NASA-CR-199358

Oscillating Flow and Heat Transfer in a Channel with Sudden Cross Section Change

Final Report

Dr. Ibrahim

Period Covered: 1/2/89 to 6/30/93

Cleveland State University
1983 East 24th Street
Cleveland, Ohio 44115

Grant Number: NAG 3-971

Computers Fluids Vol. 23, No. 1, pp. 211–224, 1994
Printed in Great Britain.

0045-7930/94 $6.00 + 0.00

OSCILLATING FLOW IN CHANNELS WITH A SUDDEN CHANGE IN CROSS SECTION

MOUNIR IBRAHIM and WAQAR HASHIM†
Mechanical Enginering Department, Cleveland State University, Euclid Avenue at East 24th Street, Cleveland, OH 44115, U.S.A.

(Received 20 February 1992; in revised form 13 July 1992)

Abstract—In this paper, we have computationally examined oscillating flow (zero mean) between two parallel plates with a sudden change in cross section. The flow was assumed to be laminar incompressible with the inflow velocity uniform over the channel cross section but varying sinusoidally with time. The cases studied cover wide ranges of Re_{max} (from 187.5 to 2000), Va (from 1 to 10.66), the expansion ratio (1:2 and 1:4) and A_r (2 and 4). Also, three different geometric cases were discussed: (a) asymmetric expansion/contraction; (b) symmetric expansion/contraction; and (c) symmetric blunt body. For these oscillating flow conditions, the fluid undergoes sudden expansion in one-half of the cycle and sudden contraction in the other half. The instantaneous friction factor, for some ranges of Re_{max} and Va, deviated substantially from the steady-state friction factor for the same flow parameters. A region has been identified (see Fig. 3) below which the flow is laminar quasi-steady. A videotape showing computer simulations of the oscillating flow demonstrates the usefulness of the current analyses in providing information on the transient hydraulic phenomena.

NOMENCLATURE

A_r—Relative amplitude of the fluid displacement [see equation (11)]
D_h—Hydraulic diameter of the smaller channel
f—Instantaneous friction factor ($=2\tau_w/\rho U_m^2$)
h—Height of the smaller channel
H—Height of the larger channel
l—Total channel length
P—Pressure
Re—Instantaneous Reynolds number
S—Step size (see Fig. 1)
St—Strouhal number [see equation (12)]
t—Time
T—Time period for one cycle
U—X-component of velocity
V—Y-component of velocity
Va—Valensi number [see equation (10)]
X—Distance along the channel axis
Y—Distance normal to the channel axis

Greek symbols
ρ—Density of the fluid
μ—Dynamic viscosity of the fluid
ω—Frequency of oscillation

Subscripts
Dh—Based on the hydraulic diameter
i—Based on the inlet condition
m—Mean value
max—Maximum during the cycle
min—Minimum during the cycle
0—Initial condition/reference state
ss—Steady state
w—At the wall

INTRODUCTION

Several engineering applications encounter unsteady flow as well as sudden changes in the channel cross section. In free-piston Stirling engine applications, the flow oscillates around a zero mean while sudden changes in the cross section take place at the components interface. As an example, in the NASA SPRE (Space Power Research Engine) the flow goes through a sudden change in cross section at the interface between the heater and the expansion space as well as between the cooler and the compression space. Today, a steady-state correlation for the fluid flow and heat transfer are used in the design analyses of such engines.

Typically, under these oscillating flow conditions the fluid undergoes a sudden expansion in one-half of the cycle and a sudden contraction in the other half. The flow reversal is caused not only by the flow oscillation but also by the sudden expansion.

Since the flow in Stirling engines oscillates in a cyclic manner, the velocity and temperature profiles differ significantly from those obtained for steady flows [1–3]. Accordingly, the friction

†Presently at: General Motors, Flint, MI, U.S.A.

factor and heat transfer coefficient are considerably different from those of the steady-state correlations.

Several computational, experimental and analytical efforts have been conducted to examine the oscillating flows within a straight channel (circular pipe and parallel plates); Ibrahim *et al.* [1] and Kurzweg [2] have performed several numerical investigations. Simon and Seume [3, 4] conducted an experimental analysis for oscillating flow in a circular pipe. Their results show a significant increase in the friction factor as compared to steady flow conditions.

A literature survey shows that several investigations have been conducted for flows with a sudden change in the area of the cross-section. Examples involve steady unidirectional flow over a backward-facing step [5–8] and flow through a sudden contraction in a channel [9–11]. The results obtained showed an enhancement in the friction factor as compared to a straight geometry under similar flow conditions.

In this paper, results from a computational analysis of the flow between two parallel plates with a sudden change in cross section are presented. The flow parameters are selected to emulate the NASA SPRE. Several geometries and expansion ratios have been examined to identify the flow characteristics under different engine operating conditions.

Since experimental data for such a problem do not exist, a careful step-by-step procedure has been used for validating the computer code. This includes, examination of false diffusion, comparison with available data for steady flows as well as solving for impulsively started flows.

ANALYSIS

Assumptions

Figure 1 shows the channel with two parallel plates and a sudden change in cross section and the Cartesian coordinate system used for the present analyses. Different geometries are considered: (a) asymmetric expansion/contraction [Fig. 1(a)]; (b) symmetric expansion/contraction [Fig. 1(b)]; and (c) a symmetric blunt body [Fig. 1(c)]. The following assumptions were made: (1) the flow is laminar incompressible with constant thermophysical properties; (2) the inlet velocity is uniform but varies sinusoidally with time; and (3) the location of the step is far away from both ends; this is chosen to isolate the effect of the step on the flow field from the end effects.

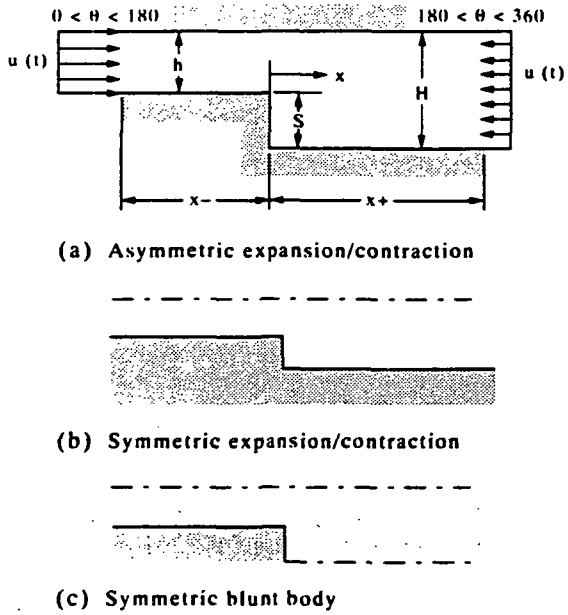

Fig. 1. The different geometries examined: (a) asymmetric expansion/contraction; (b) symmetric expansion/contraction; (c) symmetric blunt body.

Governing Equations

For unsteady laminar flow the following system of equations is employed.

Continuity equation

$$\frac{\partial(\rho u)}{\partial x}+\frac{\partial(\rho v)}{\partial y}=0. \tag{1}$$

Momentum equations

Two equations for momentum result from conservation of momentum in the x- and y-directions, respectively:

x-momentum,

$$\frac{\partial(\rho u)}{\partial t}+\frac{\partial(\rho u^2+\tau_{xx})}{\partial x}+\frac{\partial(\rho uv+\tau_{xy})}{\partial y}=-\frac{\partial p}{\partial x}; \tag{2}$$

and

y-momentum,

$$\frac{\partial(\rho v)}{\partial t}+\frac{\partial(\rho uv+\tau_{yx})}{\partial x}+\frac{\partial(\rho v^2+\tau_{yy})}{\partial y}=-\frac{\partial p}{\partial y}. \tag{3}$$

The momentum equations are cast into a standardized form by utilizing the relationship between the viscous stress and the strain rates:

$$-\tau_{xy}=-\tau_{yx}=\mu\left(\frac{\partial u}{\partial y}+\frac{\partial v}{\partial x}\right). \tag{4}$$

Equations of the following form result, which are parabolic in time but elliptic in space coordinates:

$$\frac{\partial(\rho u)}{\partial t}+\frac{\partial\left(\rho u^2-\mu\dfrac{\partial u}{\partial x}\right)}{\partial x}+\frac{\partial\left(\rho uv-\mu\dfrac{\partial u}{\partial y}\right)}{\partial y}=-\frac{\partial p}{\partial x}+S_u \tag{5}$$

and

$$\frac{\partial(\rho u)}{\partial t}+\frac{\partial\left(\rho uv-\mu\dfrac{\partial v}{\partial x}\right)}{\partial x}+\frac{\partial\left(\rho v^2-\mu\dfrac{\partial v}{\partial y}\right)}{\partial y}=-\frac{\partial p}{\partial y}+S_v, \tag{6}$$

where

$$S_u=\frac{\partial\left(\mu\dfrac{\partial u}{\partial x}\right)}{\partial x}+\frac{\partial\left(\mu\dfrac{\partial v}{\partial y}\right)}{\partial y} \tag{7}$$

and

$$S_v=\frac{\partial\left(\mu\dfrac{\partial u}{\partial y}\right)}{\partial x}+\frac{\partial\left(\mu\dfrac{\partial v}{\partial x}\right)}{\partial y}. \tag{8}$$

For incompressible/constant property flows, the source terms are zero from the continuity equation.

Dimensionless Parameters

Different dimensionless parameters characterize the unsteady flow in the channel under consideration:

(1) Re_{max}; for oscillating flows the mean flow velocity for a cycle is zero, therefore the Reynolds number is based on the maximum amplitude of the velocity during each cycle:

$$\mathrm{Re}_{max}=\frac{U_{max}\cdot D_h}{\dfrac{\mu}{\rho}}. \tag{9}$$

(2) Va; the frequency of oscillation has been expressed in dimensionless form as the Valensi number:

$$\mathrm{Va} = \frac{\omega \cdot (\mathrm{d})^2}{4.0 \cdot \frac{\mu}{\rho}}. \tag{10}$$

(3) A_r; the relative amplitude of fluid displacement is defined as the maximum fluid displacement during half a cycle divided by the channel length, based on the assumption that the fluid moves as a slug flow through the passage:

$$A_r = \frac{X_{\max}}{L}. \tag{11}$$

Three different physical situations can be identified:

(a) $A_r < 1$; part of the fluid oscillates within the passage without exiting.
(b) $A_r = 1$; the volume of fluid displaced in half a cycle is exactly equal to the volume of fluid contained within the passage.
(c) $A_r > 1$; the volume of fluid displaced during half a cycle is greater than the volume of fluid contained within the passage.

(4) St; the Strouhal number is a combination of $\mathrm{Re}_{\max}$ and Va:

$$\mathrm{St} = 4.0 \cdot \left(\frac{\mathrm{Va}}{\mathrm{Re}_{\max}} \right). \tag{12}$$

It should be noted that for the same channel geometry, a constant A_r would also imply a constant St.

(5) Another important physical parameter is the channel expansion ratio h/H (sometimes referred to in terms of the step height).

Boundary Conditions

The following boundary conditions are applied:

(1) Solid walls,

$$U = V = 0. \tag{13}$$

(2) Axis of symmetry,

$$\frac{\partial u}{\partial y} = 0, \quad v = 0. \tag{14}$$

(3) Inlet plane

$$U_i = U_{\max} \sin(\omega t). \tag{15}$$

(4) Outlet plane; the exit plane is chosen to be sufficiently far away from the zones of recirculation, therefore the gradients normal to the exit plane (i.e. along the streamwise direction) can be neglected:

$$\frac{\partial u}{\partial x} = \frac{\partial v}{\partial x} = 0. \tag{16}$$

It should be noted that for oscillating flows the inlet and outlet planes are switched at the appropriate time step so that a flow reversal is implemented numerically.

Numerical Method

The analysis performed utilizes a modified version of the computer code CAST, developed by Peric and Scheuerer [12]. The original code is capable of solving two-dimensional, steady and

Table 1. The different cases studied in the present work

Test case	Expansion ratio	Re_{max}	Va	No. of axes of symmetry	A_r	$\frac{T_w}{T_{in}}$	Mesh
A	1:2	187.5	1.0	N/A	2.0	1.2	84 × 22
B	1:2	187.5	1.0	1	4.0	1.2	84 × 22
C	1:2	187.5	1.0	2	4.0	1.2	84 × 22
D	1:4	187.5	1.0	N/A	2.0	1.2	84 × 22
E	1:2	1000.0	5.33	N/A	2.0	1.2	84 × 22
F	1:2	1000.0	5.33	1	4.0	1.2	84 × 22
G	1:2	1000.0	5.33	2	4.0	1.2	84 × 22
H	1:2	1000.0	5.33	1	2.0	1.2	94 × 22
I	1:2	1000.0	5.33	2	2.0	1.2	94 × 22
J	1:4	1000.0	5.33	N/A	2.0	1.2	84 × 32
K	1:2	2000.0	10.66	N/A	2.0	1.2	84 × 22
L	1:4	2000.0	10.66	N/A	2.0	1.2	84 × 32

unsteady, unidirectional flow problems. It has been modified to handle time-dependent boundary conditions for oscillating flows. CAST solves two-dimensional Navier–Stokes equations for laminar flows utilizing a collocated grid. A special velocity–pressure coupling [12] is used, based on the staggered grid concept to prevent oscillatory pressure solution [13]. The numerical solution procedure is a conservative finite volume method using primitive variables such as velocities, pressure and enthalpy. The basic principal involved in this method is to balance the dependent variable fluxes at the inlet and outlet of each control volume within the analysis domain. The solution procedure employed is the well-known SIMPLE algorithm by Patankar [13].

For all cases investigated, the flow cycle was divided into 60 time steps of 6-degree intervals. At least 3 cycles were run for each case to achieve a converged solution. A 0.2% convergence criteria was used in this study. The CPU time required on a Cray X-MP/Y-MP ranged from 3600 to 8000 s (for 3 cycles), depending upon the size of the mesh used (see Table 1).

CODE VALIDATION

Several computational experiments were conducted to validate the CAST code as listed below:

1. The code predictions for the reattachment length and the minimum and maximum velocities at various locations along the channel axis, for Re = 50 and 150 and expansion ratios of 1:1.2 and 1:1.5, were compared with similar steady flow results by Morgan *et al.* [8]; the comparisons were good.
2. Comparisons were made between the present code predictions and the numerical computations by Chiu [6] for steady flow over a backward-facing step, asymmetric channel with a 1:1.5 expansion ratio and Re = 916. The present code prediction for the friction factor is within 5% of Chiu's results.
3. Comparison was made, for the size of the separation bubble before the step in a forward-facing step flow at Re = 200, between the present code prediction and the numerical computation by Mei and Plotkin [11]. The agreement was within 2%.
4. Also, the present code was used to compute an impulsively started flow over a backward-facing step with Re = 400 and a 1:2 expansion ratio. The solution was marched in time and the friction factor and reattachment length were compared with the steady flow results for the same case. The agreement was within 1%. Similar agreement was found upon examining a forward-facing step case.
5. Finally, unsteady flow calculations were conducted for oscillating flow (zero mean) in a straight channel and were in excellent agreement with available analytical solutions for fully developed channel flow [2].

RESULTS AND DISCUSSION

Table 1 lists the cases studied in this paper. These cases cover wide ranges of Re_{max} (from 187.5 to 2000), Va (from 1 to 10.66), the expansion ratio (1:2 and 1:4) and A_r (2 and 4). Also, shown in the table are the three geometric cases discussed above:

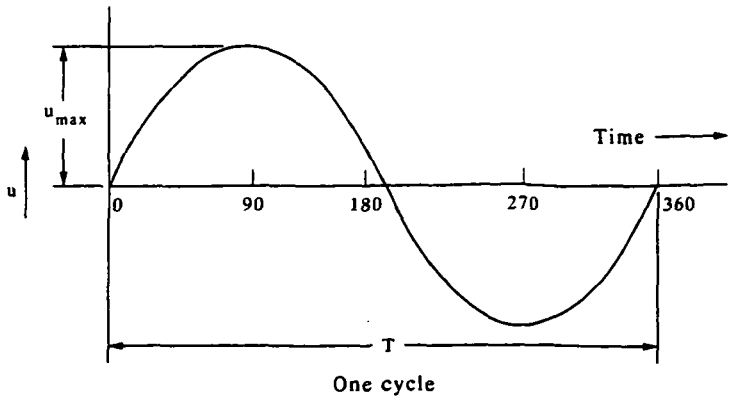

Fig. 2. Time-varying sinusoidal velocity at the channel inlet.

(a) Asymmetric expansion/contraction, cases A, D, E, J, K and L.
(b) Symmetric expansion/contraction, cases B, F and H.
(c) Symmetric blunt body, cases C, G and I.

All cases correspond to operating conditions of the NASA SPRE heater at St = 0.021333. The inlet velocity at either end of the channel varies sinusoidally with time, as shown in Fig. 2.

Figure 3 shows the envelope in which different Stirling engines operate, plotted in terms of Re_{max} vs Va [4]. In the figure, different criteria [14, 15] for the transition from laminar to turbulent flow are shown, for a straight channel. Below these lines (low Re_{max}) the flow will remain laminar throughout the cycle, while above them some combination of laminar/transitional/turbulent flow occurs over the cycle. As evident from the plot, most of the Stirling engine conditions are in the transition or "fully turbulent" zone. Efforts are underway to map the conditions under which quasi-steady turbulence models can be applied to oscillating flow conditions. For more details, see Ref. [16].

The solid circles shown in Fig. 3 are for cases A, E and K (see Table 1) as well as other runs made (not shown in this paper). We have attempted to identify the region in which the flow is

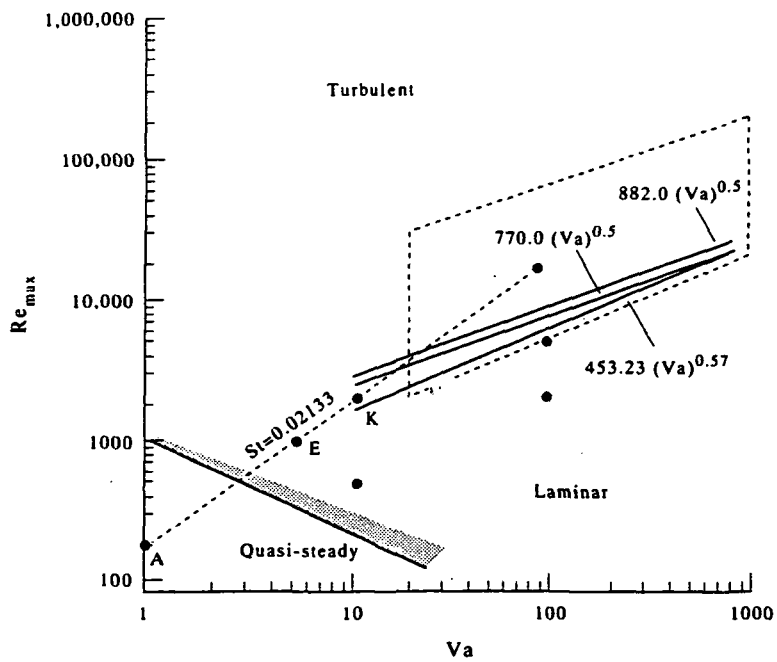

Fig. 3. Envelope in which different Stirling engines operate, together with: (i) the criterion for transition from laminar to turbulent flow in straight channels, $Re_{max} = 822 \times (Va^{0.5})$, $Re_{max} = 770 \times (Va^{0.5})$ and $Re_{max} = 453.23 \times (Va^{0.57})$; (ii) the different cases studied in the present work.

laminar quasi-steady. Case A lies in that region, while cases E and K are in the non-quasi-steady region (to be discussed in more detail later). The shaded area in the figure indicates our estimation (outcome of the present analysis) that below it the flow is laminar quasi-steady, while above it the flow becomes laminar non-quasi-steady.

Effect of the Geometry

Figure 4 shows the streamlines of the oscillating flow at different velocity phase angles of 30, 60, 90, 120, 150, 180, 210, 240, 270, 300, 330 and 360. The results are for $Re_{max} = 187.5$, $Va = 1$ and an asymmetric expansion/contraction with a ratio of 1:2 (case A). Figure 5 shows similar results for a symmetric expansion/contraction (case B); while Fig. 6 is for a symmetric blunt body (case C). From the plots it can be seen that in the sudden expansion process, the separation bubble behind the step grows gradually during flow acceleration and then shrinks gradually during flow

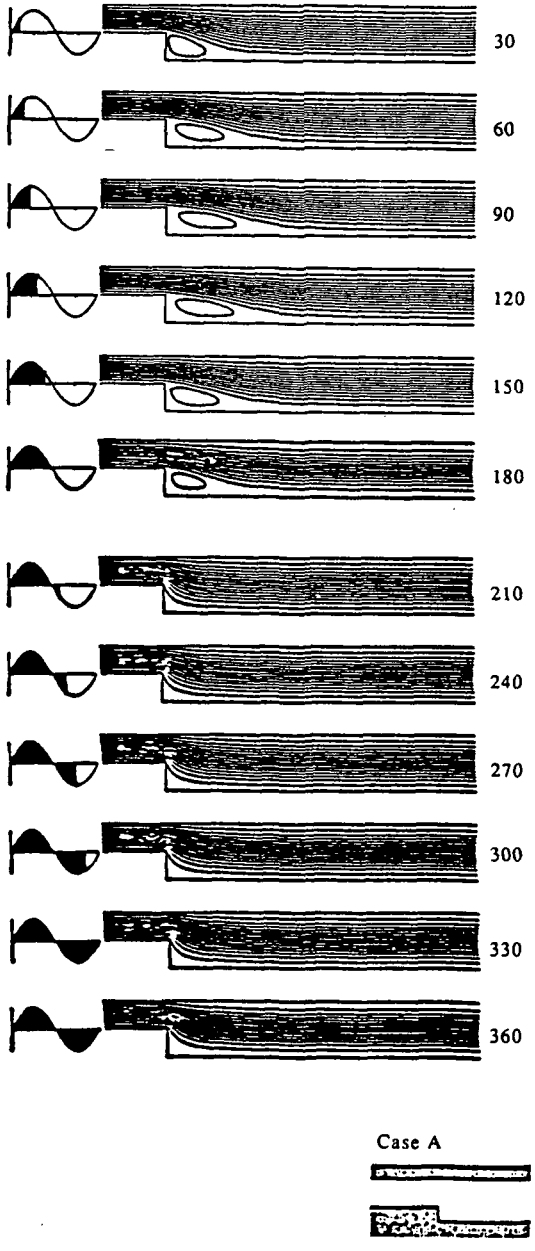

Fig. 4. Streamlines of oscillating flow at different velocity phase angles, for $Re_{max} = 187.5$ and $Va = 1$. (Case A, asymmetric expansion/contraction with a ratio of 1:2.)

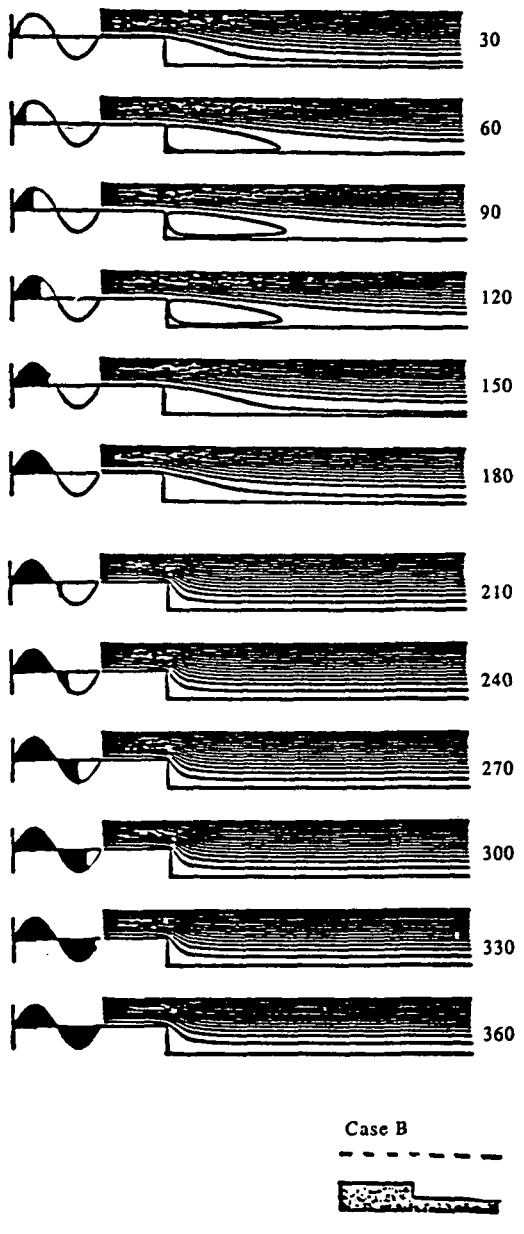

Fig. 5. Streamlines of oscillating flow at different velocity phase angles, for $Re_{max} = 187.5$ and $Va = 1$. (Case B, symmetric expansion/contraction with a ratio of 1:2.)

deceleration. However, this bubble disappears completely during the flow reversal (sudden contraction). Also, as expected, the size of the separation bubble (at a given velocity phase angle) gets progressively bigger from A to B to C. These cases, as described above, show a quasi-steady behavior.

As for the friction factor results (not shown in this paper for all cases); it was found that for case B the friction factor is of the same order of magnitude as the asymmetric expansion (case A). The difference lies in the developing zone beyond the reattachment point. Similar trends are observed for $Re_{max} = 1000$—cases E, F and G.

Effect of Re_{max} and Va

Figure 7 shows the streamlines of the oscillating flow at different velocity phase angles of 30, 60, 90, 120, 150, 180, 210, 240, 270, 300, 330 and 360. The results are for $Re_{max} = 500$, $Va = 10.66$ and an asymmetric expansion/contraction with a ratio of 1:2. Similar results are shown in Fig. 8 for $Re_{max} = 1000$, $Va = 10.66$ and an asymmetric expansion/contraction with a ratio of 1:2 (case

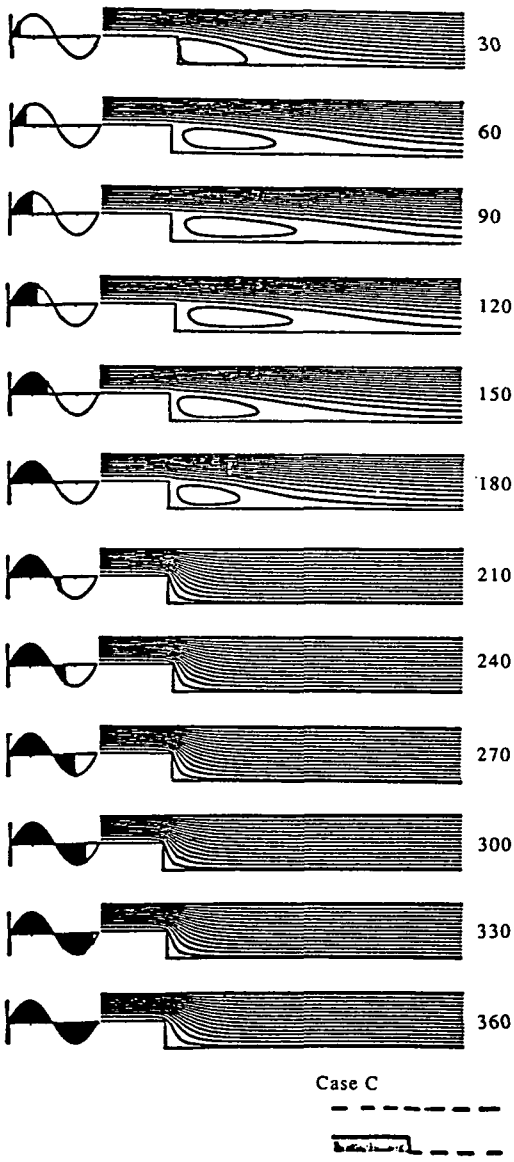

Fig. 6. Streamlines of oscillating flow at different velocity phase angles, for $Re_{max} = 187.5$ and $Va = 1$. (Case C, symmetric blunt body with a ratio of 1:2.)

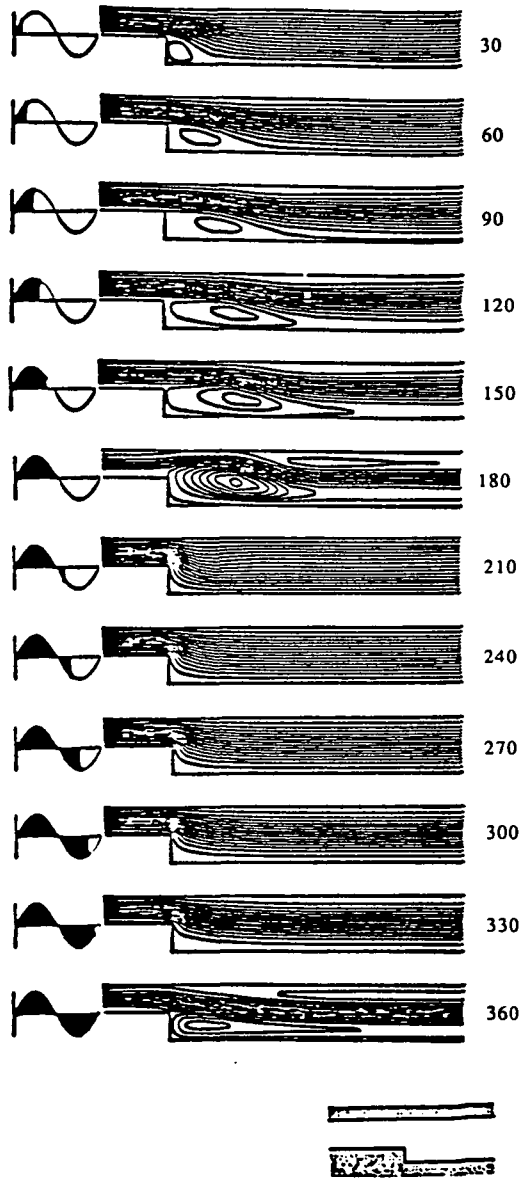

Fig. 7. Streamlines of oscillating flow at different velocity phase angles, for $Re_{max} = 500$ and $Va = 10.66$ (Asymmetric expansion/contraction with a ratio of 1:2.)

E). Experimental and analytical results for a straight channel[4], also see Fig. 3, indicate that the flow can be assumed laminar for the two cases. Due to the lack of experimental evidence for the channel with a sudden change in cross section, the flow is considered laminar. It was observed while watching the animation videos of the above cases that as the fluid accelerates during the sudden expansion phase, the separation bubble region grows in magnitude and physical size. This effect is observed irrespective of the magnitude of the flow Re. However, during the flow deceleration, this separation bubble loses momentum rapidly and disappears for cases A–D (low Re) but continues to grow while losing momentum for cases E–L (relatively higher Re). This observation, can be seen also by comparing Figs 4, 7 and 8.

For the cases presented, Va is also increased with the Re to maintain a constant St corresponding to the actual Stirling engine.

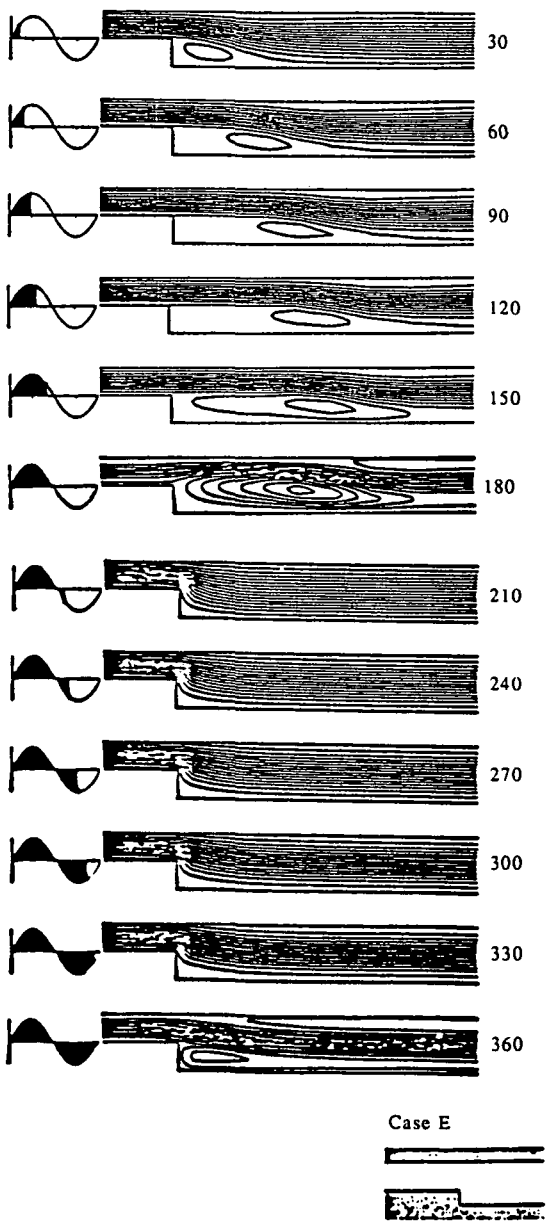

Fig. 8. Streamlines of oscillating flow at different velocity phase angles, for $Re_{max} = 1000$ and $Va = 5.33$ (Case E, asymmetric expansion/contraction with a ratio of 1:2.)

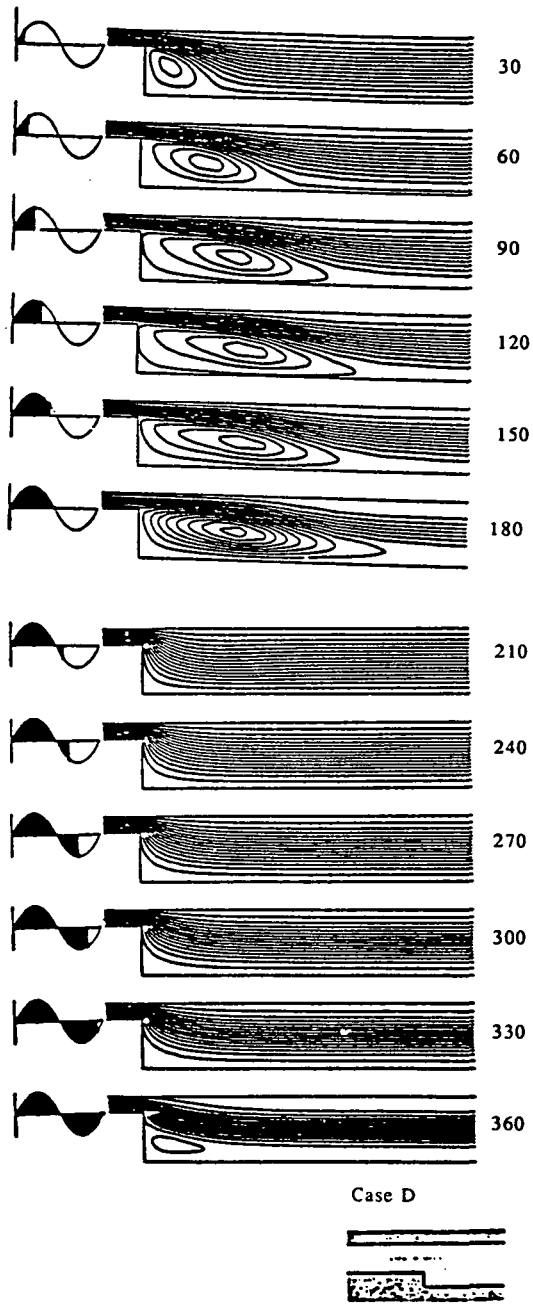

Fig. 9. Streamlines of oscillating flow at different velocity phase angles, for $Re_{max} = 187.5$ and $Va = 1$. (Case D, asymmetric expansion/contraction with a ratio of 1:4.)

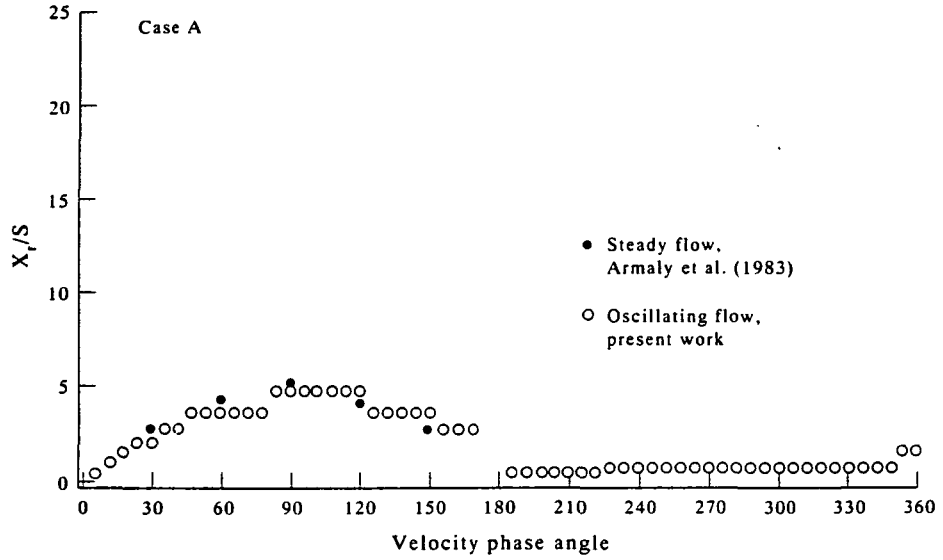

Fig. 10. Reattachment length vs time for oscillating flow at $Re_{max} = 187.5$ and $Va = 1$. (Case A, asymmetric expansion/contraction with a ratio of 1:2.)

It was found from the analysis in this work that as Va increases, the flow becomes non-quasi-steady at a lower Re_{max}. This is shown in Fig. 3 by the shaded area, below which the flow can be considered quasi-steady. Also, this could lead to the conclusion that as Va increases the flow is likely to become turbulent at a much lower Re_{max} than normally observed for straight channels.

Effect of the Expansion Ratio

Figure 9 shows the streamlines of the oscillating flow at different velocity phase angles of 30, 60, 90, 120, 150, 180, 210, 240, 270, 300, 330 and 360. The results are for $Re_{max} = 187.5$, $Va = 1$ and an asymmetric expansion/contraction with a ratio of 1:4 (case D).

Comparing cases A and D (both are similar except for the expansion ratio), the recirculation zone in case D grows to almost 4 times the size in case A. The recirculation zone, being larger, dissipates its energy during the fluid deceleration and experiences some growth. This affects the

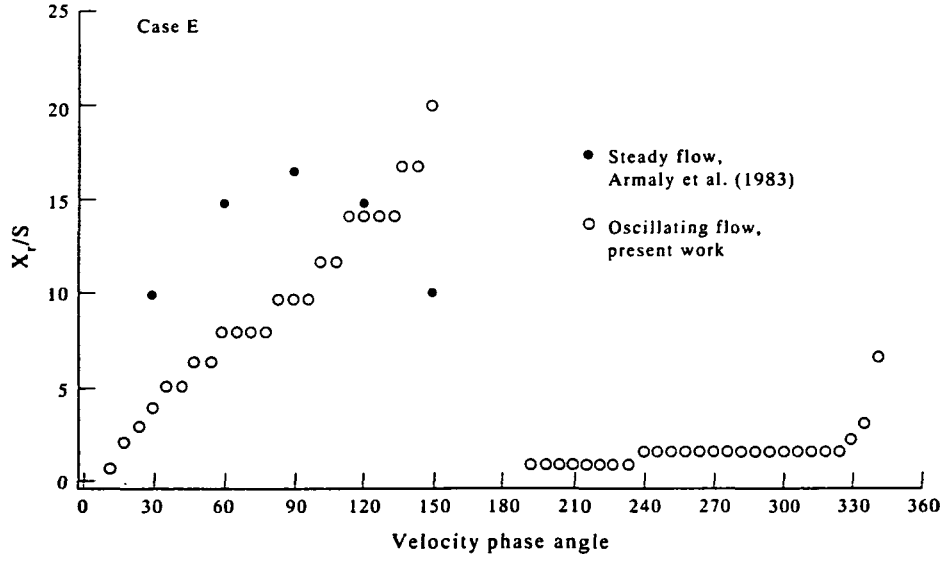

Fig. 11. Reattachment length vs time for oscillating flow at $Re_{max} = 1000$ and $Va = 5.33$. (Case E, asymmetric expansion/contraction with a ratio of 1:2.)

friction factor by more than an order of magnitude (not shown in this paper). Also, because of a larger recirculation zone, which results in good mixing, wall heat flux is reduced (not shown in this paper). Again, by comparing cases A and D, it can be seen that although case A is quasi-steady, case D is not because of the higher expansion ratio.

For a higher Re, cases E and J ($Re_{max} = 1000$) and cases K and L ($Re_{max} = 2000$), a similar trend regarding the size of the recirculation zone and the corresponding effect on friction and heat transfer is observed.

Reattachment Length

Figure 10 shows the reattachment length vs velocity phase angle for $Re_{max} = 187.5$, $Va = 1$ and an asymmetric expansion/contraction with a ratio of 1:2 (case A). Also, shown is the reattachment length, given by Armaly *et al.* [5], for steady flow at the instantaneous Re. The results of the present analysis show good agreement, indicating that the flow is quasi-steady as explained earlier. On the other hand, Fig. 11 shows a similar plot of the reattachment length vs velocity phase angle at a higher $Re_{max} = 1000$, $Va = 5.33$ (case E). It can be seen from Fig. 11 that the reattachment length will grow initially at a lower rate than in the corresponding quasi-steady case, thereafter it will

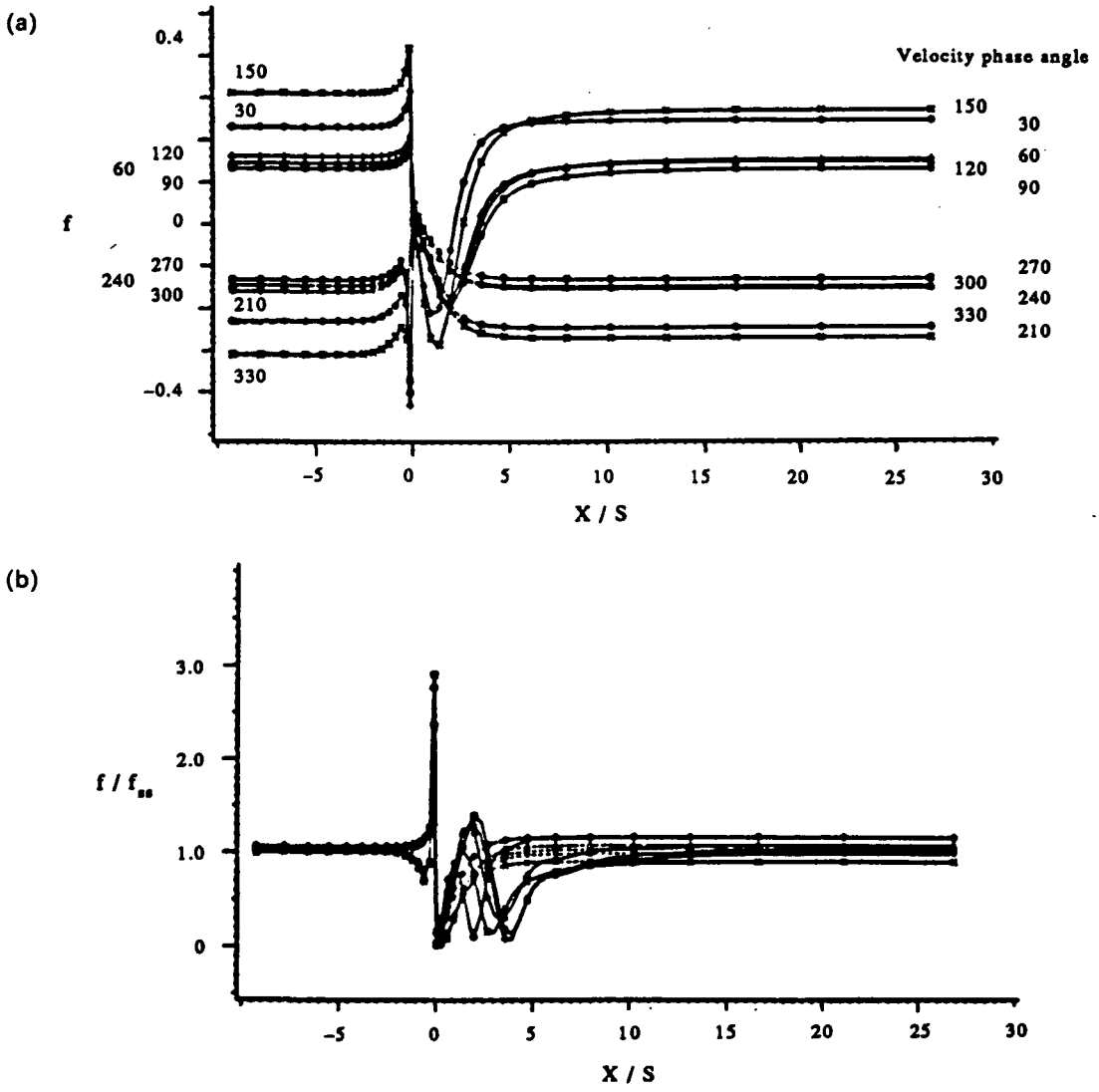

Fig. 12. (a) Friction factor vs time for oscillating flow at $Re_{max} = 187.5$ and $Va = 1$. (Case A, asymmetric expansion/contraction with a ratio of 1:2.). (b) Normalized friction factor vs time for oscillating flow at $Re_{max} = 187.5$ and $Va = 1$. (Case A, asymmetric expansion/contraction with a ratio of 1:2.)

continue to grow at a higher rate and then disappear during flow reversal, i.e. case E is non-quasi-steady.

Friction Factor

Figure 12(a) shows the instantaneous friction factor vs dimensionless axial distance at different velocity phase angles, for $Re_{max} = 187.5$, $Va = 1$ and an asymmetric expansion/contraction with a ratio of 1:2 (case A). A similar plot is shown in Fig. 12(b) but with the coordinate being the instantaneous friction factor divided by the steady-state friction factor at the instantaneous Re. The quasi-steady behavior is observed by having values of f/f_{ss} close to 1.0 in Fig. 12(b) at all times and most of the channel axial locations.

Figure 13(a) shows the instantaneous friction factor vs dimensionless axial distance at different velocity phase angles, for $Re_{max} = 1000$, $Va = 5.33$ and an asymmetric expansion/contraction with a ratio of 1:2 (case E). A similar plot is shown in Fig. 13(b) but with the coordinate being the instantaneous friction factor divided by the steady-state friction factor at the instantaneous Re. It can be seen from Fig. 13(b) that f/f_{ss} departs considerably from 1.0, particularly after the step, indicating a non-quasi-steady behavior. The friction factor can be a factor of 2 higher or lower than the steady flow values for X/S east from the reattachment location. This indicates

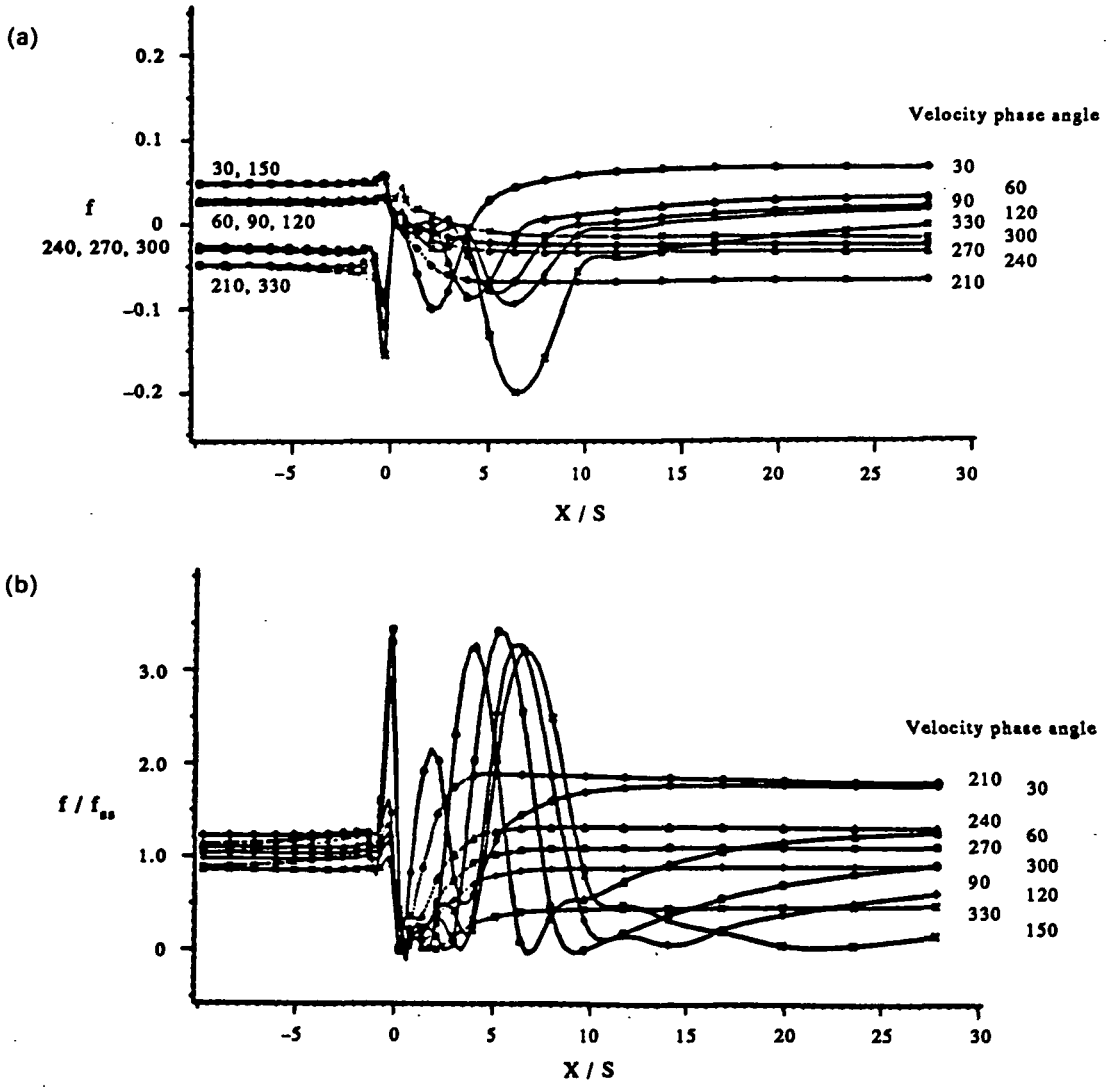

Fig. 13. (a) Friction factor vs time for oscillating flow at $Re_{max} = 1000$ and $Va = 5.33$. (Case E, asymmetric expansion/contraction with a ratio of 1:2.). (b) Normalized friction factor vs time for oscillating flow at $Re_{max} = 1000$ and $Va = 5.33$. (Case E, asymmetric expansion/contraction with a ratio of 1:2.)

that the steady-state friction factor correlations cannot be used in such applications. Work is underway to develop new correlations for the friction factor and pressure drops for oscillating flow conditions.

CONCLUDING REMARKS

In this paper the oscillating flow (zero mean) between two parallel plates with a sudden change in cross section was studied. The flow was assumed to be laminar incompressible with the inflow velocity uniform over the channel cross section but varying sinusoidally with time. Under these conditions, the fluid undergoes a sudden expansion in one-half of the cycle and a sudden contraction in the other half. The flow reversal, under such conditions, is caused not only by the flow oscillations but also by the sudden change in cross section.

A computer code, CAST, developed by Peric and Scheuerer [12] has been modified to handle time-varying boundary conditions. The CAST code solves Navier–Stokes equations in 2-D using a finite volume method. The code has been validated by comparing its predictions with available computational, experimental and analytical data for straight channels and those with a sudden change in cross section. Good agreements were found for the friction factor, reattachment length and minimum and maximum velocities at different axial channel locations.

The computations were extended to oscillating flow conditions. The cases examined emulate the operating parameters of the NASA SPRE (Space Power Research Engine). The Re_{max} in cases presented here is chosen to be sufficiently low that the assumption of laminar flow holds true during the entire flow cycle. The cases examined are summarized in Table 1.

In all cases examined, a separation zone appears during the sudden expansion and grows as the flow accelerates. This growth, however, depends on the Re_{max}. For low Re_{max} ($=187.5$), the growth follows a quasi-steady behavior, while for the higher Re_{max} ($=1000$) the growth is very rapid and the separation bubble continues growing during flow deceleration (non-quasi-steady behavior).

A shaded area has been identified (see Fig. 3), below which the flow is laminar quasi-steady. This indicated that as Va increases the flow becomes non-quasi-steady at a lower Re_{max}.

When the flow reverses, the fluid goes through a sudden contraction and the recirculation bubble from the previous half-cycle is swept back into the smaller section of the channel.

Such flow behavior causes the instantaneous friction factor to deviate substantially from the steady-state friction factor for the same flow parameters. The friction factor can be a factor of 2 higher or lower than the steady flow values for X/S east from the reattachment location. Work is underway to develop new correlations for the friction factor and pressure drops under oscillating flow conditions.

Upon examining the effect of the channel expansion ratio, it was found that for the same Re and Va, increasing the expansion ratio increases the friction losses. This is consistent with the observations made by several researchers studying steady flows with a change in the channel cross section.

Acknowledgements—This research has been conducted under NASA grant No. NAG3-971. Mr Roy C. Tew Jr, of NASA Lewis Research Center, is greatly acknowledged for his encouragement and helpful suggestions.

REFERENCES

1. M. B. Ibrahim, R. C. Tew and J. E. Dudenhoefer, Two-dimensional numerical simulation of a Stirling engine heat exchanger. NASA Technical Memorandum 102057 (1989).
2. U. H. Kurzweg, Enhanced heat conduction in oscillating viscous flows within parallel-plate channels. *J. Fluid Mech.* **156**, 291 (1985).
3. T. W. Simon and J. R. A. Seume, Survey of oscillating flow in Stirling engine heat exchangers. NASA Contractor Report 182108 (Mar. 1988).
4. J. R. Seume, An experimental investigation of transition in oscillating pipe flow. Ph.D. Thesis, Univ. of Minnesota, Minneapolis, MN (1988).
5. B. F. Armaly, F. Durst, J. C. F. Pereira and B. Schonung, Experimental and theroetical investigation of backward-facing step flow. *J. Fluid Mech.* **127**, 473 (1983).
6. I. T. Chiu, *Prediction of laminar flows over rearward-facing step using the partially-parabolized Navier–Stokes equations.* Master's Thesis, Iowa State Univ., Ames, IA (1984).
7. O. K. Kwon, R. H. Pletcher and J. P. Lewis, Prediction of sudden expansion flows using the boundary-layer equations. *J. Fluids Engng* **106**, 285 (1984).
8. K. Morgan, J. Periaux and F. Thomasset, Analysis of laminar flow over a backward-facing step. In *Proceedings of a GAMM Workshop*. Vieweg, Braunschweig (1984).

9. A. Baron, F. K. Tsou and W. Aung, Flow field and heat transfer associated with laminar flow over a forward-facing step. In *Heat Transfer 1986: Proc. 8th Int. Conf.*, San Francisco, CA, Vol. 3, pp. 1077–1082 (1986).
10. S. Hafez and M. A. Serag-Eldin, Computation of the recirculating flow over and under bluff-bodies. In *Proc. 4th Int. Conf. on Numerical Methods in Laminar and Turbulent Flows*, Vol. 1, Chap. 1, pp. 687–695 (1985).
11. R. W. Mei and A. Plotkin, Navier–Stokes solutions for laminar incompressible flows in forward-facing step geometries. *AIAA Jl* **24**, (1986).
12. M. Peric and G. Scheuerer, CAST—a finite volume method for predicting two-dimensional flow and heat transfer phenomena. GRS-Technische Notiz SSR-89-01 (Sept. 1989).
13. S. V. Patankar, *Numerical Heat Transfer and Fluid Flow*. Hemisphere, Washington, DC (1980).
14. M. Ohmi and M. Iguchi, Critical Reynolds number in an oscillating pipe flow. *Bull. JSME* **25**, 165 (1982).
15. M. Hino, M. Sawamoto and S. Takasu, Experiments on the transition to turbulence in an oscillatory pipe flow. *J. Fluid Mech.* **131**, 363 (1983).
16. K.-H. Ahn and M. B. Ibrahim, A 2-D oscillating flow analysis in Stirling engine heat exchangers. NASA Technical Memorandum 103781 (1991).

COMPRESSIBILITY EFFECTS ON THE PERIODIC UNSTEADY FLOWS

CHO-FAI KWAN

Bachelor of Science in Mechanical Engineering

Cleveland State University

June, 1988

submitted in partial fulfillment of requirements for the degree

MASTER OF SCIENCE IN MECHANICAL ENGINEERING

at the

CLEVELAND STATE UNIVERSITY

June, 1992

This thesis has been approved for the

Department of Mechanical Engineering and the

College of Graduate Studies by

_____

Thesis Committee Chairperson

_____

(Department/Date)

_____

_____

(Department/Date)

_____

_____

(Department/Date)

TABLE OF CONTENTS

LIST OF TABLES

LIST OF FIGURES

NOMENCLATURE

A	Constant in hybrid finite-difference scheme
$A_j^u, A_j^v, A_j^\phi, A_j^\theta$	Coefficients in finite-difference expressions
A_R	Amplitude ratio $(= 1/2 * D_h/L * Re_{max}/\omega^*)$
B	Constant in hybrid finite-difference scheme
$B_j^u, B_j^v, B_j^\phi, B_j^\theta$	Coefficients in finite-difference expressions
C	Speed of sound [m/s]; constant in hybrid finite-difference scheme
$C_j^u, C_j^v, C_j^\phi, C_j^\theta$	Coefficients in finite-difference expressions
C_p	Specific heat of fluid at constant pressure [J/kg*K]
D_h	Hydraulic diameter $(= 2H)$ [m]
$D_j^u, D_j^v, D_j^\phi, D_j^\theta$	Coefficients in finite-difference expressions
f_{app}	Local friction factor based on apparent wall shear stress
F1, F2	Normalized pressure gradient in x and y directions, respectively
G	Mass flux $(= \rho u)$ [kg/(s*m^2)]
G1, G2	Pressure gradient in x and y directions, respectively [Pa/m]
H	Height of the channel [m]
k	Thermal conductivity of fluid [W/m*K]
k^*	Normalized thermal conductivity of fluid
L	Length of channel [m]
M	Mach number
Nu_b	Nusselt number based on the bulk-mean temperature $(= q_w D_h/k(T_w - \tau_b))$

Nu_0	Nusselt number based on the inlet temperature (= $q_w D_h/k(T_w-T_0)$)
p	Static pressure [Pa]
P	Normalized static pressure
Pr	Prandtl number of fluid (= $C_p\mu/k$)
q	Heat flux per unit surface area [W/m^2]
R	Gas constant
Re	Reynolds number based on the Channel's Height (= $u\rho D_h/\mu$)
R_c	Critical mesh Reynolds number
R_m^+, R_m^-	Mesh Reynolds numbers
S	Sutherland's constant [K]
S_p	Dimensionless source term in pressure Poisson equation
S_ϕ	Dimensionless source term for velocity correction potential
t	Time [sec]
T	Static temperature [K]
u	Streamwise fluid velocity [m/s]
U	Normalized streamwise velocity
U^*	Normalized streamwise mass flux
v	Transverse fluid velocity [m/s]
V	Normalized transverse velocity
V^*	Normalized transverse mass flux
W	Constant for Hybrid differencing scheme
x	Cartesian coordinate in streamwise direction [m]
X	Normalized streamwise x distance

X^+	Dimensionless coordinate in the streamwise direction (= $4x/D_hRePr$)
$\Delta X_u^-, \Delta X_u, \Delta X_u^+, \Delta X_u^{++}$	Streamwise grid spacing
$\Delta X^-, \Delta X, \Delta X^+, \Delta X^{++}$	Streamwise grid spacing
y	Cartesian coordinate in transverse direction [m]
Y	Normalized transverse y distance
$\Delta Y^-, \Delta Y^+, \Delta Y_v^-, \Delta Y_v^+$	Transverse grid spacing

Greek Symbols

α	Constant for viscosity power law
β	Constant for conductivity power law
B	Constant in the Sutherland's equation [$kg/m*s*K^{0.5}$]
Γ	Normalized stagnation temperature
γ	Specific heat ratio
θ	Normalized static temperature
μ	Dynamic viscosity [kg/m*s]
μ^*	Normalized dynamic viscosity
ν	Kinematic viscosity [m^2/s]
ρ	Fluid density [kg/m^3]
ρ^*	Normalized fluid density
τ	Stagnation temperature [K]
Φ	Normalized time
ϕ	Velocity correction potential
$\psi/2$	Amplitude of the imposed velocity fluctuation
ω	Fluctuating frequency [Hz]
ω^*	Valensi number (= $\omega\rho H^2/\mu$)

Subscripts

b	Bulk-mean value
c	Correction value
e	Exact value
exit	Channel exit value
i	x-grid counter
j	y-grid counter
mean	Mean value
max	Maximum value
ref	Reference value
o	Inlet value
s	Steady state value
w	Wall value
x	Value at the x location; values for x-momentum equation
y	Values for y-momentum equation
l	Transient value minus steady-state value

Superscripts

n	"Global" iteration counter
t	Time step counter

CHAPTER I

INTRODUCTION

Inside the heat exchangers of an operating Stirling engine are hundreds of tubes where heat is transferred with the working fluid under oscillating flow conditions. Presently, NASA is using one-dimensional performance codes to model and simulate this unsteady, oscillating flow towards the development of the free-piston Stirling engines. These performance codes utilize incompressible steady-flow heat transfer and friction factor correlations, while excluding the effects of oscillation and the compressibility of the working gas. Thus, the validity of using the steady-state correlations for the oscillating conditions is questionable [Tew,1987; Ibrahim et.al.,1990]. Confidence is also lacking in the predicted performance by these one-dimensional analyses.

The present study investigates the complex oscillating flow conditions within the Stirling engine. The objectives of the current research are as follows:

1) to develop a two-dimensional modeling code for compressible, unsteady, periodic internal flows;

2) to better understand the fluid flow and heat transfer phenomena under the pulsating/oscillating conditions and to compare the results with the steady flow conditions;

3) to investigate the compressibility effect on the friction and the heat transfer; and

4) to visualize the results on video with computer animation.

The current computer code evolved from the codes developed earlier by Chilukuri [1979], Madavan [1981] and Chiu [1984], whom have used it to estimate incompressible steady flow. However, the current effort is to modify the computer code to accept unsteady compressible flows.

Two types of unsteady flows will be examined in this thesis, and to avoid possible confusion, the following definitions will clarify the differences between the oscillating and pulsating flows:

1) Oscillating - the flow fluctuates back and forth in the channel and the time-averaged velocity of this flow type is equal to zero.

2) Pulsating - the flow is fluctuating around a steady driven flow and the time-averaged velocity of this flow type is non-zero. An example of the pulsating flow is the circulation of blood in one's veins.

Review of Past Research

Steady Flow (Incompressible):

Numerous studies exist in the literature on the problem of steady incompressible flow through parallel plates with various boundary conditions, and most of the pioneer works were based on the boundary layer theory. Some of the researchers were Schlichting [1960], Siegel and Sparrow [1959], and Bhatti and Savery [1977].

In his "Boundary Layer Theory" book, Schlichting [1960] analytically resolved the boundary layer equations for flow between parallel plates, and his analysis was based on the Blasius solution technique for external flat plate flow. For heat transfer analysis, Siegel and Sparrow [1959] obtained a closed form approximated Nusselt number equation for simultaneously developing flow under the condition of uniform wall temperatures, while Bhatti and Savery [1977] solved the same problem except the heating they used was provided by the constant wall heat flux.

Narang and Krishnamoorthy [1976] presented the pressure and velocity solutions at the entrance flow regions of the parallel plates for the low Reynolds number. They solved the Navier-Stokes equations by linearizing the inertia terms and observed overshoots in the developing velocity profiles which was not obtained by the boundary layer equation. Their results were compared with data from Schlichting [1960] and they concluded the boundary layer assumptions for the entrance region were only valid for the higher Reynolds number (Re > 200). They also observed

the v-velocity at the entrance was as large as 30% of the inlet u-velocity for the low Reynolds number (Re ≈ 2), where the v-velocity is assumed zero in the boundary layer theory.

Some other researchers who solved the full Navier-Stokes equations were Brandt and Gilles [1966], Morihara and Cheng [1973], and Chen [1973]. Brandt and Gilles [1966] utilized the finite-difference approximation in their study of incompressible flow in a straight channel with the presence of a transverse magnetic field. Morihara and Cheng [1973] solved the Navier-Stokes equation by first eliminating the pressure terms followed by quasilinearizing the nonlinear terms in the resultant momentum equation. Finite-difference formulas combined with the Gaussian elimination solver was utilized to reach the solution. The Reynolds number that was considered, ranged from zero to 4000.

In the entrance flow study by Chen [1973], he performed the momentum integral method to solve the Navier-Stokes equation and obtained approximated closed form solutions for the center-line velocity development and the average axial pressure drop. His results were compared and were in excellent agreement with the finite-element solution and the experimental study at the low Reynolds numbers for flows in circular tubes by Atkinson, et.al. [1969]. A comparison was also conducted with the finite-difference analysis by Friedmamn, et.al. [1968]. Velocity overshoot in the developing profiles were observed by all the investigators who applied the full Navier-Stokes equations.

While the majority of the experimental data for steady internal flows

were performed with the circular tube, a few studies on the parallel plates were found. Heaton, et.al. [1964] performed an experimental study of simultaneously developing flow with constant uniform wall heat flux in Annulus which simulated the parallel plates channel. In a more recent study, Lou and Barton [1973] assembled a recirculation loop experimental apparatus with a rectangular channel test section that measured 7 inches wide by 1/4 inch deep and was 2 to 6 inches long. The fluids examined were water (Pr=5.7), 20% ethylene-glycol (Pr=10) and 72% ethylene-glycol (Pr=50). Their heat transfer results for constant wall temperature compared well with the theoretical data from Lou [1971].

Finally, an experimental investigation of the developing thermal entrance region with heating at the lower plate and cooling at the upper plate was done by Kamotani and Ostrach [1976].

Variable Property Flows:

Two types of variable property flows have been considered in the literature: thermally expandable (temperature dependent) and compressible (temperature and pressure dependent). An initial thermally expandable flow investigation was studied by Van Driest [1952]. Van Driest modeled the steady laminar, external air flow over a flat plate using the boundary layer method. He assumed the Prandtl number and the specific heat as constants while employing the Sutherland law to describe the fluid viscosity. Van Driest presented predictions for skin-friction and for the heat transfer coefficient as functions of the Reynolds number, the Mach

number and the wall to free-stream temperature ratio.

For the thermally expandable internal flows, Bankston and McEligot [1969] utilized the superposition method on their study of the coolant channels of a nuclear reactor. The objective was to determine the wall temperature from an imposed constant wall heat flux by the variable property model and the incompressible model. They found that the variation of the fluid properties tends to shorten the thermal entry region when heating the fluid.

Later, Bankston and McEligot [1970] extended their study by using the numerical method of finite control volume to solve the two-dimensional, coupled boundary layer equations. The study was done on the circular tube with constant heat flux; laminar and turbulent flows were considered. They showed that the variable property slightly affected the Nusselt number but the friction parameters were tripled when compared with incompressible results under heating conditions. The same analyses were performed for the parallel plates channel with constant wall temperature in Schade and McEligot [1971] paper. The study was performed in the wall/inlet temperature ratios that ranged from high heating (T_w/T_0=10) to extreme cooling (T_w/T_0=0.1). Similar conclusions as the circular tube study were found; the effects of gas property variation on the laminar flow of air are slight to moderate for heat transfer and more severe for the friction.

Herwig et.al. [1990] introduced an efficient approximation method to resolve the variable viscosity pipe flow caused by temperature changes.

The basic idea is to expand the viscosity in a Taylor series so that the Navier-Stokes and energy equations can be decoupled. By doing so, no additional nonlinearities are imposed by the temperature-dependent viscosity, hence, the set of equations that has to be solved is much simpler than the full set of coupled equations.

In the case of compressible flows, most literature found dealt with the study of external aerodynamic design of planes or high speed flows over a flat plate. MacCormack [1976] examined the time-dependent, two-dimensional compressible Navier-Stokes equations at Mach number of two. He presented a method to solve for the interaction of a shock wave with the boundary layer on a flat plate. The method time-splits the governing equations into a hyperbolic part and a parabolic part. The hyperbolic part was solved by the explicit method while the parabolic part was solved by the implicit scheme.

Other methods to resolve the high-speed compressible flow over a flat plate were introduced. Beam and Warming [1978] and Kwon et.al. [1988] applied the implicit finite-difference algorithm with a second-order-time accurate scheme which required data storage of two time levels. MacCormack [1982] introduced a new efficient unconditionally stable method that consisted of two stages to solution. The first stage used an explicit predictor-corrector finite-difference method while the second stage transformed the governing equations into an implicit form. Han [1983] then modified the SIMPLE (Semi-Implicit-Method for Pressure-Linked-Equation) Algorithm to predict transient analysis of both high speed (compressible)

and low speed (incompressible) fluid flows.

Besides flows over a flat plate, Kim [1990] studied the transonic flow over an axisymmetric curved hill. Hassankhan [1983] examined the effects of fluid compressibility on the stagnation point of a circular cylinder in cross flow. Hassankhan found that the friction increases when the Mach number and/or the wall/inlet temperature ratio increases.

As for internal compressible flow, no literature was found for the parallel plates geometry but two studies were located for circular tubes. Presler [1971] studied helium gas flow in a circular tube with uniform entrance conditions and wall heat flux conditions. The study was done both analytically and experimentally with an electrically heated small-diameter Inconel tube. The numerical results were performed for low values of the initial Mach number to prevent the choking effects. Presler reported that for any level of uniform wall heat flux, the local Nusselt number showed only small deviations from the constant property analyses, while the friction was larger for higher wall heat fluxes. The comparison of his analytical and experimental results were all within 10 percent. Similar results were found by Cebeci and Bradshaw [1984].

CHAPTER II

ANALYSIS

Figure 2.1 reveals the cross sectional view of the NASA Stirling Power Research Engine (SPRE). The components of interest are the two heat exchangers (heater and cooler) that supply and eject the necessary thermal energy to continue the oscillating motion of the working helium gas. A closer look at the inside of these heat exchangers reveals hundreds of straight, narrow tubes that contain the oscillating helium gas. Instead of examining the global heat exchanger problems, the present study is to explore and understand the detail flow and heat transfer phenomena of the fluid within each tube. The parallel plate channel is chosen for modeling this detailed single tube problem.

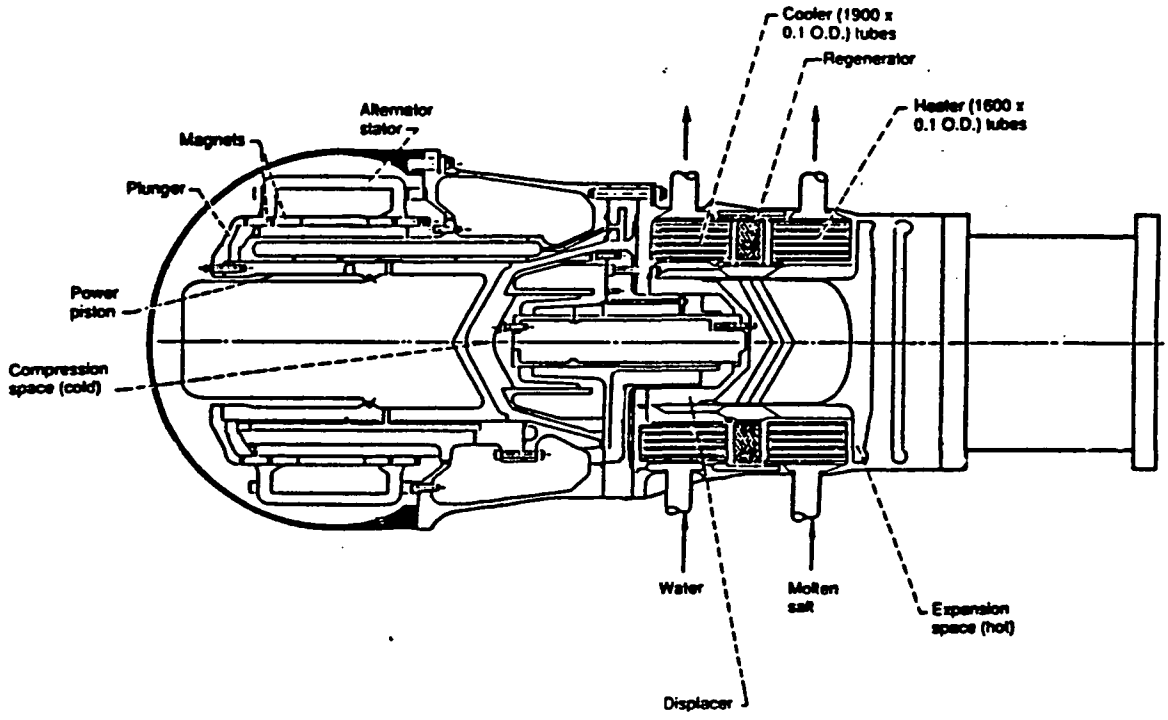

Figure 2.1: The cross section of the Stirling Power Research Engine, SPRE.

Geometry and Coordinate System

Figure 2.2 shows the parallel plate channel geometry and the Cartesian coordinate system used. The origin of the coordinate system resides at the west corner of the lower plate with the x-axis set along the stream-wise direction while the y-axis starts from zero at the lower plate to the value of H/2 at the channel's center-line. For the steady and pulsating flows, the fluid enters the channel from the west where the numerical calculation begins (Fig. 2.3). As for the oscillating flow, the fluid enters from the west during the forward half of the cycle and then shifts to enter from the east during the reverse half of the cycle (Fig. 2.4).

Assumptions

In the heater and cooler tubes, the unsteady periodic fluid flow contains the complexities of 3-dimensional, laminar, transient and turbulent flows; the fluid enters the heater and cooler tubes from the expansion and compression space, respectively, through the passage of a sudden change in the cross-sectional area; the oscillating phase angle difference between the displacer and the power piston causes real gas compression and expansion within the tubes. Due to the enormous amount of experimental

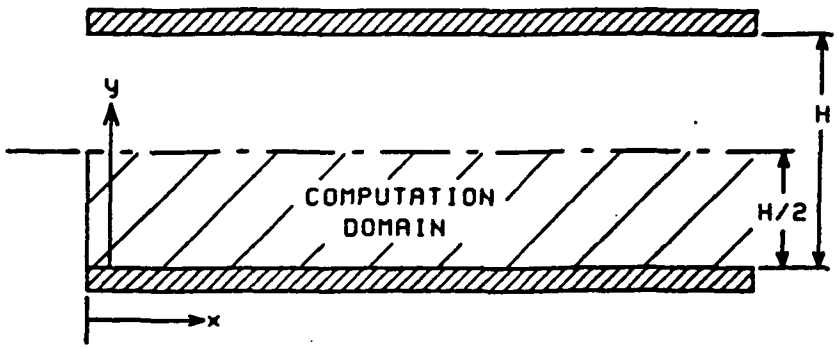

Figure 2.2: The parallel plate channel with the Cartesian coordinate system.

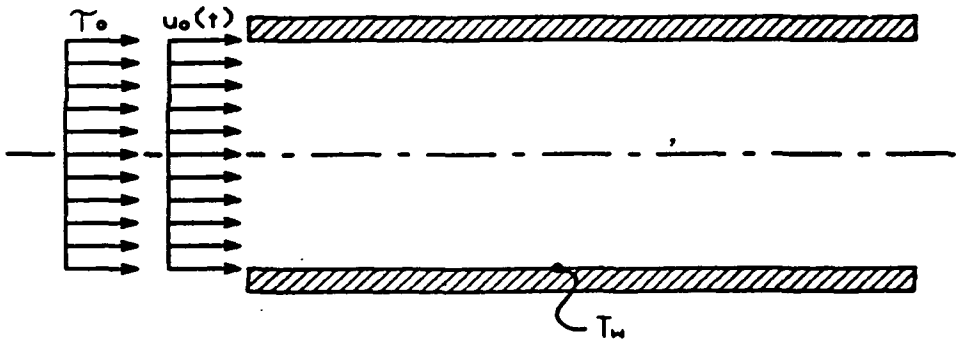

Figure 2.3: The boundary conditions for steady and pulsating flows.

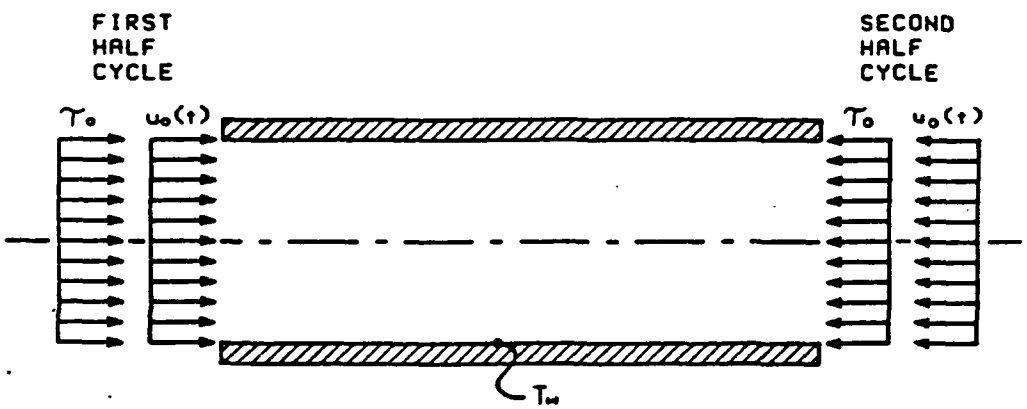

Figure 2.4: The boundary conditions for oscillating flows.

data and time it would take to model these complex conditions, the present study is simplified and is limited to the following assumptions:

a) The fluid flow is a two-dimensional, laminar with variable properties except the C_p and Pr are assumed constant;

b) The inlet velocity profile is uniform and

   i. constant with time for steady flow;

   ii. varies sinusoidally with time for unsteady flows;

c) The fluid enters the channel with uniform temperature and heat is transferred from (or to) the constant temperature plate walls;

d) The axial viscous diffusion and heat conduction are negligible;

e) The flow is subsonic.

Static Temperature versus Stagnation Temperature

To prevent confusion when examining compressible flow, the difference between static and stagnation temperatures will be clarified. The stagnation enthalpy of the fluid represents the combination of thermal energy and kinetic energy. Since the specific heat of the fluid is assumed to be constant, the stagnation enthalpy equation can be written in terms of the stagnation temperature (sometimes called total temperature):

$$\tau = T + \frac{u^2 + v^2}{2 C_p} \qquad \text{where: } \tau \text{ is the stagnation temperature}, \; T \text{ is the static temperature} \qquad (2.1)$$

As suggested by the equation, the stagnation temperature represents the total temperature as the gas is brought to rest by an adiabatic process. If the fluid velocity is slow or the Mach number is close to zero, the fluid kinetic energy is negligibly small compared to the fluid thermal energy; hence, the stagnation temperature and static temperature are equal.

$$M = 0 \quad \rightarrow \quad \tau = T$$

For the incompressible and thermally expandable flows, the presumption of the zero Mach number results in identical static and stagnation temperature values, therefore, no distinction between these temperatures is necessary as in most incompressible and thermally expandable flow literature. However, the compressible flow presumes a non-zero value of the Mach number which means the kinetic energy of the fluid can no longer be ignored and the two temperatures are differentiated by equation 2.1.

Governing Equations

The complete Navier-Stokes (NS) equations can model any viscous flow problems. Mathematically, NS equations are elliptic partial-differential equations which in a physical view-point, the flow at any location is affected by the rest of the flow field. Computing these coupled elliptic differential equations by finite-difference methods requires iterative solvers, but these solvers require heavy computer time and memory space.

For flows with a predominant flow direction, as in the current study, where the axial viscous diffusion and heat conduction are small and negligible, the NS equations can be simplified into the Partially-Parabolized Navier-Stokes (PPNS) equations. The PPNS equations are parabolic partial-differential equations by nature except the elliptic behavior associated with the pressure remains. Having the streamwise diffusion neglected, the flow at any location is affected only by the upstream flow and can be solved by marching methods which are relatively more efficient in computer time and memory space than iterative methods. Please note that only the pressure in the PPNS equations is computed by using iterative solvers.

Utilizing the assumptions stated earlier, the governing PPNS equations in primitive variables are as follows:

Continuity Equation:

$$\frac{\partial \rho}{\partial t} + \frac{\partial (\rho u)}{\partial x} + \frac{\partial (\rho v)}{\partial y} = 0 \qquad (2.2)$$

X-Momentum Equation:

$$\rho \left(\frac{\partial u}{\partial t} + u \frac{\partial u}{\partial x} + v \frac{\partial u}{\partial y} \right) = - \frac{\partial p}{\partial x} + \frac{\partial}{\partial y} \left(\mu \frac{\partial u}{\partial y} \right) \qquad (2.3)$$

Y-Momentum Equation:

$$\rho \left(\frac{\partial v}{\partial t} + u \frac{\partial v}{\partial x} + v \frac{\partial v}{\partial y} \right) = - \frac{\partial p}{\partial y} + \frac{4}{3} \frac{\partial}{\partial y} \left(\mu \frac{\partial v}{\partial y} \right) \qquad (2.4)$$

Energy Equation:

$$\rho C_p \left(\frac{\partial T}{\partial t} + u \frac{\partial T}{\partial x} + v \frac{\partial T}{\partial y} \right) = \frac{\partial}{\partial y} \left(k \frac{\partial T}{\partial y} \right) + u \frac{\partial p}{\partial x} + \frac{\partial p}{\partial t} + \mu \left(\frac{\partial u}{\partial y} \right)^2 + \frac{4}{3} \mu \left(\frac{\partial v}{\partial y} \right)^2 \qquad (2.5)$$

Note that the viscous diffusion energy is accounted for in the last two terms of the energy equation, hence the static temperature is used as a primitive variable.

The pressure has an elliptical effect throughout the flow field and is described by the Poisson equation [Anderson et.al,1984] which can be derived from the momentum equations. By rearranging equations 2.3 & 2.4, the pressure gradients can be written in the form:

$$\frac{\partial p}{\partial x} = - \left[\rho \frac{\partial u}{\partial t} + \rho u \frac{\partial u}{\partial x} + \rho v \frac{\partial u}{\partial y} - \frac{\partial}{\partial y} \left(\mu \frac{\partial u}{\partial y} \right) \right] = G1 \qquad (2.6)$$

$$\frac{\partial p}{\partial y} = - \left[\rho \frac{\partial v}{\partial t} + \rho u \frac{\partial v}{\partial x} + \rho v \frac{\partial v}{\partial y} - \frac{4}{3} \frac{\partial}{\partial y} \left(\mu \frac{\partial v}{\partial y} \right) \right] = G2 \qquad (2.7)$$

and the Poisson equation is:

$$\nabla^2 p = \frac{\partial^2 p}{\partial x^2} + \frac{\partial^2 p}{\partial y^2} = \frac{\partial G1}{\partial x} + \frac{\partial G2}{\partial y} \qquad (2.8)$$

The above governing equations are similar to the equations Chiu [1984] utilized in his analyses, except Chiu examined the steady, incompressible flows which made the apparent form of his PPNS equations somewhat further simplified. The present equations are more general as they contain additional time dependent terms to account for the unsteady flows and the equations have variable fluid properties (density, viscosity and conductivity) within the derivatives.

Equations of State

To account for fluid compressibility, one state equation is required for describing each variable fluid property (density, viscosity and conductivity). Assuming the gas is ideal, the density can be determined from the pressure and the static temperature by using the Perfect Gas Law.

$$\rho = \frac{P}{RT} \qquad \textit{where R is the Gas constant} \qquad (2.9)$$

To date, the viscosity of gases has been described by two commonly-used equations, the Power Law and the Sutherland Law.

The Viscosity Power Law:

$$\frac{\mu}{\mu_{ref}} = \left(\frac{T}{T_{ref}}\right)^{\alpha} \qquad \textit{where } \alpha \textit{ is a constant} \qquad (2.10)$$

The Sutherland Law:

$$\mu = \frac{BT^{\frac{3}{2}}}{T+S} \qquad \textit{where B and S are Sutherland coefficients} \qquad (2.11)$$

The α, B and S are constants depending upon the gas used (their values for air and helium are listed in Table 2.1). The Power Law and the Sutherland Law relate the viscosity with the temperature of the gas. From the experimental data by Tribus et.al. [1942] for viscosity of air at various temperature, Driest [1952] found that the predictions from the Sutherland Law matched the data more closely than the predictions from the Power Law. Hence, the Sutherland relationship was chosen for this study to achieve more accurate viscosity estimations.

As for the fluid conductivity, again, two relationships were commonly used; the conductivity Power Law and the definition of the Prandtl number.

The Conductivity Power Law:

$$\frac{k}{k_{ref}} = \left(\frac{T}{T_{ref}}\right)^{\beta} \qquad \textit{where } \beta \textit{ is a constant} \qquad (2.12)$$

Table 2.1: Gas properties for the Power Laws and the Sutherland Viscosity Law.

GAS	α	β	B ($kg/(m*s*K^{\alpha+\beta})$)	S (K)	Pr
Air	.67	.805	1.466 E-6	110.3	.72
Helium	--	--	1.286 E-6	8.63	.72

The Definition of the Prandtl Number:

$$k = \frac{\mu C_p}{Pr} \qquad (2.13)$$

For most gases, the Prandtl number and specific heat are relatively constant for a wide range of temperature which makes the gas conductivity directly proportional to the gas viscosity when incorporating the Prandtl number definition. In this study, the Prandtl number definition is applied. As these state equations are normalized, it will become apparent why the Prandtl number is more advantageous over the Power law.

Boundary Conditions

As shown on Figure 2.2, the computational domain is one-half of the channel, from the bottom plate to the center-line of the channel. At the lower solid wall boundary, the no-slip wall condition applies and the wall temperature is constant.

$$y = 0 \quad \rightarrow \quad u = v = 0 \ , \ T = T_w$$

While at the line of symmetry, u-velocity and temperature gradients are assumed to be zero.

$$y = \frac{H}{2} \quad \rightarrow \quad v = 0 \ , \ \frac{\partial u}{\partial y} = 0 \ , \ \frac{\partial T}{\partial y} = 0$$

The upper and lower boundary conditions are identical for the steady, pulsating and oscillating flows.

Ensuring the incoming fluid contains the same energy level, the imposed inlet stagnation temperature remains constant for all flow types, while the inlet v-velocity is assumed to be zero.

$$\tau_o = constant \quad , \quad v_o = 0$$

The imposed inlet u-velocity, however, differs according to the flow type. For the steady flow, inlet u-velocity is constant (see figure 2.3).

$$u_o(t) = u_o = constant$$

In the case of pulsating flow, the u-velocity varies sinusoidally around a mean flow according to the relation:

$$u_o(t) = u_{mean,o} \cdot (1 + \tfrac{\varepsilon}{2} Sin\,\omega t) \qquad (2.14)$$

where: $\frac{\varepsilon}{2}$ *is the imposed velocity fluctuation amplitude*

Finally, the imposed inlet u-velocity for oscillating flow varies around a zero-velocity.

$$u_o(t) = u_{max,o} \cdot Sin\omega t \qquad (2.15)$$

Referring to figure 2.4, the inlet flow enters the channel from the west when u_0 is positive, and east when u_0 is negative.

The boundary conditions for the pressure Poisson equation will be discussed in the next chapter.

Similarity Parameters

The following characteristic parameters are used to generally describe the fluid flow and heat transfer in similar systems. For incompressible and steady flow, only the Reynolds number and Prandtl number is needed for generalizing similar systems.

Reynolds number (non-dimensional mass flux):

$$Re_{ref} = \frac{u_{ref} \cdot D_h}{\nu_{ref}} \qquad (2.16)$$

Prandtl number (ratio of viscosity over conductivity of the fluid):

$$Pr = \frac{C_p \cdot \mu_{ref}}{k_{ref}} \qquad (2.17)$$

The additional Mach number is required when dealing with compressible flow.

Mach number (non-dimensional flow speed):

$$M_{ref} = \frac{u_{ref}}{C_{ref}} \qquad \textit{where: } C \textit{ is the speed of sound} \tag{2.18}$$

For unsteady flow, the Valensi number generalizes the fluctuating frequency of the system.

Valensi number (non-dimensional frequency):

$$\omega^* = \frac{\omega \cdot D_h^2}{4\,\nu_{ref}} \tag{2.19}$$

An amplitude ratio is needed to describe the geometric similarity between oscillating flow systems.

Amplitude ratio (non-dimensional fluid displacement):

$$A_R = \frac{1}{2}\,\frac{D_h}{L}\,\frac{Re_{max,o}}{\omega^*} \tag{2.20}$$

where: $A_R < 1$ ➡ *fluid oscillates without exiting the channel*

$A_R > 1$ ➡ *fluid traverses quickly via the channel*

Nondimensionalization

The advantage for nondimensionalizing the variables is that the characteristic parameters such as the Reynolds number, the Prandtl number, the Mach number, etc., can be varied independently. Also the values of the normalized flow variables often fall in the range such as zero to one.

Location of the reference values depends on the flow type. The subscript "ref" used throughout the thesis has the following definitions:

a) For steady flow: ref ➡ the value at the channel's inlet.

b) For pulsating flow: ref ➡ the mean value at the channel's inlet.

c) For oscillating flow: ref ➡ the maximum value at the channel's inlet.

With the appropriate reference values, all the variables are nondimensionalized as follows:

$U = \frac{u}{u_{ref}}$: *the normalized streamwise velocity*

$V = \frac{v}{u_{ref}}$: *the normalized transverse velocity*

$P = \frac{p}{\rho_{ref} u_{ref}^2}$: *the normalized pressure*

$\theta = \frac{T}{T_{ref}}$: *the normalized static temperature*

$\Gamma = \frac{\tau}{T_{ref}}$: *the normalized stagnation temperature*

$X = \frac{\rho_{ref} u_{ref} x}{\mu_{ref}}$: *the normalized x distance*

$Y = \frac{\rho_{ref} u_{ref} y}{\mu_{ref}}$: *the normalized y distance*

$\Phi = \frac{\rho_{ref} u_{ref}^2 t}{\mu_{ref}}$: *the normalized time*

$\rho^* = \frac{\rho}{\rho_{ref}}$: *the normalized fluid density*

$\mu^* = \frac{\mu}{\mu_{ref}}$: *the normalized dynamic viscosity*

$k^* = \frac{k}{k_{ref}}$: *the normalized fluid conductivity*

$U^* = \rho^* U$: *the normalized streamwise mass flux*

$V^* = \rho^* V$: *the normalized transverse mass flux*

The Normalized Governing Equations

Thus, the partially-parabolized Navier-Stokes equations (2.2-2.5) can be converted as follows:

Continuity Equation:

$$\frac{\partial \rho^*}{\partial \Phi} + \frac{\partial U^*}{\partial X} + \frac{\partial V^*}{\partial Y} = 0 \tag{2.21}$$

X-Momentum Equation:

$$\rho^* \frac{\partial U}{\partial \Phi} + U^* \frac{\partial U}{\partial X} + V^* \frac{\partial U}{\partial Y} = -\frac{\partial P}{\partial X} + \frac{\partial}{\partial Y}\left(\mu^* \frac{\partial U}{\partial Y}\right) \tag{2.22}$$

Y-Momentum Equation:

$$\rho^* \frac{\partial V}{\partial \Phi} + U^* \frac{\partial V}{\partial X} + V^* \frac{\partial V}{\partial Y} = -\frac{\partial P}{\partial y} + \frac{4}{3}\frac{\partial}{\partial Y}\left(\mu^* \frac{\partial V}{\partial Y}\right) \tag{2.23}$$

Energy Equation:

$$\rho^* \frac{\partial \theta}{\partial \Phi} + U^* \frac{\partial \theta}{\partial X} + V^* \frac{\partial \theta}{\partial Y} = \frac{1}{Pr}\frac{\partial}{\partial Y}\left(k^* \frac{\partial \theta}{\partial Y}\right) + M_{ref}^2(\gamma - 1)\left[\frac{\partial P}{\partial \Phi} + U\frac{\partial P}{\partial X} + \mu^*\left(\frac{\partial U}{\partial Y}\right)^2 + \frac{4}{3}\mu^*\left(\frac{\partial V}{\partial Y}\right)^2\right] \tag{2.24}$$

For the Poisson equation, the x and y-momentum equations are rearranged.

$$\frac{\partial P}{\partial X} = -\left[\rho^* \frac{\partial U}{\partial \Phi} + U^* \frac{\partial U}{\partial X} + V^* \frac{\partial U}{\partial Y} - \frac{\partial}{\partial Y}\left(\mu^* \frac{\partial U}{\partial Y}\right)\right] = F1 \tag{2.25}$$

$$\frac{\partial P}{\partial Y} = -\left[\rho^* \frac{\partial V}{\partial \Phi} + U^* \frac{\partial V}{\partial X} + V^* \frac{\partial V}{\partial Y} - \frac{4}{3}\frac{\partial}{\partial Y}\left(\mu^* \frac{\partial V}{\partial Y}\right)\right] = F2 \tag{2.26}$$

The pressure Poisson Equation:

$$\nabla^2 P = \frac{\partial^2 P}{\partial X^2} + \frac{\partial^2 P}{\partial Y^2} = \frac{\partial F1}{\partial X} + \frac{\partial F2}{\partial Y} \tag{2.27}$$

Note that for thermally expandable flows, M_{ref}=0, hence the kinetic energy terms are negligible and the energy equation can be simplified to balance only the thermal energy. As for incompressible flows, ρ^*, μ^*, k^* = 1 which also converts U^* = U and V^* = V, and the coefficient value 4/3 is changed to one in the y-momentum diffusion term due to simplification by the incompressible continuity equation. With these reductions and for the steady flow condition, the normalized governing equations will be identical to the equations Chiu [1984] utilized. The present governing equations are more general than Chiu's, and they are capable to describe the different flow types considered in the present analyses.

Normalized Equations of State

Density (Ideal Gas Law):

$$\rho^* = \frac{1}{\theta} + M_{ref}^2 \frac{\Delta P \gamma}{\theta} \qquad (2.28)$$

where: ΔP = *the change of P from the channel's inlet.*

For subsonic flow where $M_{ref} << 1$, the second term on the right hand side of equation 2.28 will be insignificant compared to the first term;

hence, for low Mach number flow, the second term can be ignored and the value of the density depends solely by the temperature only. This type of flow is assumed to be thermally expandable.

Viscosity (Sutherland's Law) and Conductivity (Definition of Pr):

$$\mu^* = \theta^{\frac{3}{2}} \frac{1 + C_1}{\theta + C_1} \quad ; \quad k^* = \mu^* \qquad (2.29\ a\&b)$$

$$\text{where: } C_1 = \frac{S}{T_{ref}}$$

Viscosity and Conductivity (Power Laws):

$$\mu^* = \theta^{\alpha} \quad ; \quad k^* = \theta^{\beta} \qquad (2.30\ a\&b)$$

The definition of Prandtl number is used because it equates the normalized viscosity and the normalized conductivity, and there is one less variable to solve.

Normalized Boundary Conditions

The nondimensional boundary conditions are

a) $U = V = 0$, $\theta = \theta_w$ *no-slip boundary conditions at the wall*

b) $V = 0$, $\frac{\partial U}{\partial Y} = 0$, $\frac{\partial \theta}{\partial Y} = 0$ *symmetry boundary conditions*

c) Γ_o = *constant* , $V_o = 0$ *imposed inlet temperature and v-velocity*

d) imposed inlet u-velocity

i) $U_o(\Phi) = U_o = 1$ *for steady flow* (2.31)

ii) $U_o(\Phi) = 1 + \frac{\psi}{2} Sin\left(\frac{4\omega^* \Phi}{Re_{mean,o}}\right)$ *for pulsating flow* (2.32)

iii) $U_o(\Phi) = Sin\left(\frac{4\omega^* \Phi}{Re_{max,o}}\right)$ *for oscillating flow* (2.33)

Again, the normalized pressure boundary conditions will be discussed in Chapter III.

CHAPTER III

METHOD OF SOLUTION

Based upon the method of solution used in Chiu's thesis [1984], the present solution techniques have been revised and extended to cover a wider range of fluid flow problems including the ability to resolve unsteady periodic flows and compressible fluid flows. This chapter consists of six sections. The first section describes the staggered, finite-difference grid utilized in the computation domain. Sections 2 to 5 present the various finite-difference schemes applied on the governing equations and the numerical solvers used. Section 6 summarizes the chapter by illustrating the flow chart and the steps proceeded by the present computer program to reach the results.

The Finite-Difference Grid

Having selected the Cartesian coordinate system for the computation domain, the present finite difference analysis uses a staggered grid [Patankar,1980] to prevent the probable development of a wavelike pressure or a wavelike velocity field. The idea behind the staggered grid is to define three different grids; two for the velocity components and one for the scaler variables. As shown in Figure 3.1, the solid dots indicate the grid locations for the scaler variables (the fluid properties, pressure, temperature and the velocity correction potential ϕ), whereas the velocity components, indicated by the arrows, reside midway between these dot points. The horizontal arrows denote the locations for U and the axial pressure gradient F1, while the vertical arrows designate the positions for V and the transverse pressure gradient F2. Figure 3.1 also reveals the spatial step variables used on the unequally spaced grid.

Despite the fact that the variables are actually defined at different locations, a single reference set of grid indices is used for convenience. Referring back to Figure 3.1, the label (i+1, j) actually identifies the spatial locations of the two arrows and one solid point enclosed by the dashed boomerang, thus, $U_{i+1,\ j}$ is to the right of $P_{i+1,\ j}$ and $V_{i+1,\ j}$ is beneath $P_{i+1,\ j}$, etc.

Unlike the convectional grid which only requires a single control volume at each node, the staggered grid requires three distinctive spatial control volumes (Fig. 3.2) for the different governing equations. This

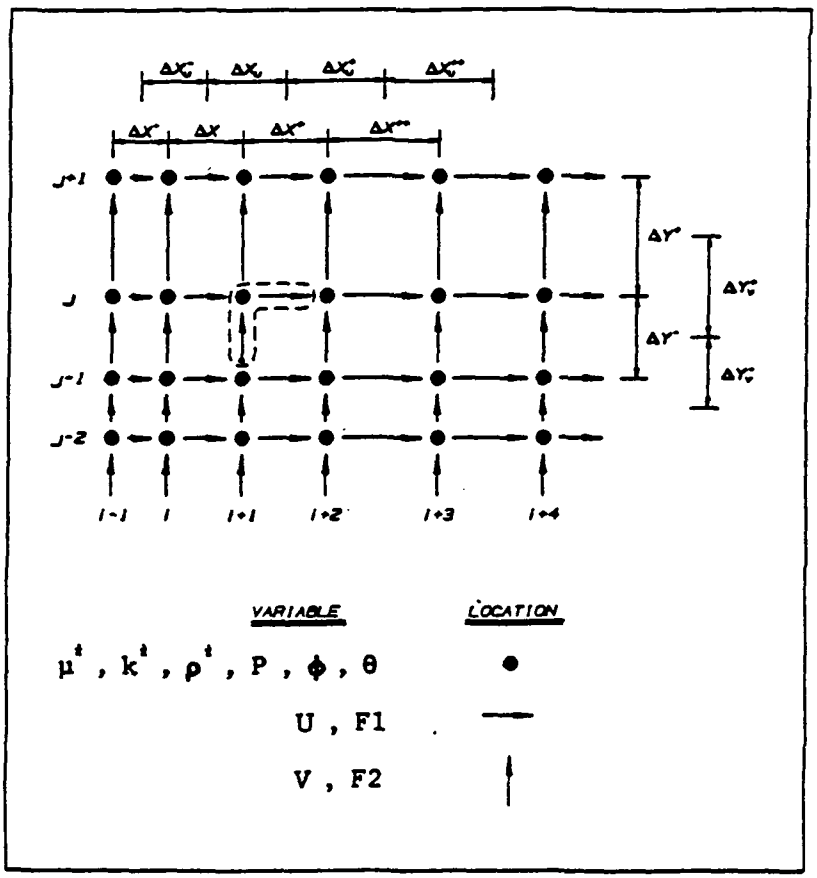

Figure 3.1: The staggered grid and the variable locations.

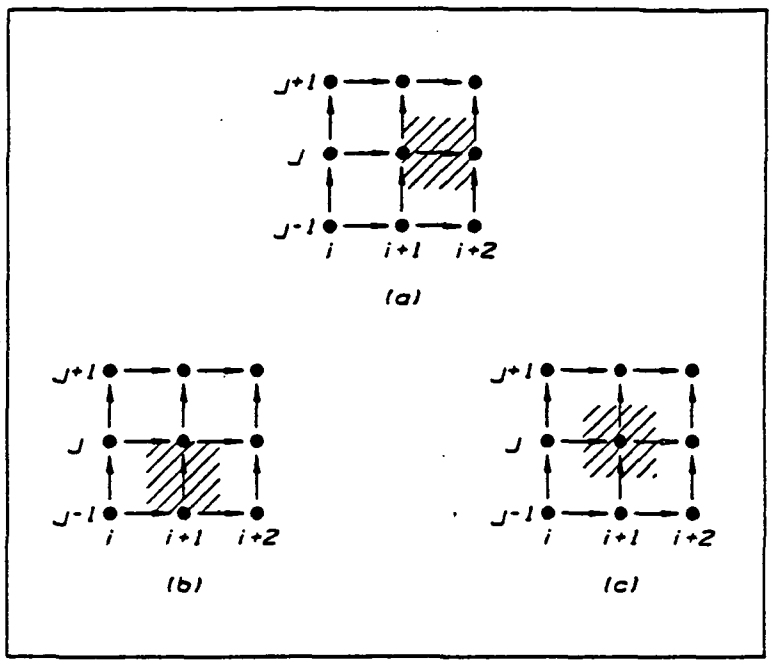

Figure 3.2: The three distinctive spatial control volumes for:
a) x-momentum equation,
b) y-momentum equation,
c) continuity, energy, and pressure Poisson equations.

concept leads to the different locations of the expansion point according to the equation; care is called upon when differencing the governing equations to the corresponding control volumes. For example, the terms in the x-momentum equation are expanded at the (i+1, j) u-velocity arrow (Fig. 3.2a), while the terms in the energy equations are expanded at the (i+1, j) pressure point (Fig. 3.2c).

Figure 3.3 shows the computational domain of the parallel plates combined with the staggered grid. Notice that a set of fictitious points is positioned below the solid wall (j = 1) and another set is located above the line of symmetry (j = NJ+1); these fictitious points are used in describing the boundaries of the domain because the horizontal boundaries in staggered grid are placed along the v-velocity arrows. Hence, the no-slip and constant temperature boundary conditions stated in Chapter Two become:

$$U_{i,2} = -U_{i,1} \tag{3.1}$$

$$V_{i,2} = 0 \tag{3.2}$$

$$\frac{\theta_{i,2}+\theta_{i,1}}{2} = \theta_w \tag{3.3}$$

At the upper boundary, the symmetric boundary conditions are prescribed as:

$$U_{i,NJ} = U_{i,NJ+1} \tag{3.4}$$

$$V_{i,NJ+1} = 0 \tag{3.5}$$

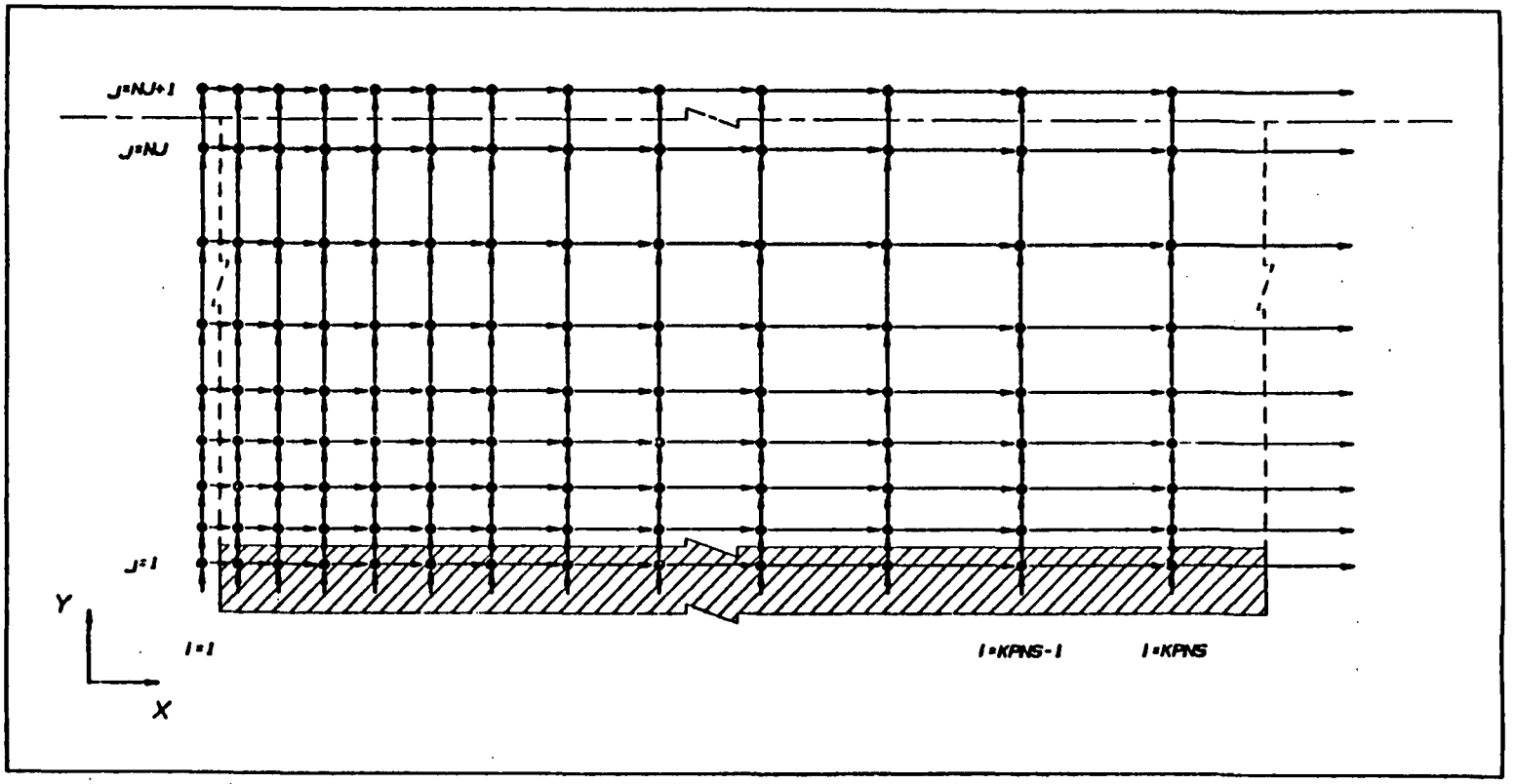

Figure 3.3: The computational domain with the staggered grid and the locations of boundaries.

$$\theta_{1,KJ} = \theta_{1,KJ+1} \qquad (3.6)$$

The velocity and temperature profiles at the inlet boundary are prescribed at the same grid indic of i=1, but the actual locations of the profiles are slightly different due to the nature of the staggered grid.

Figure 3.4 presents the two types of grid set-ups used in the present study. For the steady flow and the pulsatile flow analyses, the axial grid spacing is fine at the channel's entrance then increases down the stream while the transverse steps are fine closer to the lower wall but coarse at the channel's center (Fig. 3.4a). This set-up provides sufficient node points at the critical regions, like areas close to the entrance and the wall, where rapid gradient changes occur. As for the oscillating flow analysis, the set-up grid shown in Figure 3.4b is used and is similar to the steady flow grid, except for the fine axial steps that appear at both ends of the channel. The reasoning behind this is that during half the cycle, the flow is moving forward while the second half of the flow is moving backwards.

Finite-Difference Formulation of the Momentum Equations

Coefficients of the convective terms:

The momentum equations are algebraically nonlinear differential

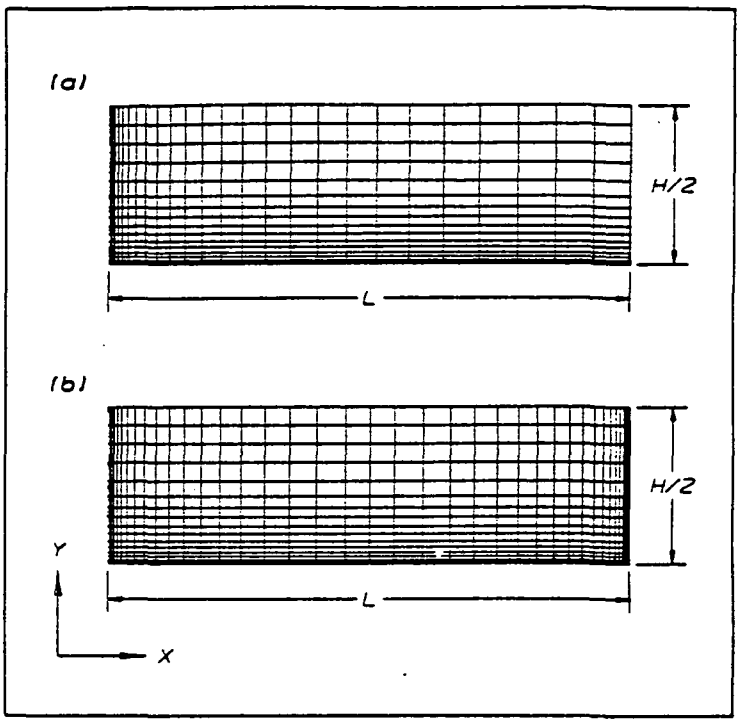

Figure 3.4: The x and y grid formats used for:
a) steady flows and pulsating flows.
b) oscillating flows.

equations. Solving these equations by numerical method requires linearizing the equations and computing them by an iterative procedure. The most common linearization strategy is done by lagging or extrapolating the coefficient U^* and V^* in the convective terms of the momentum equations. In this thesis, the coefficients in the x-momentum and y-momentum equations are denoted by the subscripts x and y, respectively.

Lagging the coefficients: The coefficients are evaluated from the previous iteration values. This method is used where values of velocity components are stored.

$$U_{x\,i+1,j}^{*\,t+1,n+1} = U^{*\,t+1,n}_{i+1,j} \tag{3.7}$$

$$U_{y\,i+1,j}^{*\,t+1,n+1} = \left[\frac{U^{*\,t+1,n}_{i,j} + U^{*\,t+1,n}_{i,j-1}}{2} \cdot \frac{\Delta X^*}{2} + \frac{U^{*\,t+1,n}_{i+1,j} + U^{*\,t+1,n}_{i+1,j-1}}{2} \cdot \frac{\Delta X}{2} \right] \cdot \frac{1}{\Delta X_u} \tag{3.8}$$

$$V_{x\,i+1,j}^{*\,t+1,n+1} = \frac{V^{*\,t+1,n}_{i+1,j} + V^{*\,t+1,n}_{i+2,j}}{2} \tag{3.9}$$

$$V_{y\,i+1,j}^{*\,t+1,n+1} = V^{*\,t+1,n}_{i+1,j} \tag{3.10}$$

Extrapolating the coefficients (regular): The coefficients are extrapolated by the upstream values. This method is always used in the first "Global" iteration at each time step, due to the lack of previously calculated values.

$$U_{x_{i+1,j}}^{*\,t+1,n+1} = U^{*\,t+1,n+1}_{i,j} + \left(U^{*\,t+1,n+1}_{i,j} - U^{*\,t+1,n+1}_{i-1,j}\right) \cdot \frac{\Delta X_u}{\Delta X_u^-} \qquad (3.11)$$

$$U_{y_{i+1,j}}^{*\,t+1,n+1} = \left[\frac{U^{*\,t+1,n+1}_{i,j} + U^{*\,t+1,n+1}_{i,j-1}}{2} \cdot \frac{\Delta X^+}{2} + \frac{U_{x_{i+1,j}}^{*\,t+1,n+1} + U_{x_{i+1,j-1}}^{*\,t+1,n+1}}{2} \cdot \frac{\Delta X}{2} \right] \cdot \frac{1}{\Delta X_u} \qquad (3.12)$$

$$V_{x_{i+1,j}}^{*\,t+1,n+1} = V^{*\,t+1,n+1}_{i,j} + \left(V^{*\,t+1,n+1}_{i,j} - V^{*\,t+1,n+1}_{i-1,j}\right) \cdot \frac{\Delta X + (\Delta X^+/2)}{\Delta X^-} \qquad (3.13)$$

$$V_{y_{i+1,j}}^{*\,t+1,n+1} = V^{*\,t+1,n+1}_{i,j} + \left(V^{*\,t+1,n+1}_{i,j} - V^{*\,t+1,n+1}_{i-1,j}\right) \cdot \frac{\Delta X}{\Delta X^-} \qquad (3.14)$$

Extrapolating the coefficients (special case): For regions where only one upstream station is available (the second x-station in the channel's inlet), the coefficients are evaluated by the previous station.

$$U_{x_{i+1,j}}^{*\,t+1,n+1} = U^{*\,t+1,n+1}_{i,j} \qquad (3.15)$$

$$U_{y_{i+1,j}}^{*\,t+1,n+1} = \frac{U^{*\,t+1,n+1}_{i,j} + U^{*\,t+1,n+1}_{i,j-1}}{2} \qquad (3.16)$$

$$V_{x_{i+1,j}}^{*\,t+1,n+1} = V^{*\,t+1,n+1}_{i,j} \qquad (3.17)$$

$$V_{y_{i+1,j}}^{*\,t+1,n+1} = V^{*\,t+1,n+1}_{i,j} \qquad (3.18)$$

Convective terms in the x-direction (axial):

$$U^* \frac{\partial U}{\partial X} \quad , \quad U^* \frac{\partial V}{\partial X}$$

Except at the entrance regions with only one station in the upwind direction, the two convective terms are differenced by the three-point,

second-order accurate, upwind scheme. The polarity of the coefficient U^* determines the direction of the upwind scheme (forward upwind for positive U^*, while backward upwind for negative U^*). Also, the second order upwind differencing used in the present work was tested for the numerical diffusion and compared with a first order upwind differencing (normally used in the literature); the present scheme showed an improvement in the predictions of about 10%.

For the x-momentum equation with forward going flow, the convective term becomes:

$$\left(U^* \frac{\partial U}{\partial X}\right)^{t+1,n+1}_{i+1,j} = U^{*\,t+1,n+1}_{x\,i+1,j} \cdot \left[\frac{U^{t+1,n+1}_{i+1,j} - U^{t+1,n+1}_{i,j}}{\Delta X_u} - \frac{U^{t+1,n+1}_{i,j} - U^{t+1,n+1}_{i-1,j}}{\Delta X_u^-} + \frac{U^{t+1,n+1}_{i+1,j} - U^{t+1,n+1}_{i-1,j}}{\Delta X_u + \Delta X_u^-} \right] \tag{3.19}$$

For the y-momentum equation with forward going flow, the convective term becomes:

$$\left(U^* \frac{\partial V}{\partial X}\right)^{t+1,n+1}_{i+1,j} = U^{*\,t+1,n+1}_{y\,i+1,j} \cdot \left[\frac{V^{t+1,n+1}_{i+1,j} - V^{t+1,n+1}_{i,j}}{\Delta X} - \frac{V^{t+1,n+1}_{i,j} - V^{t+1,n+1}_{i-1,j}}{\Delta X^-} + \frac{V^{t+1,n+1}_{i+1,j} - V^{t+1,n+1}_{i-1,j}}{\Delta X + \Delta X^-} \right] \tag{3.20}$$

However, for the inflow region where only one station is available in the upwind direction, a two-point, first-order accurate, upwind scheme is used instead of the three-point scheme.

For the x-momentum equation:

$$\left(U^* \frac{\partial U}{\partial X}\right)^{t+1,n+1}_{i+1,j} = U^{*\,t+1,n+1}_{x\,i+1,j} \cdot \frac{U^{t+1,n+1}_{i+1,j} - U^{t+1,n+1}_{i,j}}{\Delta X_u} \tag{3.21}$$

For the y-momentum equation:

$$\left(U^* \frac{\partial V}{\partial X}\right)^{t+1,n+1}_{i+1,j} = U^{*\,t+1,n+1}_{y\,i+1,j} \cdot \frac{V^{t+1,n+1}_{i+1,j} - V^{t+1,n+1}_{i,j}}{\Delta X} \tag{3.22}$$

When the coefficient U^* of the convective terms is negative, the flow is reversed and the forward moving flow differencing scheme is no longer valid. For this type of flow, a three-point upwind differencing scheme is still utilized except the differencing direction is reversed in the x-direction.

Thus, for the x-momentum equation:

$$\left(U^* \frac{\partial U}{\partial X}\right)^{t+1,n+1}_{i+1,j} = U^{*\,t+1,n+1}_{x\,i+1,j} \cdot \left[\frac{U^{t+1,n}_{i+2,j} - U^{t+1,n+1}_{i+1,j}}{\Delta X^{+}_{u}} - \frac{U^{t+1,n}_{i+3,j} - U^{t+1,n}_{i+2,j}}{\Delta X^{++}_{u}} + \frac{U^{t+1,n}_{i+3,j} - U^{t+1,n+1}_{i+1,j}}{\Delta X^{+}_{u} + \Delta X^{++}_{u}} \right] \tag{3.23}$$

For the y-momentum equation:

$$\left(U^{*}\frac{\partial V}{\partial X}\right)^{i+1,n+1}_{i+1,j} = U_{y}^{*\,i+1,n+1}_{i+1,j} \cdot \left[\frac{V^{i+1,n}_{i+2,j} - V^{i+1,n+1}_{i+1,j}}{\Delta X^{*}} - \frac{V^{i+1,n}_{i+3,j} - V^{i+1,n}_{i+2,j}}{\Delta X^{**}} + \frac{V^{i+1,n}_{i+3,j} - V^{i+1,n+1}_{i+1,j}}{\Delta X^{*} + \Delta X^{**}} \right] \qquad (3.24)$$

While the forward going differencing scheme uses velocities at the current n+1 iteration level, the reversed differencing scheme makes use of $U_{i+2,\,j}$, $U_{i+3,\,j}$, $U_{i+2,\,j}$ and $U_{i+3,\,j}$ velocities at the previous n iteration level. The reason for using previous velocity values is because they have not been updated by the marching process at the current n+1 iteration level. Thus, storage for the n level velocities is required for the flow reversal region.

Convective terms in the y-direction (transverse):

$$V^{*}\frac{\partial U}{\partial Y} \quad , \quad V^{*}\frac{\partial V}{\partial Y}$$

The hybrid differencing scheme [Anderson et.al. 1984] is utilized to avoid numerical instability that a pure central differencing may resolve at a high mesh Reynolds number. A pure upwind differencing scheme may be used but the numerical diffusion may become too large compared to the actual diffusion at a low mesh Reynolds number. A scheme that switches

from central to upwind after a critical mesh Reynolds number may also be used but the sudden change could distort the convergence to a solution. To avoid this sudden switch, the present hybrid scheme applies a weighted average of the two schemes for large mesh Reynolds numbers and reduces to a pure central differencing scheme when the mesh Reynolds is smaller than the set critical mesh Reynolds value, R_c. This R_c value should be less than or equal to 2.0 as suggested by Spalding [1972]. In the present analyses, R_c is set to 1.9 (the same value used by Chiu [1984]) and no attempt was made to fine tune this number in maximizing the stability nor for minimizing the numerical false diffusion.

For the x-momentum equation, the convective term becomes:

$$\left(V^*\frac{\partial U}{\partial Y}\right)^{t+1,n+1}_{i+1,j} = \left[V^{*\,t+1,n+1}_{x\,i+1,j+1}\cdot\frac{U^{t+1,n+1}_{i+1,j+1}-U^{t+1,n+1}_{i+1,j}}{\Delta Y^+}\cdot\frac{\Delta Y^-}{\Delta Y^+ + \Delta Y^-}\right.$$
$$\left. + V^{*\,t+1,n+1}_{x\,i+1,j}\cdot\frac{U^{t+1,n+1}_{i+1,j}-U^{t+1,n+1}_{i+1,j-1}}{\Delta Y^-}\cdot\frac{\Delta Y^+}{\Delta Y^+ + \Delta Y^-}\right]\cdot W \qquad (3.25)$$
$$+ V^{*\,t+1,n+1}_{x\,i+1,j}\cdot\frac{U^{t+1,n+1}_{i+1,j}-U^{t+1,n+1}_{i+1,j-1}}{\Delta Y^-}\cdot(1-W)\cdot A$$
$$+ V^{*\,t+1,n+1}_{x\,i+1,j+1}\cdot\frac{U^{t+1,n+1}_{i+1,j+1}-U^{t+1,n+1}_{i+1,j}}{\Delta Y^+}\cdot(1-W)\cdot B$$

where W, A, and B are determined as follows:

$$R^*_m = \frac{V^{*\,t+1,n+1}_{x\,i+1,j+1}}{\mu^{*\,t+1,n+1}_{i+3/2,j+1}}\cdot\Delta Y^-$$

$$R_m^- = \frac{V_{x\,i+1,j}^{*\,t+1,n+1}}{\mu^{*\,t+1,n+1}_{i+3/2,j}} \cdot \Delta Y^+$$

R_c = *Critical mesh Reynolds number*
If $R_m^+ > R_c$, *then* $A=1$, $B=0$, *and* $W = R_c/R_m^+$
If $R_m^- < -R_c$, *then* $A=0$, $B=1$, *and* $W = -R_c/R_m^-$
If $R_m^+ \le R_c$ *and* $R_m^- \ge -R_c$, *then* $A=0$, $B=0$, *and* $W=1$

For the y-momentum equation, the convective term becomes:

$$\left(V^* \frac{\partial V}{\partial Y}\right)^{t+1,n+1}_{i+1,j} = V_{y\,i+1,j}^{*\,t+1,n+1} \cdot \left[\frac{V_{i+1,j+1}^{t+1,n+1} - V_{i+1,j}^{t+1,n+1}}{\Delta Y_v^+} \cdot \frac{\Delta Y_v^-}{\Delta Y_v^+ + \Delta Y_v^-} + \frac{V_{i+1,j}^{t+1,n+1} - V_{i+1,j-1}^{t+1,n+1}}{\Delta Y_v^-} \cdot \frac{\Delta Y_v^+}{\Delta Y_v^+ + \Delta Y_v^-} \right] \cdot W + V_{y\,i+1,j}^{*\,t+1,n+1} \cdot \frac{V_{i+1,j}^{t+1,n+1} - V_{i+1,j-1}^{t+1,n+1}}{\Delta Y_v^-} \cdot (1-W) \cdot A + V_{y\,i+1,j}^{*\,t+1,n+1} \cdot \frac{V_{i+1,j+1}^{t+1,n+1} - V_{i+1,j}^{t+1,n+1}}{\Delta Y_v^+} \cdot (1-W) \cdot B \qquad (3.26)$$

where the mesh Reynolds numbers are computed as follows:

$$R_m^+ = \frac{V_{y\,i+1,j}^{*\,t+1,n+1}}{\mu^{*\,t+1,n+1}_{i+1,j-1/2}} \cdot \Delta Y_v^-$$

$$R_m^- = \frac{V_{y\,i+1,j}^{*\,t+1,n+1}}{\mu^{*\,t+1,n+1}_{i+1,j-1/2}} \cdot \Delta Y_v^+$$

By using these mesh Reynolds numbers, the W, A, and B variables can be determined by the same criteria as used for the x-momentum convective term.

Pressure gradient and diffusion terms:

$$\frac{\partial P}{\partial X} \quad , \quad \frac{\partial P}{\partial Y} \quad , \quad \frac{\partial}{\partial Y}\left(\mu \cdot \frac{\partial U}{\partial Y}\right) \quad , \quad \frac{4}{3} \cdot \frac{\partial}{\partial Y}\left(\mu \cdot \frac{\partial V}{\partial Y}\right)$$

A second-order accurate, central differencing is used for these terms. Note that because the staggered grid is used, the expansion points for the central differencing equations are located at (i+1, j) where the velocities are evaluated (Fig. 3.2a,b). For the x-momentum equation,

$$\left(\frac{\partial P}{\partial X}\right)^{t+1,n+1}_{i+1,j} = \frac{P^{t+1,n}_{i+2,j} - P^{t+1,n}_{i+1,j}}{\Delta X^{+}} \tag{3.27}$$

$$\left[\frac{\partial}{\partial Y}\left(\mu \cdot \frac{\partial U}{\partial Y}\right)\right]^{t+1,n+1}_{i+1,j} = \left[\mu^{t+1,n+1}_{i+3/2,j+1/2} \cdot \frac{U^{t+1,n+1}_{i+1,j+1} - U^{t+1,n+1}_{i+1,j}}{\Delta Y^{+}} - \mu^{t+1,n+1}_{i+3/2,j-1/2} \cdot \frac{U^{t+1,n+1}_{i+1,j} - U^{t+1,n+1}_{i+1,j-1}}{\Delta Y^{-}}\right] \cdot \frac{2}{\Delta Y^{+} + \Delta Y^{-}} \tag{3.28}$$

and for the y-momentum equation,

$$\left(\frac{\partial P}{\partial Y}\right)^{t+1,n+1}_{i+1,j} = \frac{P^{t+1,n}_{i+1,j} - P^{t+1,n}_{i+1,j-1}}{\Delta Y^{-}} \tag{3.29}$$

$$\left[\frac{4}{3}\frac{\partial}{\partial Y}\left(\mu^*\frac{\partial V}{\partial Y}\right)\right]^{t+1,n+1}_{i+1,j} = \left[\mu^{*\,t+1,n+1}_{i+1,j}\cdot\frac{V^{t+1,n+1}_{i+1,j+1}-V^{t+1,n+1}_{i+1,j}}{\Delta Y^{+}_{V}} - \mu^{*\,t+1,n+1}_{i+1,j-1}\cdot\frac{V^{t+1,n+1}_{i+1,j}-V^{t+1,n+1}_{i+1,j-1}}{\Delta Y^{-}_{V}}\right]\cdot\frac{4}{3}\cdot\frac{2}{\Delta Y^{+}_{V}+\Delta Y^{-}_{V}} \tag{3.30}$$

For points immediately within the solid wall, the finite-difference representation of $\frac{\partial}{\partial Y}\left(\mu^*\frac{\partial U}{\partial Y}\right)$, equation 3.28 can be a poor representation of the diffusion term due to the use of a fictitious point outside of the boundary. A better representation is to assign a point at the boundary instead. For points immediately above the lower wall, $\frac{\partial}{\partial Y}\left(\mu^*\frac{\partial U}{\partial Y}\right)$ becomes:

$$\left[\frac{\partial}{\partial Y}\left(\mu^*\frac{\partial U}{\partial Y}\right)\right]^{t+1,n+1}_{i+1,j} = \left[\mu^{*\,t+1,n+1}_{i+3/2,j+1/2}\cdot\frac{U^{t+1,n+1}_{i+1,j+1}-U^{t+1,n+1}_{i+1,j}}{\Delta Y^{+}} - \mu^{*\,t+1,n+1}_{i+3/2,j}\cdot\frac{U^{t+1,n+1}_{i+1,j}-0}{\Delta Y^{-}/2}\right]\cdot\frac{2}{\Delta Y^{+}+(\Delta Y^{-}/2)} \tag{3.31}$$

Time-dependent (unsteady) terms:

$$\rho^*\frac{\partial U}{\partial \Phi} \quad , \quad \rho^*\frac{\partial V}{\partial \Phi}$$

A first order accurate in time, backward differencing scheme is chosen for the time dependent terms. Any finite-difference scheme would require storage of all values of parameters evaluated at earlier time steps. While a second order accurate scheme could be used, such a scheme would

require values of parameters at the two previous time steps to be stored which could require excessive amount of computer memory. Whereas using a first-order accurate scheme only requires the values of the previous time step, will result in saving half the required memory size.

For the x-momentum:

$$\left(\rho^* \frac{\partial U}{\partial \Phi}\right)^{t+1,n+1}_{i+1,j} = \rho^{*\,t+1,n+1}_{i+3/2,j} \cdot \left(\frac{U^{t+1,n+1}_{i+1,j} - U^{t}_{i+1,j}}{\Delta \Phi}\right) \tag{3.32}$$

For the y-momentum:

$$\left(\rho^* \frac{\partial V}{\partial \Phi}\right)^{t+1,n+1}_{i+1,j} = \rho^{*\,t+1,n+1}_{i+1,j-1/2} \cdot \left(\frac{V^{t+1,n+1}_{i+1,j} - V^{t}_{i+1,j}}{\Delta \Phi}\right) \tag{3.33}$$

Momentum equations in Thomas Algorithm formats:

In substituting the corresponding finite-differenced terms back into the momentum equations 2.22 and 2.23, the equations can be written for (i+1, j) grid point and can be rearranged to the following formats.

The x-momentum:

$$B^u_j \cdot U^{t+1,n+1}_{i+1,j-1} + D^u_j \cdot U^{t+1,n+1}_{i+1,j} + A^u_j \cdot U^{t+1,n+1}_{i+1,j+1} = C^u_j \tag{3.34}$$

where

$$B_j^u = -\frac{V_{x\,i+1,j}^{*\,t+1,n+1}\cdot\Delta Y^{+}\cdot W}{\Delta Y^{-}\cdot(\Delta Y^{+}+\Delta Y^{-})} - \frac{V_{x\,i+1,j}^{*\,t+1,n+1}\cdot(1-W)\cdot A}{\Delta Y^{-}} - \frac{2\cdot\mu^{*\,t+1,n+1}_{\,i+3/2,j-1/2}}{\Delta Y^{-}\cdot(\Delta Y^{+}+\Delta Y^{-})} \qquad (3.35)$$

$$A_j^u = \frac{V_{x\,i+1,j+1}^{*\,t+1,n+1}\cdot\Delta Y^{-}\cdot W}{\Delta Y^{+}\cdot(\Delta Y^{+}+\Delta Y^{-})} + \frac{V_{x\,i+1,j+1}^{*\,t+1,n+1}\cdot(1-W)\cdot B}{\Delta Y^{+}} - \frac{2\cdot\mu^{*\,t+1,n+1}_{\,i+3/2,j+1/2}}{\Delta Y^{+}\cdot(\Delta Y^{+}+\Delta Y^{-})} \qquad (3.36)$$

$$D_j^u = U_{x\,i+1,j}^{*\,t+1,n+1}\cdot\frac{\Delta X_u^{-}+2\cdot\Delta X_u}{\Delta X_u\cdot(\Delta X_u^{-}+\Delta X_u)} + E_j^u \qquad \textit{for forward flow} \qquad (3.37)$$

$$D_j^u = -U_{x\,i+1,j}^{*\,t+1,n+1}\cdot\frac{\Delta X_u^{++}+2\cdot\Delta X_u^{+}}{\Delta X_u^{+}\cdot(\Delta X_u^{+}+\Delta X_u^{++})} + E_j^u \qquad \textit{for reversed flow} \qquad (3.38)$$

$$E_j^u = \left[\frac{V_{x\,i+1,j}^{*\,t+1,n+1}\cdot\Delta Y^{+}}{\Delta Y^{-}\cdot(\Delta Y^{+}+\Delta Y^{-})} - \frac{V_{x\,i+1,j+1}^{*\,t+1,n+1}\cdot\Delta Y^{-}}{\Delta Y^{+}\cdot(\Delta Y^{+}+\Delta Y^{-})}\right]\cdot W$$

$$+\frac{V_{x\,i+1,j}^{*\,t+1,n+1}\cdot(1-W)\cdot A}{\Delta Y^{-}} - \frac{V_{x\,i+1,j+1}^{*\,t+1,n+1}\cdot(1-W)\cdot B}{\Delta Y^{+}} \qquad (3.39)$$

$$+\frac{2\cdot\left(\mu^{*\,t+1,n+1}_{\,i+3/2,j+1/2}\cdot\Delta Y^{-}+\mu^{*\,t+1,n+1}_{\,i+3/2,j-1/2}\cdot\Delta Y^{+}\right)}{\Delta Y^{+}\cdot\Delta Y^{-}\cdot(\Delta Y^{+}+\Delta Y^{-})} + \frac{\rho^{*\,t+1,n+1}_{\,i+3/2,j}}{\Delta\Phi}\cdot$$

$$C_j^u = -\frac{P_{\,i+2,j}^{\,t+1,n}-P_{\,i+1,j}^{\,t+1,n}}{\Delta X^{+}} + U_{x\,i+1,j}^{*\,t+1,n+1}\cdot\left[\frac{\Delta X_u+\Delta X_u^{-}}{\Delta X_u\cdot\Delta X_u^{-}}\cdot U_{\,i,j}^{\,t+1,n+1}\right. \qquad (3.40)$$

$$\left.-\frac{\Delta X_u}{\Delta X_u^{-}\cdot(\Delta X_u^{-}+\Delta X_u)}\cdot U_{\,i-1,j}^{\,t+1,n+1}\right] + \frac{\rho^{*\,t+1,n+1}_{\,i+3/2,j}\cdot U_{\,i+1,j}^{\,t}}{\Delta\Phi} \qquad \textit{for forward flow}$$

$$C_j^u = -\frac{P_{\,i+2,j}^{\,t+1,n}-P_{\,i+1,j}^{\,t+1,n}}{\Delta X^{+}} + U_{x\,i+1,j}^{*\,t+1,n+1}\cdot\left[-\frac{\Delta X_u^{+}+\Delta X_u^{++}}{\Delta X_u^{+}\cdot\Delta X_u^{++}}\cdot U_{\,i+2,j}^{\,t+1,n}\right.$$

$$\left.+\frac{\Delta X_u^{+}}{\Delta X_u^{++}\cdot(\Delta X_u^{+}+\Delta X_u^{++})}\cdot U_{\,i+3,j}^{\,t+1,n}\right] + \frac{\rho^{*\,t+1,n+1}_{\,i+3/2,j}\cdot U_{\,i+1,j}^{\,t}}{\Delta\Phi} \qquad \textit{for reversed flow} \qquad (3.41)$$

The y-momentum:

$$B_j^v \cdot V_{i+1,j-1}^{t+1,n+1} + D_j^v \cdot V_{i+1,j}^{t+1,n+1} + A_j^v \cdot V_{i+1,j+1}^{t+1,n+1} = C_j^v \tag{3.42}$$

where

$$B_j^v = -\frac{V_{y\,i+1,j}^{*\,t+1,n+1} \cdot \Delta Y_v^+ \cdot W}{\Delta Y_v^- \cdot (\Delta Y_v^+ + \Delta Y_v^-)} - \frac{V_{y\,i+1,j}^{*\,t+1,n+1} \cdot (1-W) \cdot A}{\Delta Y_v^-} - \frac{\frac{8}{3} \cdot \mu^{*\,t+1,n+1}_{i+1,j-1}}{\Delta Y_v^- \cdot (\Delta Y_v^+ + \Delta Y_v^-)} \tag{3.43}$$

$$A_j^v = \frac{V_{y\,i+1,j}^{*\,t+1,n+1} \cdot \Delta Y_v^- \cdot W}{\Delta Y_v^+ \cdot (\Delta Y_v^+ + \Delta Y_v^-)} + \frac{V_{y\,i+1,j}^{*\,t+1,n+1} \cdot (1-W) \cdot B}{\Delta Y_v^+} - \frac{\frac{8}{3} \cdot \mu^{*\,t+1,n+1}_{i+1,j}}{\Delta Y_v^+ \cdot (\Delta Y_v^+ + \Delta Y_v^-)} \tag{3.44}$$

$$D_j^v = U_{y\,i+1,j}^{*\,t+1,n+1} \cdot \frac{\Delta X^- + 2 \cdot \Delta X}{\Delta X \cdot (\Delta X^- + \Delta X)} + E_j^v \qquad \textit{for forward flow} \tag{3.45}$$

$$D_j^v = -U_{y\,i+1,j}^{*\,t+1,n+1} \cdot \frac{\Delta X^{++} + 2 \cdot \Delta X^+}{\Delta X^+ \cdot (\Delta X^+ + \Delta X^{++})} + E_j^v \qquad \textit{for reversed flow} \tag{3.46}$$

$$E_j^v = V_{y\,i+1,j}^{*\,t+1,n+1} \cdot \left[\frac{\Delta Y_v^+ - \Delta Y_v^-}{\Delta Y_v^+ \cdot \Delta Y_v^-} \cdot W + \frac{(1-W) \cdot A}{\Delta Y_v^-} - \frac{(1-W) \cdot B}{\Delta Y_v^+} \right] + \frac{\frac{8}{3} \cdot \left(\mu^{*\,t+1,n+1}_{i+1,j} \cdot \Delta Y_v^- + \mu^{*\,t+1,n+1}_{i+1,j-1} \cdot \Delta Y_v^+ \right)}{\Delta Y_v^+ \cdot \Delta Y_v^- \cdot (\Delta Y_v^+ + \Delta Y_v^-)} + \frac{\rho^{*\,t+1,n+1}_{i+1,j-1/2}}{\Delta \Phi} \tag{3.47}$$

$$C_j^v = -\frac{P_{i+1,j}^{t+1,n} - P_{i+1,j-1}^{t+1,n}}{\Delta Y^-} + U_{y\,i+1,j}^{*\,t+1,n+1} \cdot \left[\frac{\Delta X + \Delta X^-}{\Delta X \cdot \Delta X^-} \cdot V_{i,j}^{t+1,n+1} - \frac{\Delta X}{\Delta X^- \cdot (\Delta X^- + \Delta X)} \cdot V_{i-1,j}^{t+1,n+1} \right] + \frac{\rho^{*\,t+1,n+1}_{i+1,j-1/2} \cdot V_{i+1,j}^{t}}{\Delta \Phi} \qquad \textit{for forward flow} \tag{3.48}$$

$$C_j^v = -\frac{P_{i+1,j}^{t+1,n} - P_{i+1,j-1}^{t+1,n}}{\Delta Y^-} + U_{y\,i+1,j}^{*\,t+1,n+1} \cdot \left[-\frac{\Delta X^+ + \Delta X^{++}}{\Delta X^+ \cdot \Delta X^{++}} \cdot V_{i+2,j}^{t+1,n} + \frac{\Delta X^+}{\Delta X^{++} \cdot (\Delta X^+ + \Delta X^{++})} \cdot V_{i+3,j}^{t+1,n} \right] + \frac{\rho^{*\,t+1,n+1}_{i+1,j-1/2} \cdot V_{i+1,j}^{t}}{\Delta \Phi} \qquad \textit{for reversed flow} \tag{3.49}$$

The equations 3.34 and 3.42, when written for each y-grid point at the i+1 axial station will result in a tridiagonal coefficient matrix for each equation. Combined with the proper boundary conditions (eq. 3.1, 3.2, 3.4 & 3.5), the momentum equations are resolved by the efficient Thomas Algorithm solver.

Points like the second stations and points adjacent to a solid boundary can be similarly constructed.

Finite-Difference Formulation of the Continuity Equation

If the exact pressure and temperature fields are used in the momentum equations, the resulting velocities will automatically satisfy the continuity equation. However the calculation procedure begins with estimated pressure and temperature, thus the velocity solutions from the momentum equations will not balance the continuity equation. An iterative procedure is necessary to reach the correct pressure and temperature fields. The present solution procedure adjusts the tentative velocities from the momentum equations by the continuity equation, and the corrected velocities are used to update the pressure (using the Poisson equation) and the temperature (using the energy equation). A detail description of the steady, incompressible velocity correction procedure can be found in Chiu [1984] and in Anderson et.al. [1984]; however, the present velocity

correction procedure is generalized to also work on compressible and unsteady flows.

The continuity equation (eq. 2.21) is converted by the central differencing scheme except the unsteady, time dependent term is differenced by a first-order backward scheme. The expansion point is located at the (i+1, j) dot point. For the exact velocities values (U_e^t and V_e^t) and the exact density values (ρ_e^t), the continuity equation in finite-difference form becomes:

$$\frac{U_{e\,i+1,j}^{*\,t+1,n+1} - U_{e\,i,j}^{*\,t+1,n+1}}{\Delta X_u} + \frac{V_{e\,i+1,j+1}^{*\,t+1,n+1} - V_{e\,i+1,j}^{*\,t+1,n+1}}{\Delta Y_v^*} + \frac{\rho_{e\,i+1,j}^{*\,t+1,n+1} - \rho_{e\,i+1,j}^{*\,t}}{\Delta \Phi} = 0 \qquad (3.50)$$

These exact values can be defined as the sum of the provisional values and the correction values.

$$U_{e\,i+1,j}^{*\,t+1,n+1} = U^{*\,t+1,n+1}_{i+1,j} + U_{c\,i+1,j}^{*\,t+1,n+1} \qquad (3.51)$$

$$V_{e\,i+1,j}^{*\,t+1,n+1} = V^{*\,t+1,n+1}_{i+1,j} + V_{c\,i+1,j}^{*\,t+1,n+1} \qquad (3.52)$$

$$\rho_{e\,i+1,j}^{*\,t+1,n+1} = \rho^{*\,t+1,n+1}_{i+1,j} + \rho_{c\,i+1,j}^{*\,t+1,n+1} \qquad (3.53)$$

The U^t, V^t and ρ^t are provisional solutions obtained from the momentum equations, and the ideal gas equation, while U_c^t, V_c^t and ρ_c^t are correction values. Substituting these definitions into equation 3.50 and rearranging all the correction variables to one side of the equation:

$$\frac{U_{c\,i+1,j}^{*\,t+1,n+1} - U_{c\,i,j}^{*\,t+1,n+1}}{\Delta X_u} + \frac{V_{c\,i+1,j+1}^{*\,t+1,n+1} - V_{c\,i+1,j}^{*\,t+1,n+1}}{\Delta Y_v^+} + \frac{\rho_{c\,i+1,j}^{*\,t+1,n+1} - \rho_{c\,i+1,j}^{*\,t}}{\Delta \Phi}$$

$$= -\left[\frac{U^{*\,t+1,n+1}_{i+1,j} - U^{*\,t+1,n+1}_{i,j}}{\Delta X_u} + \frac{V^{*\,t+1,n+1}_{i+1,j+1} - V^{*\,t+1,n+1}_{i+1,j}}{\Delta Y_v^+} + \frac{\rho^{*\,t+1,n+1}_{i+1,j} - \rho^{*\,t}_{i+1,j}}{\Delta \Phi} \right] \qquad (3.54)$$

$$= S_{\phi\,i+1,j}^{t+1,n+1}$$

where S_ϕ is known since U^*, V^* and ρ^* have already been calculated.

Equation 3.54 contains three unknown variables (U_c^*, V_c^* and ρ_c^*) and in order to resolve this equation, further simplifications and variable reductions are necessary.

a) $U_{c\,i,j}^{*\,t+1,n+1} = 0$

This condition is true because the velocity at the previous axial location has already satisfied the continuity equation.

b) *Irrotational velocity corrections*

This assumption permits the use of a velocity correction potential to relate U_c^* and V_c^*, such that

$$U_{c\,i+1,j}^{*\,t+1,n+1} = \left(\frac{\partial \phi}{\partial X}\right)_{i+1,j}^{t+1,n+1} = \frac{\phi_{i+2,j}^{t+1,n+1} - \phi_{i+1,j}^{t+1,n+1}}{\Delta X^+} \qquad (3.55)$$

$$V_{c\,i+1,j}^{*\,t+1,n+1} = \left(\frac{\partial \phi}{\partial Y}\right)_{i+1,j}^{t+1,n+1} = \frac{\phi_{i+1,j}^{t+1,n+1} - \phi_{i+1,j-1}^{t+1,n+1}}{\Delta Y^-} \qquad (3.56)$$

c) $\phi^{t+1,n+1}_{i+2,j} = 0$ *this implies* $V^{*\,t+1,n+1}_{c\,i+2,j} = 0$

This assumption is true as convergence is achieved.

d) $\rho^{*\,t+1,n+1}_{c\,i+1,j} = 0$, $\rho^{*\,t}_{c\,i+1,j} = 0$

These density correction terms will equal to zero when convergence is achieved.

The above four assumptions simplify equation 3.54 and can be converted in the form:

$$B^{\phi}_{j} \cdot \phi^{t+1,n+1}_{i+1,j-1} + D^{\phi}_{j} \cdot \phi^{t+1,n+1}_{i+1,j} + A^{\phi}_{j} \cdot \phi^{t+1,n+1}_{i+1,j+1} = C^{\phi}_{j} \qquad (3.57)$$

As for the boundary conditions, the no-slip condition on the solid wall and the symmetric condition at the center-line are utilized.

$$V^{*\,t+1,n+1}_{c\,i+1,j} = \frac{\phi^{t+1,n+1}_{i+1,j} - \phi^{t+1,n+1}_{i+1,j-1}}{\Delta Y^{-}} = 0 \qquad \textit{where } j = 2 \textit{ or } NJ+1$$

The Thomas Algorithm solver is used to calculate this tridiagonal matrix.

Finite-Difference Formulation of the Pressure Poisson Equation

Central differencing is used for the Poisson equation with the expansion point located at the (i+1, j) pressure point.

$$\nabla^2 P = \left[\frac{P_{i+2,j}^{t+1,n} - P_{i+1,j}^{t+1,n+1}}{\Delta X^+} - \frac{P_{i+1,j}^{t+1,n+1} - P_{i,j}^{t+1,n+1}}{\Delta X^-} \right] \cdot \frac{1}{\Delta X_u}$$

$$+ \left[\frac{P_{i+1,j+1}^{t+1,n+1} - P_{i+1,j}^{t+1,n+1}}{\Delta Y^+} - \frac{P_{i+1,j}^{t+1,n+1} - P_{i+1,j-1}^{t+1,n+1}}{\Delta Y^-} \right] \cdot \frac{1}{\Delta Y_v^*} \qquad (3.58)$$

$$= \frac{F1_{i+1,j}^{t+1,n+1} - F1_{i,j}^{t+1,n+1}}{\Delta X_u} + \frac{F2_{i+1,j+1}^{t+1,n+1} - F2_{i+1,j}^{t+1,n+1}}{\Delta Y_v^*}$$

$$= S_{P\,i+1,j}^{t+1,n+1}$$

The pressure source term, S_p, can be determined by the F1 and F2 pressure gradients resulting from the same finite-difference forms of the momentum equations (eq. 2.25 and 2.26) using the corrected velocities from the continuity equation. Combined with the Neumann boundary conditions,

$$F1_{i,j}^{t+1,n+1} = \frac{P_{i+1,j}^{t+1,n+1} - P_{i,j}^{t+1,n+1}}{\Delta X} \qquad \textit{where } i=1 \textit{ or } KPNS \qquad (3.59)$$

$$F2_{i+1,j}^{t+1,n+1} = \frac{P_{i+1,j}^{t+1,n+1} - P_{i+1,j-1}^{t+1,n+1}}{\Delta Y^-} \qquad \textit{where } j=2 \textit{ or } NJ+1 \qquad (3.60)$$

the resulting set of equations for pressure is solved by the method of Successive Over-Relaxation (SOR) by points. The use of an over-relaxation factor, usually in the range of 1.5 to 1.99, was necessary to efficiently

reach the pressure solution with minimum pressure iterations. No in depth study was conducted on determining the best over-relaxation factor to use, but a trial and error process has shown that for unsteady flow and compressible flow, a minimum value of 1.9 is required for rapid convergence compared to the value of 1.5 used for most incompressible flow types. Moreover, the pressure source term (S_p) must be under-relaxed. Normally this under-relaxation factor starts with a small value (about .01) and gradually increases with each "Global" iteration (see the Solution Procedure Section) with a maximum value of .50 used. For variable properties flow, this under-relaxation factor generally remains below .30 for the best stable convergence.

Finite-Difference Formulation of the Energy Equation

In the present study, the momentum equations and the continuity equation are solved prior to the energy equation. The expansion point for the energy equation is located at the (i+1, j) temperature point. The terms in the energy equation are differenced as follows:

$$U^{*}\frac{\partial\theta}{\partial X} \rightarrow \textit{Three point upwind scheme}$$

$$V^{*}\frac{\partial\theta}{\partial Y} \rightarrow \textit{Hybrid scheme}$$

$$\frac{\partial}{\partial Y}\left(k^{*}\frac{\partial\theta}{\partial Y}\right),\ U\frac{\partial P}{\partial X},\ \mu^{*}\left(\frac{\partial U}{\partial Y}\right)^{2},\ \frac{4}{3}\cdot\mu^{*}\left(\frac{\partial V}{\partial Y}\right)^{2} \rightarrow \textit{Central differencing}$$

$$\rho^{*}\frac{\partial\theta}{\partial\Phi},\ \frac{\partial P}{\partial\Phi} \rightarrow \textit{Backward differencing}$$

The followings are finite-difference expressions for the terms in the energy equation:

$$\left(U^{*}\frac{\partial\theta}{\partial X}\right)^{t+1,n+1}_{i+1,j} = \frac{U^{*\,t+1,n+1}_{i+1,j}\cdot\Delta X + U^{*\,t+1,n+1}_{i,j}\cdot\Delta X^{+}}{\Delta X+\Delta X^{+}}\cdot\left[\frac{\theta^{t+1,n+1}_{i+1,j}-\theta^{t+1,n+1}_{i,j}}{\Delta X}\right.$$
$$\left.-\frac{\theta^{t+1,n+1}_{i,j}-\theta^{t+1,n+1}_{i-1,j}}{\Delta X^{-}}+\frac{\theta^{t+1,n+1}_{i+1,j}-\theta^{t+1,n+1}_{i-1,j}}{\Delta X+\Delta X^{-}}\right]\quad \textit{for forward flow} \tag{3.61}$$

$$\left(U^{*}\frac{\partial\theta}{\partial X}\right)^{t+1,n+1}_{i+1,j} = \frac{U^{*\,t+1,n+1}_{i+1,j}\cdot\Delta X + U^{*\,t+1,n+1}_{i,j}\cdot\Delta X^{+}}{\Delta X+\Delta X^{+}}\cdot\left[\frac{\theta^{t+1,n}_{i+2,j}-\theta^{t+1,n+1}_{i+1,j}}{\Delta X^{+}}\right.$$
$$\left.-\frac{\theta^{t+1,n}_{i+3,j}-\theta^{t+1,n}_{i+2,j}}{\Delta X^{++}}+\frac{\theta^{t+1,n}_{i+3,j}-\theta^{t+1,n+1}_{i+1,j}}{\Delta X^{+}+\Delta X^{++}}\right]\quad \textit{for reversed flow} \tag{3.62}$$

$$\left(V^{*}\frac{\partial\theta}{\partial Y}\right)^{t+1,n+1}_{i+1,j} = \left[V^{*\,t+1,n+1}_{i+1,j+1}\cdot\frac{\theta^{t+1,n+1}_{i+1,j+1}-\theta^{t+1,n+1}_{i+1,j}}{\Delta Y^{+}}\cdot\frac{\Delta Y^{-}}{\Delta Y^{+}+\Delta Y^{-}}\right.$$
$$\left.+V^{*\,t+1,n+1}_{i+1,j}\cdot\frac{\theta^{t+1,n+1}_{i+1,j}-\theta^{t+1,n+1}_{i+1,j-1}}{\Delta Y^{-}}\cdot\frac{\Delta Y^{+}}{\Delta Y^{+}+\Delta Y^{-}}\right]\cdot W$$
$$+V^{*\,t+1,n+1}_{i+1,j}\cdot\frac{\theta^{t+1,n+1}_{i+1,j}-\theta^{t+1,n+1}_{i+1,j-1}}{\Delta Y^{-}}\cdot(1-W)\cdot A \tag{3.63}$$
$$+V^{*\,t+1,n+1}_{i+1,j+1}\cdot\frac{\theta^{t+1,n+1}_{i+1,j+1}-\theta^{t+1,n+1}_{i+1,j}}{\Delta Y^{+}}\cdot(1-W)\cdot B$$

where W, A, and B are determined as follows:

$$R_m^+ = \frac{V^{*\,t+1,n+1}_{i+1,j+1}}{\mu^{*\,t+1,n+1}_{i+1,j+1/2}} \cdot \Delta Y^-$$

$$R_m^- = \frac{V^{*\,t+1,n+1}_{i+1,j}}{\mu^{*\,t+1,n+1}_{i+1,j-1/2}} \cdot \Delta Y^+$$

R_c = *Critical mesh Reynolds number*
If $R_m^+ > R_c$, *then* $A=1$, $B=0$, *and* $W = R_c/R_m^+$
If $R_m^- < -R_c$, *then* $A=0$, $B=1$, *and* $W = -R_c/R_m^-$
If $R_m^+ \le R_c$ *and* $R_m^- \ge -R_c$, *then* $A=0$, $B=0$, *and* $W=1$

Again, the value of R_c is set equal to 1.9 for the present studies.

$$\left[\frac{\partial}{\partial Y}\left(k^*\frac{\partial\theta}{\partial Y}\right)\right]^{t+1,n+1}_{i+1,j} = \left[k^{*\,t+1,n+1}_{i+1,j+1/2}\cdot\frac{\theta^{t+1,n+1}_{i+1,j+1}-\theta^{t+1,n+1}_{i+1,j}}{\Delta Y^+} - k^{*\,t+1,n+1}_{i+1,j-1/2}\cdot\frac{\theta^{t+1,n+1}_{i+1,j}-\theta^{t+1,n+1}_{i+1,j-1}}{\Delta Y^-}\right]\cdot\frac{2}{\Delta Y^+ + \Delta Y^-} \tag{3.64}$$

$$\left(\rho^*\frac{\partial\theta}{\partial\Phi}\right)^{t+1,n+1}_{i+1,j} = \rho^{*\,t+1,n+1}_{i+1,j}\cdot\left(\frac{\theta^{t+1,n+1}_{i+1,j}-\theta^{t}_{i+1,j}}{\Delta\Phi}\right) \tag{3.65}$$

$$\left(U\frac{\partial P}{\partial X}\right)^{t+1,n+1}_{i+1,j} = \frac{U^{t+1,n+1}_{i+1,j}\cdot\Delta X + U^{t+1,n+1}_{i,j}\cdot\Delta X^+}{(\Delta X+\Delta X^+)^2}\cdot\left[\left(P^{t+1,n}_{i+2,j}-P^{t+1,n}_{i+1,j}\right)\cdot\frac{\Delta X}{\Delta X^+} + \left(P^{t+1,n}_{i+1,j}-P^{t+1,n}_{i,j}\right)\cdot\frac{\Delta X^+}{\Delta X}\right] \tag{3.66}$$

$$\left(\frac{\partial P}{\partial\Phi}\right)^{t+1,n+1}_{i+1,j} = \frac{P^{t+1,n}_{i+1,j}-P^{t}_{i+1,j}}{\Delta\Phi} \tag{3.67}$$

$$\left[\mu^{*}\left(\frac{\partial U}{\partial Y}\right)^{2}\right]_{i+1,j}^{t+1,n+1} = \left[\frac{\left(U_{i+1,j+1}^{t+1,n+1} - U_{i+1,j-1}^{t+1,n+1}\right)\cdot\Delta X + \left(U_{i,j+1}^{t+1,n+1} - U_{i,j-1}^{t+1,n+1}\right)\cdot\Delta X^{+}}{(\Delta X + \Delta X^{+})\cdot(\Delta Y^{+} + \Delta Y^{-})}\right]^{2} \cdot \mu^{*\,t+1,n+1}_{i+1,j} \qquad (3.68)$$

$$\left[\frac{4}{3}\mu^{*}\left(\frac{\partial V}{\partial Y}\right)^{2}\right]_{i+1,j}^{t+1,n+1} = \frac{4}{3}\cdot\mu^{*\,t+1,n+1}_{i+1,j}\cdot\left[\frac{V_{j+1,j+1}^{t+1,n+1} - V_{j+1,j}^{t+1,n+1}}{\Delta Y_{v}^{+}}\right]^{2} \qquad (3.69)$$

By substituting equations 3.61 through 3.69 into equation 2.24, the energy equation can be rearranged in the form:

$$B_{j}^{\theta}\cdot\theta_{i+1,j-1}^{t+1,n+1} + D_{j}^{\theta}\cdot\theta_{i+1,j}^{t+1,n+1} + A_{j}^{\theta}\cdot\theta_{i+1,j+1}^{t+1,n+1} = C_{j}^{\theta} \qquad (3.70)$$

Combined with the constant wall temperature boundary condition (eq. 3.3) and the upper symmetric boundary condition (eq. 3.6), the resulting Tridiagonal matrix is again solved by the efficient Thomas Algorithm method. However, for locations such as the 2nd x-station and points adjacent to the boundary walls, a 1st order upwind scheme for the axial convective term and a more accurate scheme for the thermal diffusion terms are used instead.

Solution Procedure

Based upon the Partially Parabolized Navier-Stokes (PPNS) equations solution procedure for incompressible, steady, subsonic flows [Anderson

et.al.,1984], the present technique is extended to cover unsteady, compressible flow problems. For the steady flow calculation, the solution procedure found in Chiu's [1984] thesis is used with the energy equation resolved at each "Global" iteration (see Fig. 3.5) for variable fluid properties. As for unsteady flows, an extra "Time Step" loop is required to calculate the time dependent terms and to advance time increments in the fluctuation cycle. A flow chart of the present computer code is provided in Figure 3.5 and the computational steps are explained in the following summaries.

Steady flow solution procedure summary:

S1) Read all the input information, nondimensionalize all the variables, and initialize all counters. The normalized fluid properties are set temporarily to 1.0 while the initial boundary conditions at the channel's inlet are determined.

S2) The "Global" iteration level is advanced by one to n+1 level.

S3) Advance the axial counter "i" by one to the next stream-wise station. Use the n iteration level results or initial guessed values (for the first "Global" iteration) of the pressure and fluid properties, and determine the tentative U and V velocities by evaluating the momentum equations with the appropriate boundary conditions.

S4) Next, the continuity equation is balanced to correct the

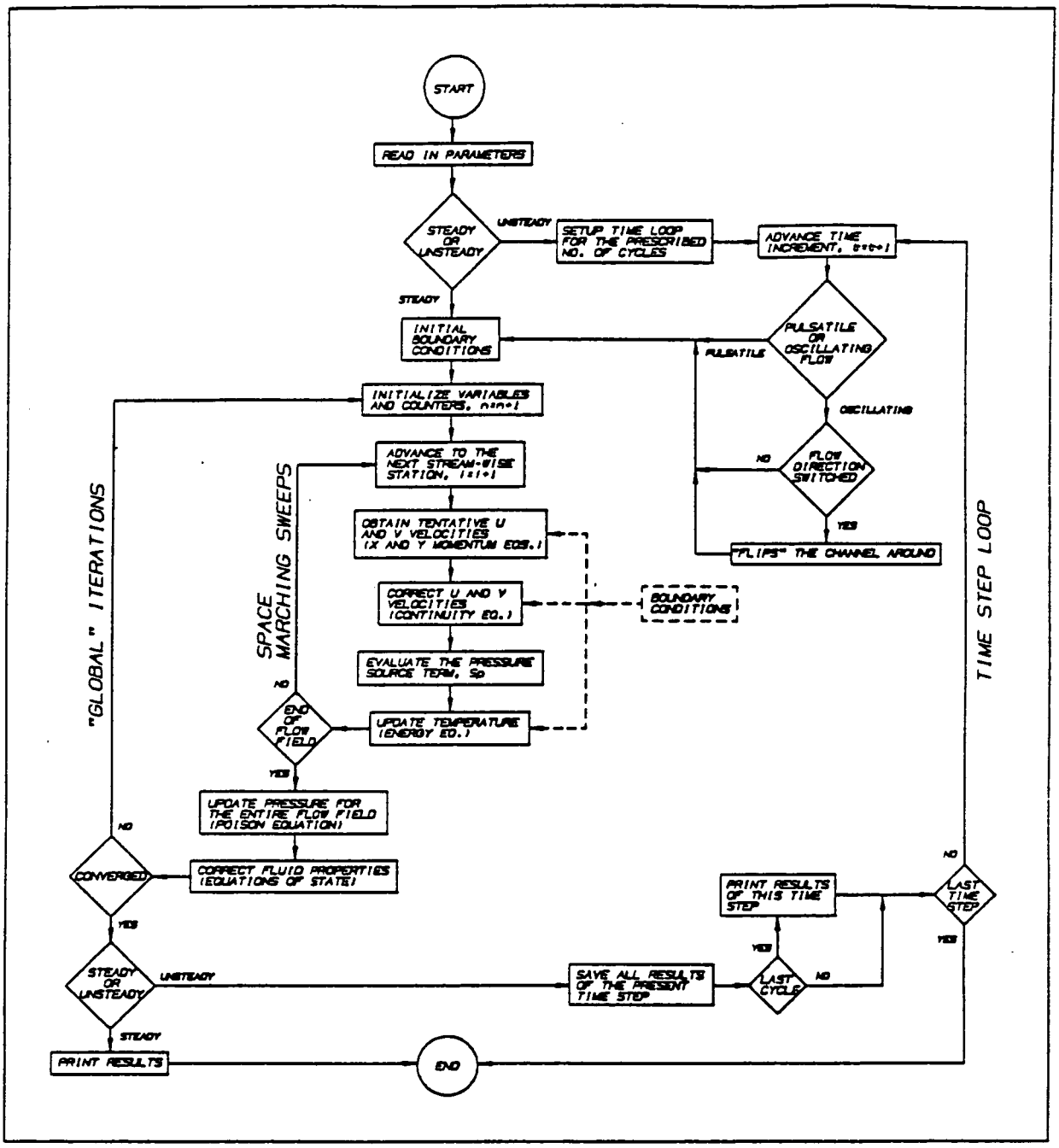

Figure 3.5: Computational flow chart of the present solution procedure for the steady and unsteady fluid flows.

provisional U and V velocities. This requires the transformation of the correction velocities into the correction velocity potential ϕ and solving equation 3.57. The residual mass source term is determined.

S5) Utilizing the corrected U and V velocities at the n+1 iteration level, the pressure source term S_p is evaluated at the i+1 axial station.

S6) For problems involving transfer of heat, the revision of the thermal field is performed. The temperature is updated to the n+1 iteration level via solving the energy equation with the latest values of U and V.

S7) Steps (S3) to (S6) are repeated until the end of the channel is reached. The U and V velocities, the temperature, and the S_p are revised for the entire flow channel to the n+1 "Global" iteration level.

S8) The pressure of the entire flow field is updated to n+1 iteration level by utilizing the Poisson equation with the previously calculated S_p values and the Neumann boundary conditions. As mentioned earlier, this pressure correction process uses the Successive Over-Relaxation (SOR) by points method. The SOR method is an iterative procedure which sweeps the entire channel for the number of prescribed iterations.

S9) The last step in this n+1 "Global" iteration corrects the fluid properties by computing the equations of state with the latest temperature and pressure.

S10) This "Global" iteration process repeats from step (S2) to (S9) until the residual mass ratio is converged to an acceptable, imposed percentage value (usually .1%) or until the number of "Global" iterations exceed the maximum prescribed value. In either case, the program prints out the detail flow results into the appropriate output files. A warning message will appear in these files if the program exit was due to an insufficient number of imposed iterations.

Unsteady flow solution procedure summary:

The unsteady flow solution procedure is based upon the steady flow solution steps with an additional time loop. At each time step, the unsteady PPNS equations are solved in a similar manner as in the steady flow procedure. The unsteady flow procedure is slightly different for pulsatile flow from the oscillating flow. For pulsatile flow, the fluid always travels in one direction, hence the numerical marching sweep moves from left to right. As for the oscillating flow, the fluid moves forward for half the fluctuating cycle and then it moves backward in the second half. During the backward flow period, instead of marching in the reversed direction, the present code "flips" the channel around as the input axial

velocity direction is changed. This actually simulates the same reversed marching but, this way, the code maintains the left to right sweeping direction throughout the oscillating cycle. The following outline briefly describes the unsteady flow solution procedure:

U1) The program reads all input information and sets up the "time step" loop. The program also determines if the flow is pulsatile or oscillating and sets up the appropriate inlet velocity fluctuation values.

U2) For the first time step, the computation domain is solved as steady flow with the corresponding unsteady inlet velocity value. This is done because no previous results are available for the time dependent calculations and also it will provide initial guesses of the velocities, temperature, and pressure for the next time step.

U3) The time step counter "t" advances by one and the computation domain is solved by the steps (S2) to (S10) from the steady flow procedure except the governing equations contain the time dependent, unsteady terms. The sinusoidal time variation of the inlet velocity profile is used in these calculations.

U4) If the inlet flow reverses its direction on the next time step, the solutions are saved in a reverse order matter which simulates "flipping" the channel around in a physical sense.

Otherwise, the present solution is normally saved for the next time step calculations.

U5) Steps (U3) and (U4) are repeated until the total number of time steps are completed. The results are printed for the last oscillating cycle.

CHAPTER IV

DISCUSSION OF RESULTS

The presentation of the results are divided into three sections. The first section compares and validates the present steady flow solutions with existing literature on incompressible, thermally expandable and compressible fluid conditions. These variable fluid property validations determine and evaluate the accuracy of the present computer code prior to the examination of the pulsating flows and oscillating flows discussed in sections two and three, respectively. For reference purposes, the abbreviations and the numbers denoted in square brackets coincide with the flow runs performed in this chapter, and the detailed input parameters are summarized in Appendix-A.

Code Validation

Steady Incompressible - Hydrodynamically Developing Flows:

Based on Chiu's [1984] thesis, the present computer code is first validated for its ability to produce accurate steady incompressible flow solutions prior to any code modifications on handling thermally expandable, compressible properties and unsteady conditions. In Figures 4.1.1a and 4.1.1b, the residual mass source is plotted with respect to the number of "Global" iterations for the Reynolds numbers of 40 and 100, respectively. The figures reveal the convergence characteristic behaviors for steady incompressible flows at four axial locations from the area of flow development to the fully-developed downstream region. Having the over-relaxation factor for the pressure correction terms set at 1.5, the present code performed 53 "Global" iterations to reach the 0.2% mass flow convergence criterion at the two low Reynolds number flows considered. As for the high Reynolds number flows (Re=2000 or greater), substantial reduction in the required number of iterations (20 or less) was observed.

The gradual velocity evolvements from the uniform inlet profile to the fully-developed, parabolic form are illustrated in Figures 4.1.2a and 4.1.2b. For both of the Reynolds numbers (40 and 100), the fully-developed streamwise velocity reached a maximum normalized value of 1.5 at the channel's center-line which meets the theoretical value for steady incompressible flows between parallel plates. Notice also that the near wall over-shoot velocities in the initial developing profiles correspond to

a)

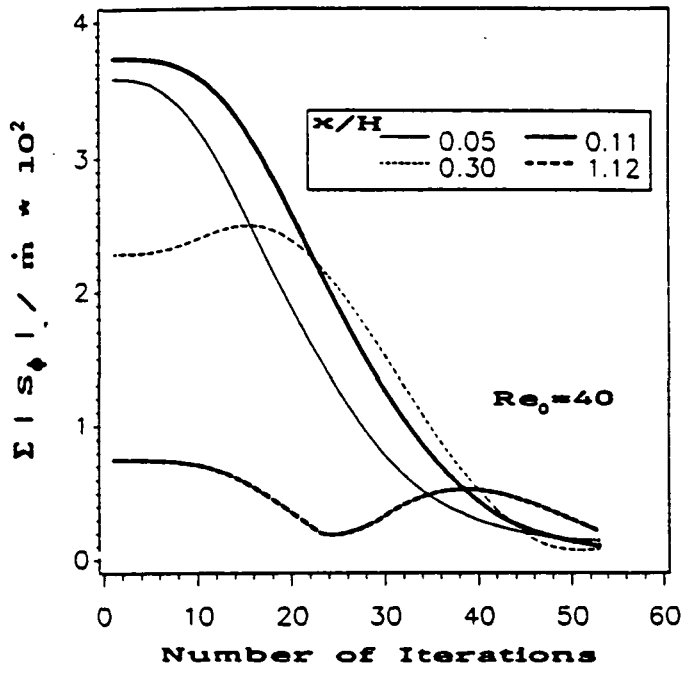

b)

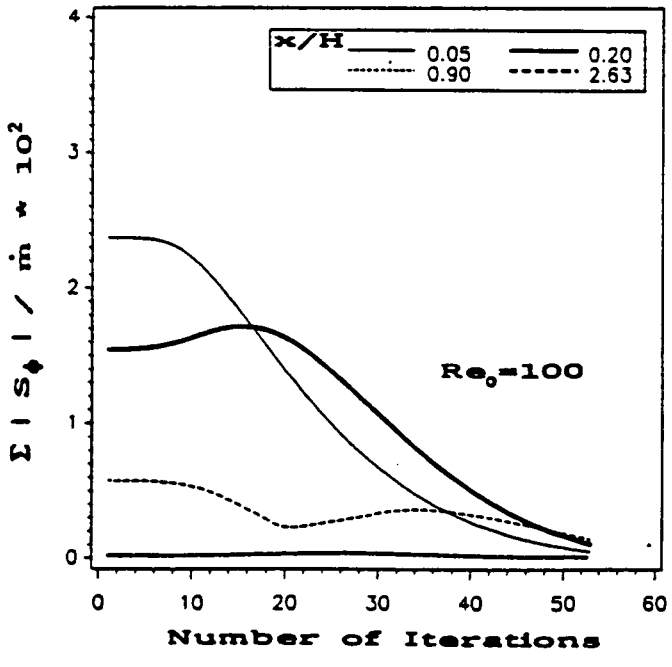

Figure 4.1.1: Convergence characteristics for incompressible, steady flow at:
a) Re_0=40 [SI-1].
b) Re_0=100 [SI-2].

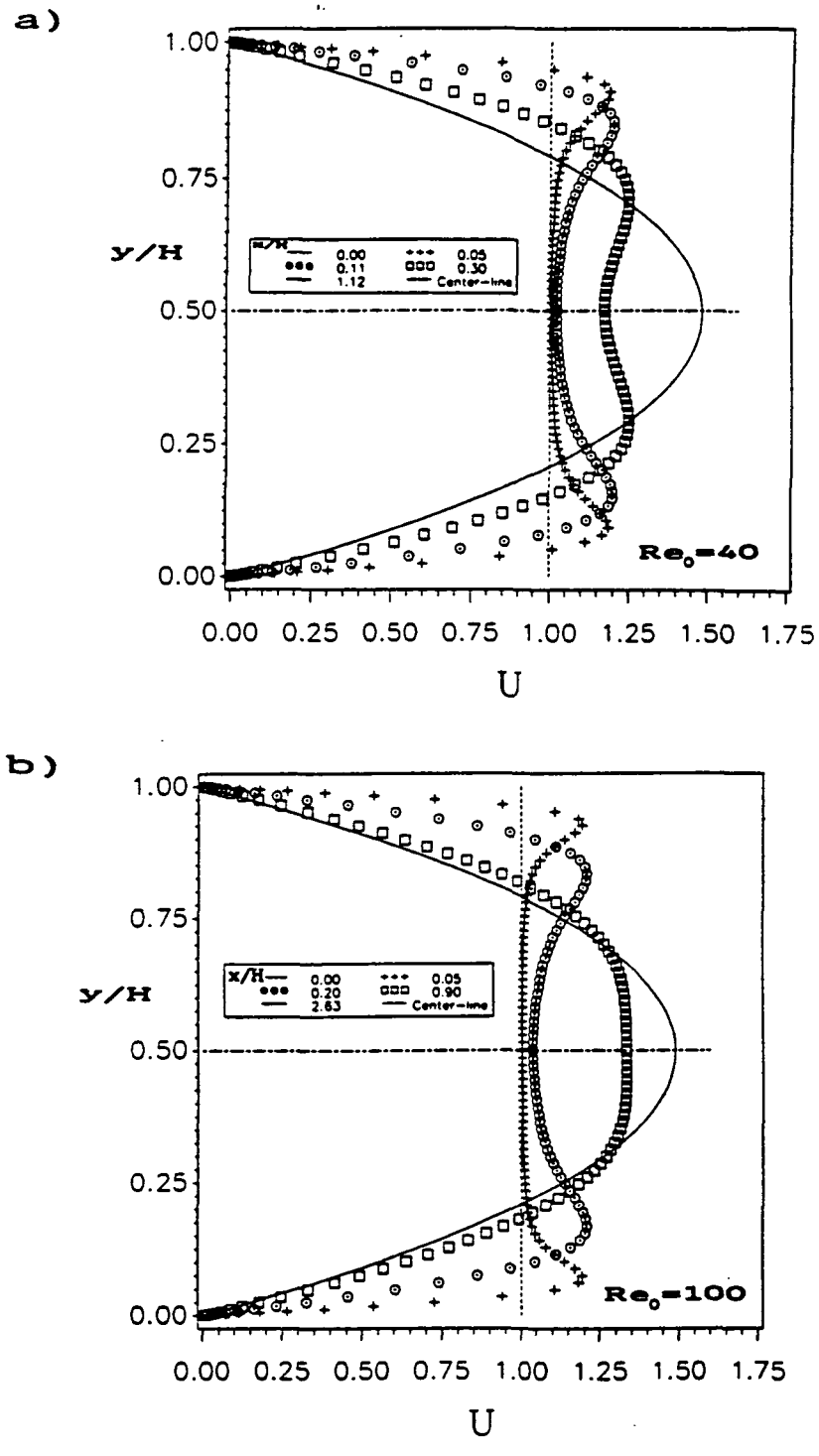

Figure 4.1.2: **Developing velocity profiles of the incompressible, steady flow through parallel plates at:**
a) Re_0=40 [SI-1].
b) Re_0=100 [SI-2].

Brandt's [1966] findings and to those who have solved the Navier-Stokes equations. The over-shoot velocity comparison with data from Brandt are listed in Table 4.1.1; good agreements on the location and on the maxima value of the over-shoot velocity were established.

Listed in Table 4.1.2 are center-line velocity values situated at various axial distance from the channel's entrance. Two Reynolds numbers (40 and 1000) were examined and compared with data from Brandt; the agreements of the results were well below half a percent difference.

An exercise to determine the steady hydrodynamic entrance length was performed for three Reynolds numbers: 40, 100 and 1000. The hydrodynamic entrance length is defined as the required distance from the channel's inlet for U-velocity to reach 99 percent of the fully-developed U_{max} value of 1.5. The outcomes are listed and compared with other literature in Table 4.1.3.

The boundary layer theory results from Schlichting [1960] estimated shorter hydrodynamic entrance lengths than others who resolved the Navier-Stokes equations. At a Reynolds number of 40, Schlichting's prediction was 28.9% less than the present result; while at the higher Reynolds number of 1000, the difference decreased to 17.2% less than the present result. From this comparison, it is clear that the boundary layer theory provides satisfactory approximations of the Navier-Stokes equations only when the Re_0 is high.

The present hydrodynamic entrance length results are in good agreement with data from Brandt [1966], Morihara [1973] and Narang [1976].

Table 4.1.1: Location and Amplitude of the maxima of the steady, developing velocity profiles compared with data from Brandt [1966] at different Re_0 and axial locations [SI-1, SI-5].

Re_0	x/H	U_{max}			$(y/H)_{max}$		
		Brandt [1966]	Present	Diff.	Brandt [1966]	Present	Diff.
40	0.1	1.129	1.201	6.4%	0.125	0.146	+.021
	0.2	1.168	1.223	4.7%	0.214	0.222	+.008
	0.3	1.210	1.249	3.2%	0.290	0.288	−.002
	0.4	1.261	1.278	1.3%	0.369	0.345	−.024
1000	0.1	1.163	1.151	−1.0%	0.048	0.044	−.003
	1.0	1.151	1.145	−0.5%	0.180	0.178	−.002
	3.0	1.223	1.222	−0.1%	0.315	0.328	+.013
	5.0	1.288	1.290	0.2%	0.435	0.468	+.033

Table 4.1.2: Center-line velocity comparison of steady, developing flow between parallel plates with data from Brandt [1966] at different Re_0 and axial locations [SI-1, SI-5].

Re_0	x/H	U (at y/H=.5)		
		Brandt [1966]	Present	Diff.
40	0.1	1.022	1.021	−0.1%
	0.2	1.085	1.079	−0.6%
	0.3	1.169	1.166	−0.3%
	0.4	1.254	1.250	−0.3%
1000	0.1	1.003	1.003	0.0%
	1.0	1.100	1.096	−0.3%
	3.0	1.211	1.213	0.2%
	5.0	1.288	1.290	0.2%

Table 4.1.3: Comparison of the steady hydrodynamic entrance length for flows in parallel plates with data from Schlichting [1960], Brandt [1966], Morihara [1973], Chen [1973] and Narang [1976]. [SI-1, SI-2, SI-5]

Re_o	Hydrodynamic Entrance Length, x/H (at $U=.99*U_{max}$)					
	Present	Schlichting [1960]	Brandt [1966]	Morihara [1973]	Chen [1973]	Narang [1976]
40	1.125	0.8	1.13	1.118	1.50	1.11
100	2.630	2.0	----	----	2.91	2.72
1000	24.15	20.0	22.4	----	----	24.42

Methods used by the earlier investigators:

Schlichting : Boundary Layer Theory
Brandt : Full Navier-Stokes Equation
Morihara : Numerical Solution, Quasilinearized
Chen : Momentum Integral Method
Narang : Linearizing the Inertia Terms

Table 4.1.4: Steady mean nusselt number for equal and constant walls' temperature at Re_0=100 and Pr=.72 compared with data from Hwang [1973]. [SI-2]

Re_o	x/H	Mean Nu_o		
		Hwang [1973]	Present	Diff.
100	.500	14.90	16.74	12.3%
	1.25	10.96	11.72	6.9%
	2.13	9.593	10.03	4.6%

As for Chen [1973], who solved the Navier-Stokes equations by the momentum integral method, he predicted longer hydrodynamic entrance lengths than the present work (at Re_0=40 which was 33% longer, and at Re_0=100 which was 10.6% longer).

Steady Incompressible - Simultaneously Developing Flows:

In this segment the heat transfer analysis in the channel, provided by the constant wall temperature is examined with both velocity and temperature profiles developing simultaneously.

The first validation case has a constant temperature for the upper and lower walls while the flow is at Re_0=100 and the fluid has a Pr=.72. The temperature evolvement from the inlet uniform profile to the fully-developed parabolic shape is illustrated in Figure 4.1.3a, while Figure 4.1.3b plots the present heat transfer coefficient results along with the available numerical data from Hwang [1973]. The Nusselt numbers are in good agreement between the two predictions with a maximum difference of 12% after the channel's length x/H=.5 (see Table 4.1.4). Moreover, the present local Nusselt number curve approaches the analytical fully-developed value of 7.54 downstream.

The second heat transfer validation run has constant and different wall temperatures, where the upper plate heats the fluid while the lower plate cools it. Figure 4.1.4a shows the results of the developing temperature profiles along 5 axial locations from the entrance to the fully-

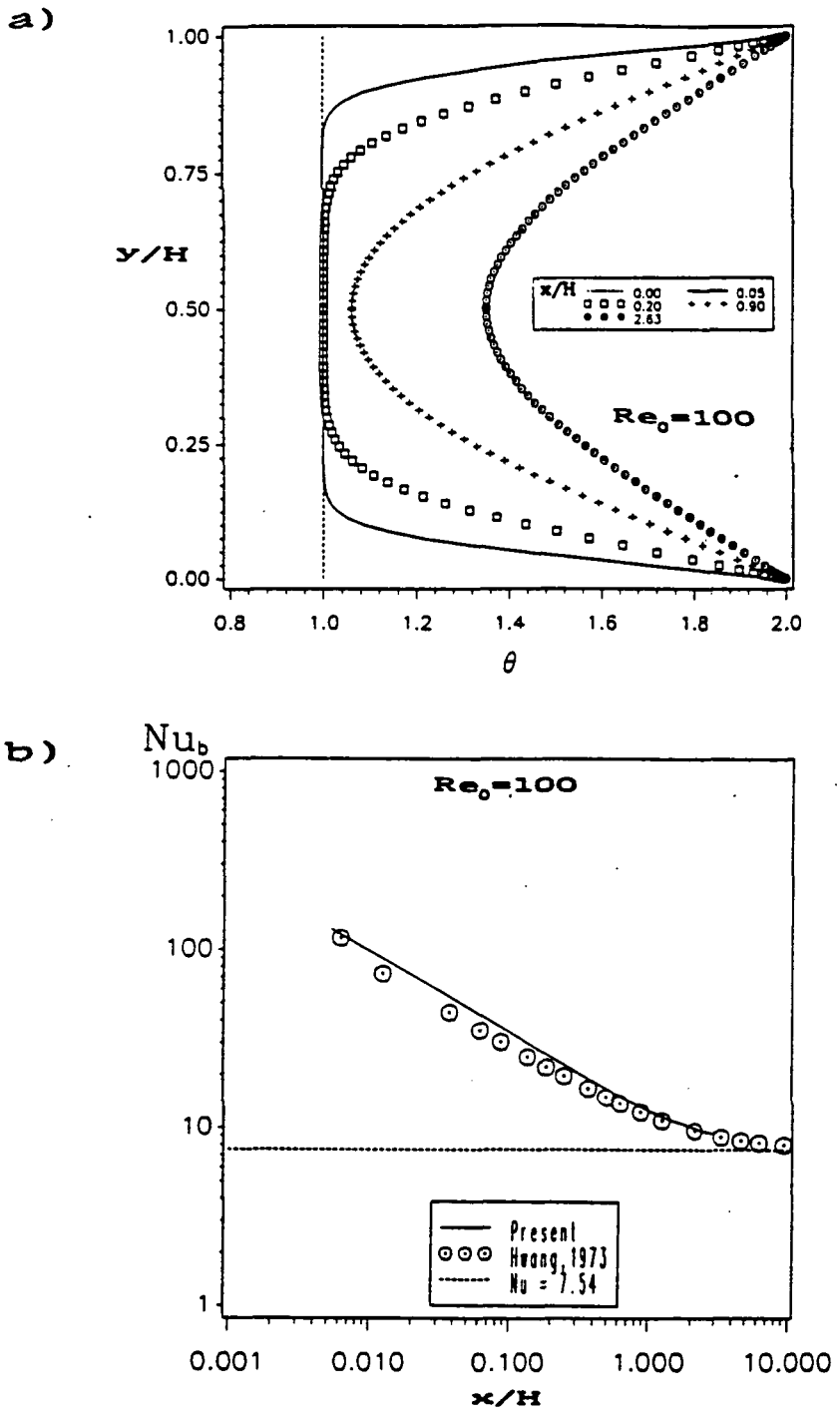

Figure 4.1.3: Heat Transfer in simultaneously developing, steady flow with equal and constant wall temperatures at Re_0=100 [SI-2]:
a) Temperature profiles at different developing axial locations.
b) Comparison of the present average heat transfer coefficient with data from Hwang [1973].

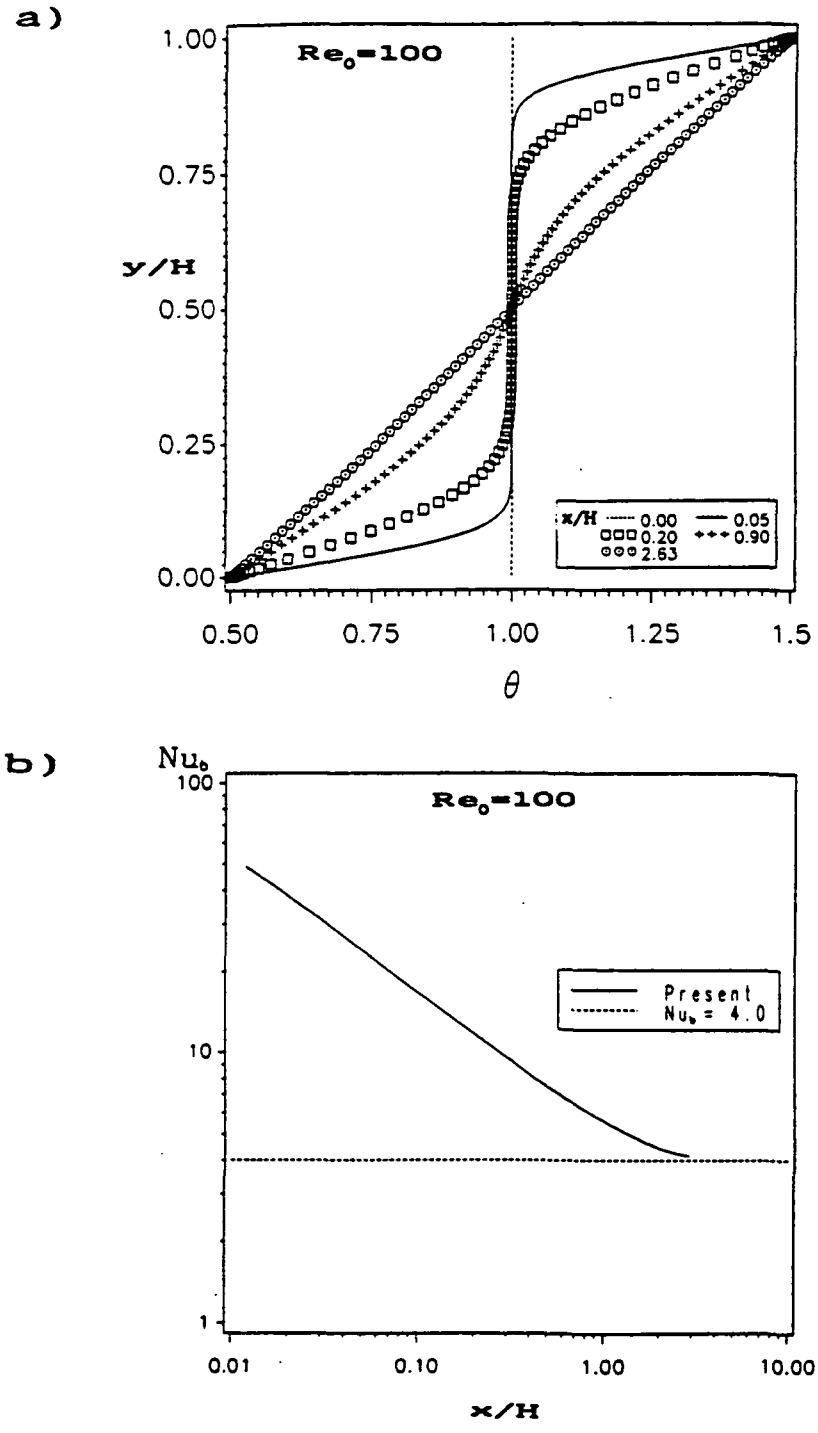

Figure 4.1.4: Heat Transfer in simultaneously developing, steady flow with different but constant wall temperatures at Re_0=100 [SI-3]:
a) Temperature profiles at different developing axial locations.
b) Comparison of the present developing local Nusselt number with the theoretical, fully-developed value (Nu_b=4.0).

developed downstream region. The developing temperature profiles began uniformly and then as the input heat flux from the upper wall balanced with the heat flux ejected into the lower wall, the temperature profile transformed into a fully-developed diagonal linear line with the end-points equal to the upper and lower wall temperatures. In Figure 4.1.4b, the local Nusselt number curve is plotted and the curve approaches the fully-developed theoretical value of 4.0.

Steady Thermally Expandable Flows:

For the thermally expandable flows, the work done by Schade and McEligot [1971] is used as the comparison reference. In their paper, the predictions of the fluid properties were determined by the ideal gas law, the viscosity power law and the conductivity power law. These equations are defined in Chapter 2 (eqs. 2.9, 2.10 and 2.12) with the α and β values listed in Table 2.1 for air.

Two Reynolds numbers, 144 and 2000, were chosen for this extensive validation study, and the fluid was assumed to have the properties of air and four T_w/T_0 ratios (.5 cooling, 1.0 incompressible, 2.0 and 5.0 heating) were examined for each Re_0. The resulting comparisons are shown in Figures 4.1.5 to 4.1.7.

In Figures 4.1.5a (Re_0=144) and 4.1.5b (Re_0=2000), the local apparent friction is compared with data from Schade and McEligot at T_w/T_0=1.0 (incompressible), 0.5 and 2.0 (thermally expandable). The present

a)

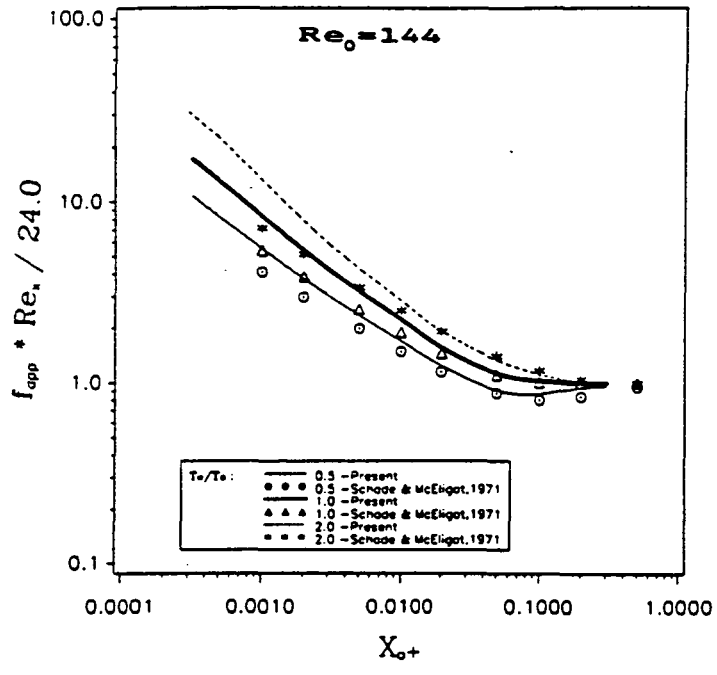

b)

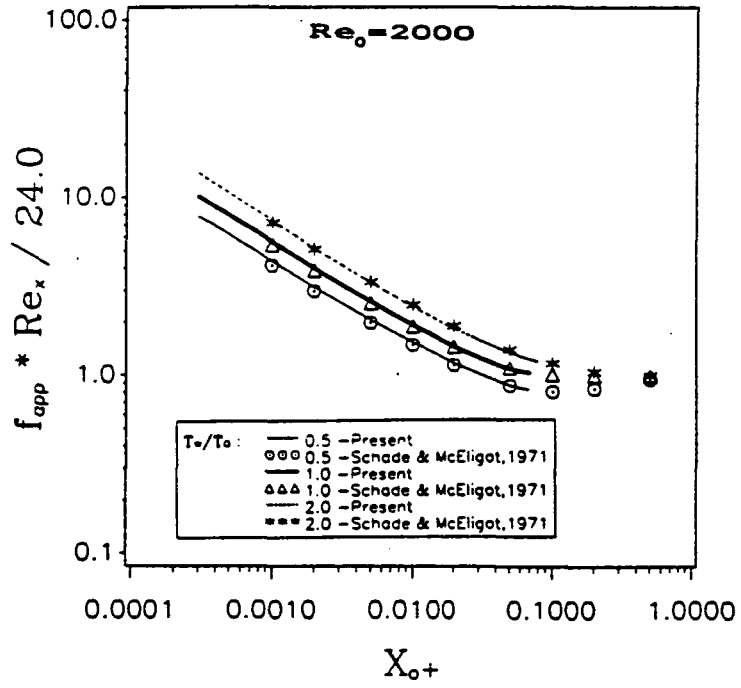

Figure 4.1.5: Local apparent friction comparison of steady flow in the channel with data from Schade & McEligot [1971] at different wall/inlet temperature ratios, T_w/T_0=1.0 (incompressible), 0.5 and 2.0 (thermally expandable):
a) Re_0=144 [SI-4, ST-1, ST-2].
b) Re_0=2000 [SI-5, ST-4, ST-9].

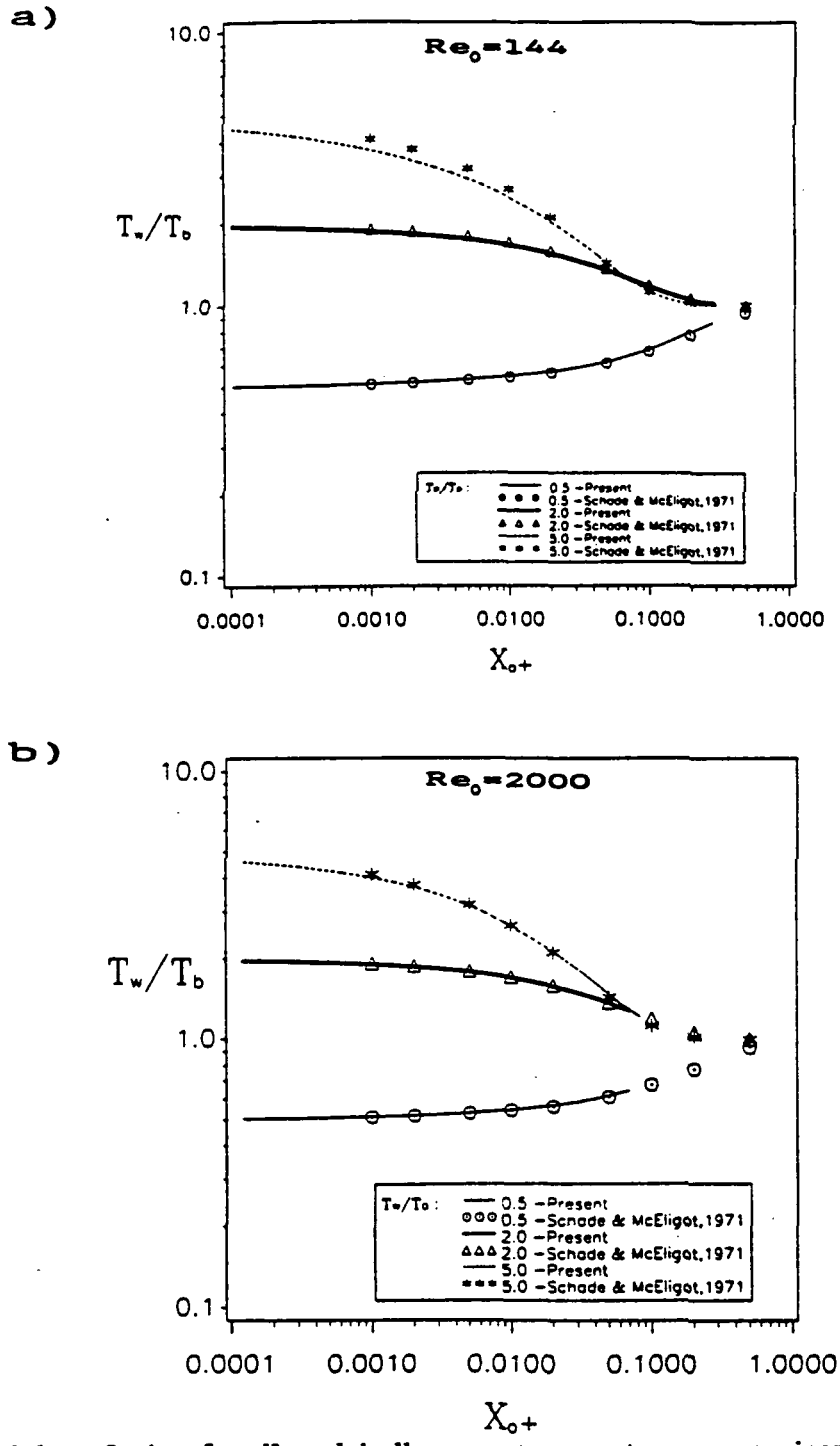

Figure 4.1.6: Ratio of wall and bulk-mean temperature comparison in the channel with data from Schade & McEligot [1971] at different wall/inlet temperature ratios, T_w/T_0=0.5, 2.0, 5.0 (thermally expandable):
a) Re_0=144 [ST-1, ST-2, ST-3].
b) Re_0=2000 [ST-4, ST-9, ST-10].

a)

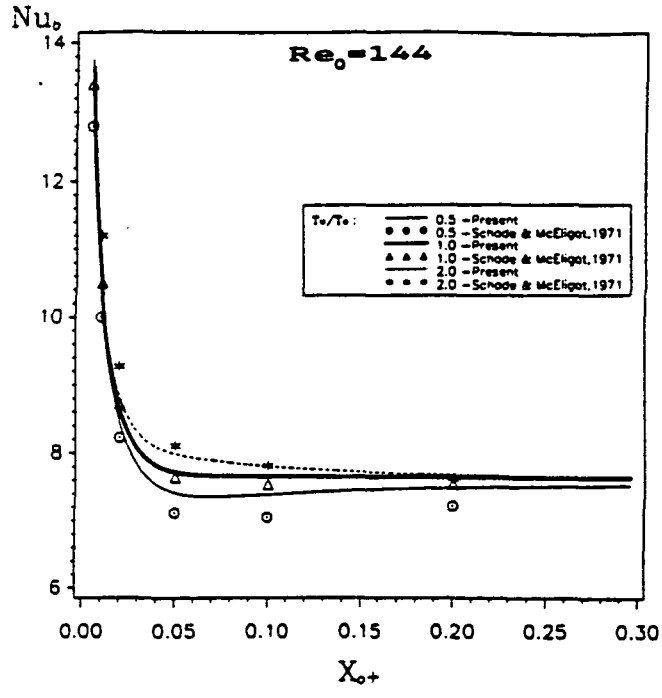

b)

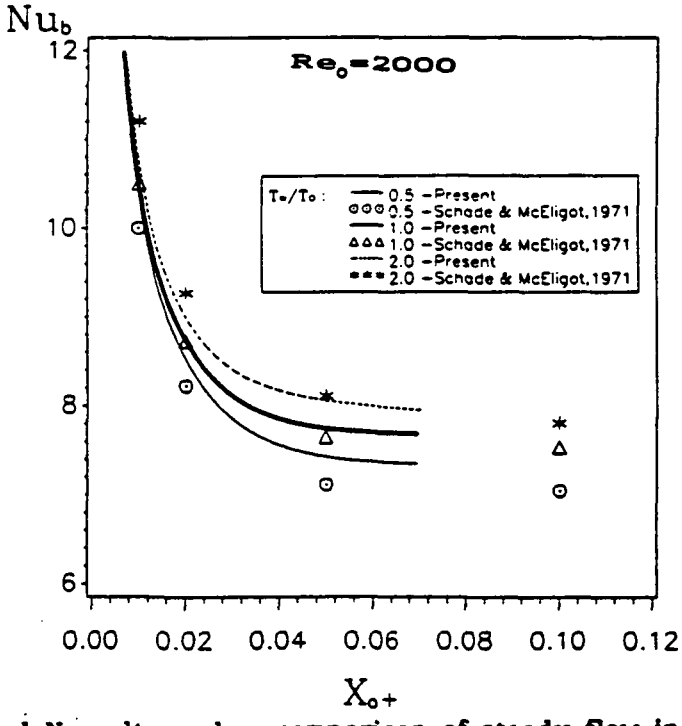

Figure 4.1.7: **Local Nusselt number comparison of steady flow in the channel with data from Schade & McEligot [1971] at different wall/inlet temperature ratios, T_w/T_0=1.0 (incompressible), 0.5 and 2.0 (thermally expandable):**
a) Re_0=144 [SI-4, ST-1, ST-2].
b) Re_0=2000 [SI-5, ST-4, ST-9].

predictions suggest an increase in friction as the fluid is heated while a decrease is observed when cooled; this observation corresponds to Schade and McEligot's findings. This friction behavior is directly related to the increase in viscosity as the temperature of the gas rises and vice versa. Such variation in friction can only be recorded when the fluid properties are allowed to vary; whereas for incompressible flows, a single friction curve would have been generated regardless of the wall/inlet temperature ratio. A quantitative comparison revealed that the present friction predictions compared well with data from Schade and McEligot [1971] especially at the higher Re_0 (2000), (see Table 4.1.5).

The wall and bulk-mean temperature ratios versus the normalized axial locations are plotted in Figures 4.1.6a (Re_0=144) and 4.1.6b (Re_0=2000). Again, the comparisons with data from Schade and McEligot are in excellent agreement, even at high heating of T_w/T_0=5.0.

The local Nusselt number comparison at wall/inlet temperature ratios of 1.0 (incompressible), 0.5 and 2.0 (thermally expandable) are shown in Figures 4.1.7a (Re_0=144) and 4.1.7b (Re_0=2000). Notice that the Nusselt number curve increases as a result of a higher wall/inlet temperature ratio and the opposite effect is shown for cooling. This behavior is caused by the fluid's conductivity increase with the temperature rise which offers less thermal resistance against heat flow into the fluid. Quantitative comparison with Schade and McEligot's data resulted in an agreement within a 5.0% difference (see Table 4.1.5).

Table 4.1.5: Comparison of the predictions for steady, thermally expandable flow between the present and the data from Schade & McEligot [1971]. [ST-1, ST-2, ST-4, ST-9]

Re_o	T_w/T_o	X_o^+	$f_{app} * Re_x / 24.0$			T_w / T_b			Nu_b		
			Schade **	Present	Diff. (%)	Schade **	Present	Diff. (%)	Schade **	Present	Diff. (%)
144	0.5	.01	1.48	1.68	13.5	.541	.548	1.3	10.0	10.3	3.0
		.05	.872	.911	4.5	.609	.621	2.0	7.12	7.42	4.2
		.10	.806	.874	8.4	.676	.690	2.1	7.05	7.40	5.0
		.20	.841	.944	12.2	.776	.798	2.8	7.21	7.49	3.9
	2.0	.01	2.49	2.69	8.0	1.70	1.65	-2.9	11.2	11.0	-1.8
		.05	1.40	1.31	-6.4	1.37	1.34	-2.2	8.11	8.01	-1.2
		.10	1.17	1.12	-4.3	1.19	1.17	-1.7	7.81	7.80	-0.1
		.20	1.05	1.01	-3.8	1.06	1.05	-0.9	7.62	7.68	0.8
2000	0.5	.01	1.48	1.54	4.0	.541	.545	0.7	10.0	10.3	3.0
		.02	1.14	1.18	3.5	.561	.568	1.2	8.22	8.55	4.0
		.05	.872	.883	1.3	.609	.619	1.6	7.12	7.43	4.4
	2.0	.01	2.49	2.45	-1.8	1.70	1.68	-1.2	11.2	10.8	-3.6
		.02	1.90	1.81	-4.7	1.58	1.56	-1.3	9.27	9.09	-1.9
		.05	1.40	1.35	-3.6	1.37	1.36	-0.7	8.11	8.06	-0.6

Note: ** - Schade & McEligot [1971] used the Power Laws for properties variations.

Steady Compressible Flows:

When dealing with the steady high velocity flow, previous investigators mainly studied external supersonic flow or subsonic flow over a flat plate or a cross section of an air foil. To the author's knowledge, no internal subsonic compressible flow through parallel plates was published. Hence, the results in this segment are new findings for internal compressible flows.

Ensuring the code generates accurate compressible solutions, validation runs were established at the fixed Re_0=2000 and M=0.25 tested under four different wall/inlet temperature ratios. Note that when dealing with compressible flow, the stagnation enthalpy or the stagnation temperature (since C_p is assumed constant) is taken as the thermal energy reference of the fluid. By setting the inlet fluid stagnation temperature equal to 300K, the four different wall temperatures (note: the static wall temperature is equivalent to the stagnation wall temperature due to zero-velocity at the wall) were set constant at 294K and 298K (fluid cooling, cases A and B, respectively), 300K (no heat transfer, case C) and 302K (fluid heating, case D). The static and stagnation temperature profiles are presented in Figures 4.1.8a to 4.1.8d where each figure represents solutions at a specific streamwise location: a) x/H=1.10, b) x/H=5.16, c) x/H=19.9 and d) x/H=59.7.

The present computer code handled the static temperature as one of the primitive variables (see eq. 2.5); therefore, the direct results from the energy equation are static temperature solutions which are plotted as solid

a)

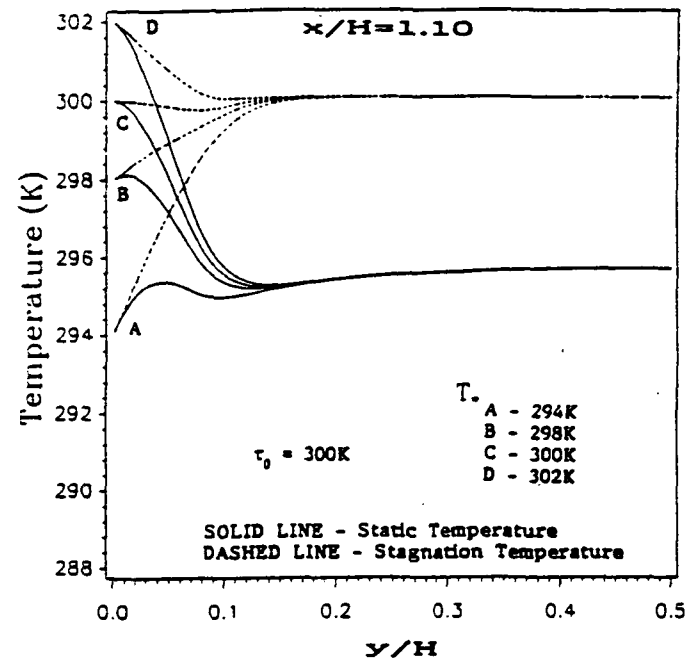

b)

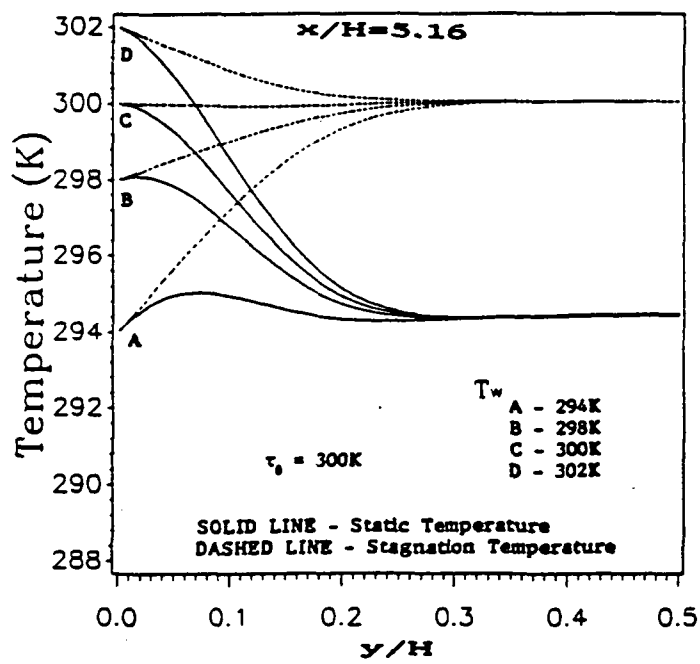

Figure 4.1.8: Comparison between static and stagnation temperature distribution in the channel at high-velocity (M=.25) steady flow for a fluid with Pr=1.0 [SC-1 to SC-4]:
a) x/H=1.10.
b) x/H=5.16.

c)

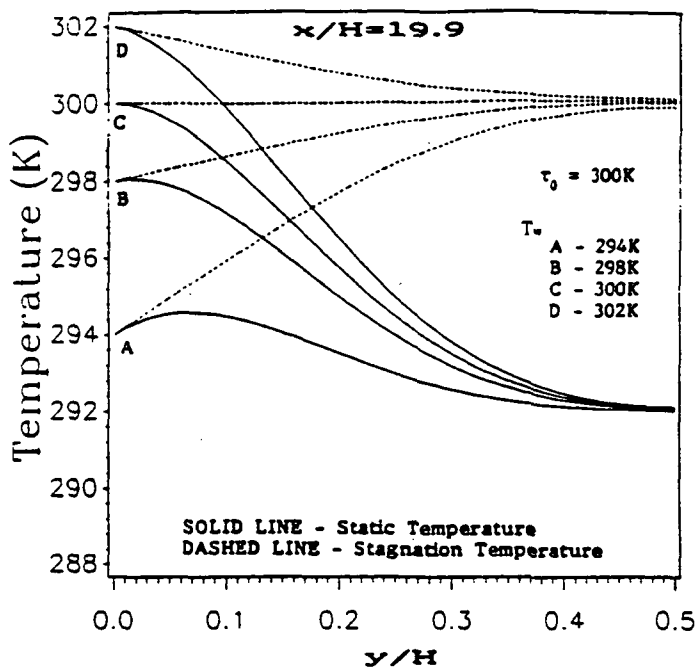

d)

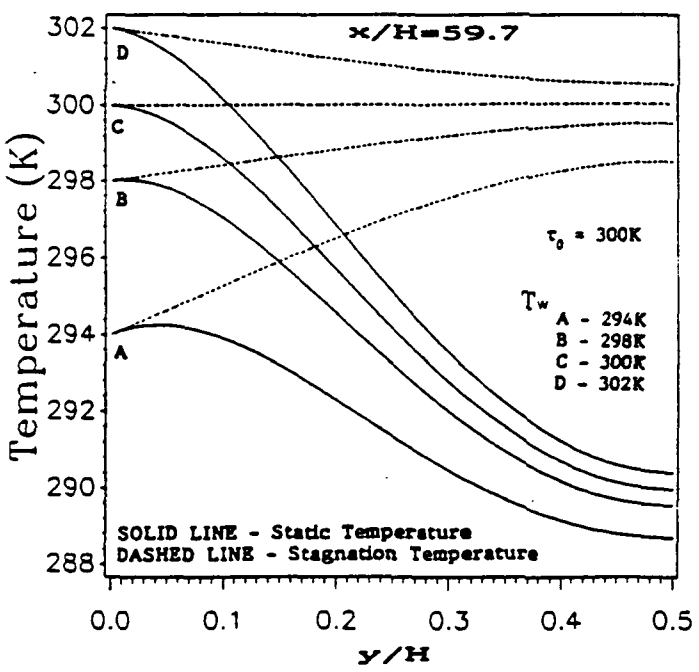

Figure 4.1.8: (cont.)

c) x/H=19.9.
d) x/H=59.7.

lines in figure 4.1.8a to 4.1.8d. Notice for all four T_w/τ_0 ratios examined, the static temperature results (solid lines) gradually decreased in value with respect to the axial length. By intuitive observation, one would conclude that there was fluid energy loss into the wall at all four of the wall/inlet temperature ratios studied. However, by close examination of the temperature gradients at the wall suggested otherwise; gradients for cases A and B indicate negative heat flux to the fluid (cooling), case D revealed a positive heat flux to the fluid (heating), while case C had a zero wall temperature gradient hinting no heat was transferred. The same conclusions can also be derived by viewing the stagnation temperature curves represented as the dashed lines in the plots.

As explained in Chapter two, the difference between the static and stagnation temperature curves is that the static temperature measures only the thermal energy in the fluid while the stagnation temperature accounts for the total energy (thermal and kinetic energy). Whereas, in the incompressible and thermally expandable fluid assumptions, the thermal energy outweighs the kinetic energy. The two types of energy in the high velocity compressible flow are comparable. For this very reason, the decrease of static temperature with respect to the axial length was caused by the conversion of thermal energy into kinetic energy, and if the static temperature was examined alone, it could have led to a false conclusion on the heat flux direction. This validation analysis agrees with the similar qualitative findings for high speed external flow over a flat plate [Kays and Crawford, 1980].

The main objective of this thesis is to explore the fluid compressibility effects on internal flows as compared with the incompressible and thermally expandable assumptions. The following study examines the behavior of the apparent friction factor and the heat transfer coefficient under various Mach number flows. The fluid air was selected for the investigation with the Re_0 fixed at 2000. Two sets of steady flow with heat transfer were performed, one set on fluid heating (T_w/τ_0=1.5) and one set on fluid cooling (T_w/τ_0=.67). Five fluid property models were considered: a) incompressible; b) thermally expandable; c) compressible, M=.05; d) M=.10 and e) M=.25.

The predictions of the apparent friction are plotted in Figure 4.1.9a (for the heating case) and Figure 4.1.9b (for the cooling case). As expected, substantial differences exist between the incompressible and thermally expandable predictions. For the T_w/τ_0=1.5 heating case, the thermally expandable run predicted around 12.5% higher in friction than the incompressible results throughout the channel; while for the T_w/τ_0=.67 cooling case, about 15.5% lower was found (see Table 4.1.6). As noted in the previous thermally expandable flow discussion, this behavior is primarily caused by the temperature dependence of the fluid viscosity (eq. 2.11).

Since thermally expandable flow is actually compressible flow with the Mach number assumed as zero, the friction factor comparison with compressible flows at low Mach numbers shows marginal differences. For both fluid heating and cooling studies, thermally expandable results differ

a)

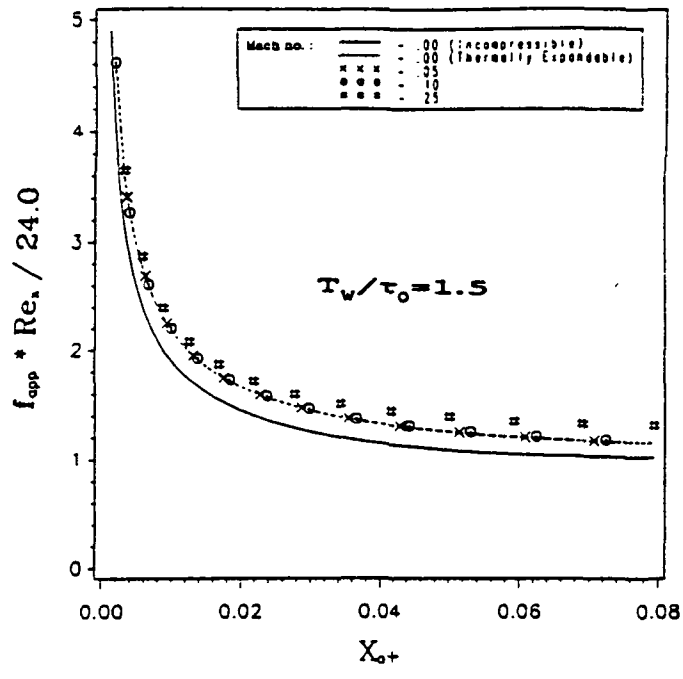

b)

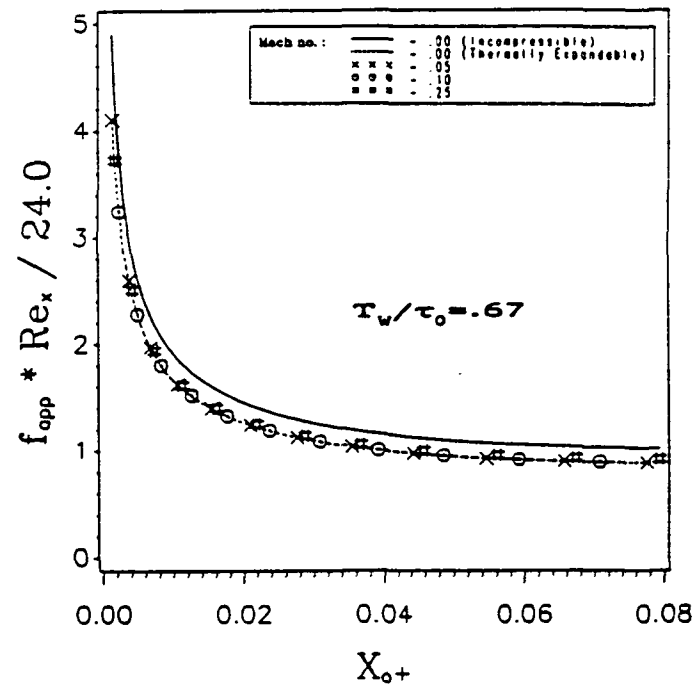

Figure 4.1.9: **Comparison of steady local apparent friction in the channel at different Mach numbers, M=0.0 (incompressible), 0.0 (thermally expandable), .05, .10 and .25 (compressible):**
a) T_w/τ_0=1.5 [SI-8, ST-8, SC-8, SC-9, SC-10].
b) T_w/τ_0=.67 [SI-6, ST-5, SC-5, SC-6, SC-7].

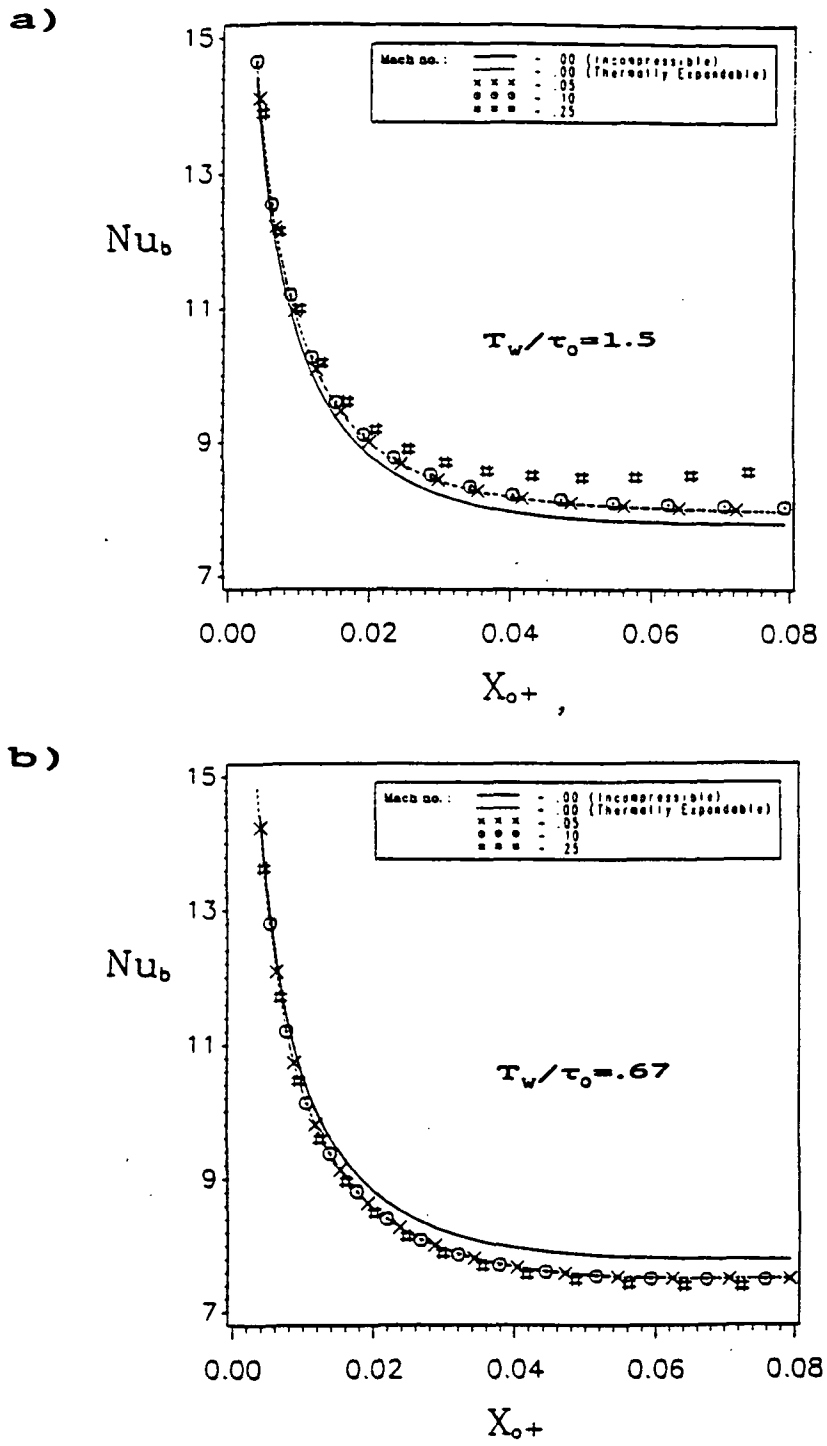

Figure 4.1.10: Comparison of steady local Nusselt number in the channel at different Mach numbers, M=0.0 (incompressible), 0.0 (thermally expandable), .05, .10 and .25 (compressible):
a) T_w/τ_0=1.5 [SI-8, ST-8, SC-8, SC-9, SC-10].
b) T_w/τ_0=.67 [SI-6, ST-5, SC-5, SC-6, SC-7].

Table 4.1.6: Steady apparent friction comparison between incompressible, thermally expandable, and compressible air flow for Re_0=2000 and different Mach numbers [SI-6, SI-8, ST-5, ST-8, SC-5 to SC-10].

T_w/T_o	X_o^+	$F_{app}^+Re_z/24.0$					Diff. from T.E. (%)			
		Inc.	T.E.	Mach No.			Inc.	Mach No.		
				.05	.10	.25		.05	.10	.25
1.5	.02	1.449	1.662	1.665	1.675	1.762	-12.8	0.2	0.8	6.0
	.04	1.149	1.323	1.327	1.339	1.449	-13.2	0.3	1.2	9.2
	.06	1.051	1.199	1.203	1.215	1.344	-12.3	0.3	1.3	12.1
	.08	1.019	1.145	1.149	1.161	1.309	-11.0	0.3	1.4	14.3
.667	.02	1.449	1.258	1.259	1.262	1.288	15.2	0.1	0.3	2.4
	.04	1.149	0.993	0.994	0.998	1.027	15.7	0.1	0.5	3.4
	.06	1:051	0.906	0.908	0.911	0.942	16.0	0.2	0.6	4.0
	.08	1.019	0.881	0.882	0.886	0.919	15.7	0.1	0.6	4.3

Table 4.1.7: Steady Nusselt number comparison between incompressible, thermally expandable, and compressible air flow for Re_0=2000 and different Mach numbers [SI-6, SI-8, ST-5, ST-8, SC-5 to SC-10].

T_w/T_o	X_o^+	Nu_b					Diff. from T.E. (%)			
		Inc.	T.E.	Mach No.			Inc.	Mach No.		
				.05	.10	.25		.05	.10	.25
1.5	.02	8.819	9.008	9.017	9.044	9.273	-2.1	0.1	0.4	2.9
	.04	7.968	8.183	8.194	8.228	8.533	-2.6	0.1	0.5	4.3
	.06	7.820	8.027	8.041	8.083	8.505	-2.6	0.2	0.7	6.0
	.08	7.798	7.977	7.994	8.046	8.620	-2.2	0.2	0.9	8.1
.667	.02	8.819	8.563	8.560	8.552	8.495	3.0	-0.1	-0.1	-0.8
	.04	7.968	7.680	7.676	7.666	7.593	3.8	-0.1	-0.2	-1.1
	.06	7.820	7.520	7.516	7.504	7.411	4.0	-0.1	-0.2	-1.4
	.08	7.798	7.510	7.505	7.491	7.382	3.8	-0.1	-0.3	-1.7

Note:
Inc. – Incompressible
T.E. – Thermally Expandable
Mach No. – Compressible flow at the given Mach number

less than 1.5% when compared with compressible flows at Mach numbers below .10 . However as the Mach number increases to .25, the compressible friction factors surpass the thermally expandable predictions regardless of the wall/inlet temperature ratios; Table 4.1.6 discloses the differences that were as high as 14.3% (at X_0^+=.08 and T_w/τ_0=1.5).

Next, the Nusselt number predictions are plotted in Figure 4.1.10a (heating) and Figure 4.1.10b (cooling). Similar behaviors as found in the friction factor apply to the Nusselt number except the differences between compressible and thermally expandable results are lower in percentage magnitude (see Table 4.1.7).

Via this steady compressible flow study, the following observation was noted. For low Mach number flows (below M=.10), the thermally expandable fluid assumption predicts excellent results as compared to the actual compressible flow. However, as the Mach number of the flow increases (above M=.25), the thermally expandable predictions will no longer be valid to model such high-velocity compressible flow.

Pulsating Flows

With the preliminary steady flow investigation conducted and the code validated, the next research stage implements the time-dependent terms into the governing equations. In this section, the periodic pulsating

unsteady flow is examined in detail. In part, the present pulsating incompressible and thermally expandable results were presented and published at the fourth International Symposium on Transport Phenomena in Heat and Mass Transfer at Sydney, Australia [Ibrahim and Kwan, 1990].

Pulsating Incompressible - Hydrodynamically Developing Flows:

The code modifications for unsteady flow are first checked with the incompressible pulsating results from Siegel and Perlmutter [1962]. The pulsating flow boundary conditions described in Chapter two are similar to the boundary conditions employed by Siegel and Perlmutter, except they applied the sinusoidally pulsating pressure gradients at the channel's inlet rather than the pulsating velocity (eq. 2.14). Ensuring the two inlet velocity matches, Siegel and Perlmutter's equations were used to derive the present imposed velocity fluctuation amplitude, ψ. The ψ's are listed in Table 4.2.1 for various Valensi numbers with the imposed pressure gradient fluctuation amplitude equal to one.

The predicted phase angle between the axial pressure gradient and the mean velocity are compared between the present work versus the closed form incompressible solution given by Siegel and Perlmutter [1962] in Table 4.2.2. For the low and high Valensi numbers considered, the comparison shows excellent agreement.

At the fixed Re_{ref}=2000, the Figures 4.2.1a (ω^+=0.08) and 4.2.1b (ω^+=32.0) illustrate the fully developed, normalized fluctuating velocity

Table 4.2.1: Parameter ψ used in determining the inlet pulsating velocity conditions (eq. 2.14) for different ω^* to match the conditions used by Siegel & Perlmutter [1962] [PI-1 to PI-4].

ω^*	ψ
0.08	1.0000
8.0	0.7775
32.0	0.2984
200.0	0.0543

Table 4.2.2: Comparison between present work and data from Siegel & Perlmutter [1962] on the phase angle difference between cross-sectional average velocity and axial pressure gradient (incompressible pulsating flow, fully developed) [PI-1 to PI-4].

ω^*	Phase Angle Difference (degrees)	
	Siegel & Perlmutter [1962]	Present
0.08	0.0	0.0
8.00	38.5	38.7
32.0	70.5	71.0
200.0	83.5	83.1

a)

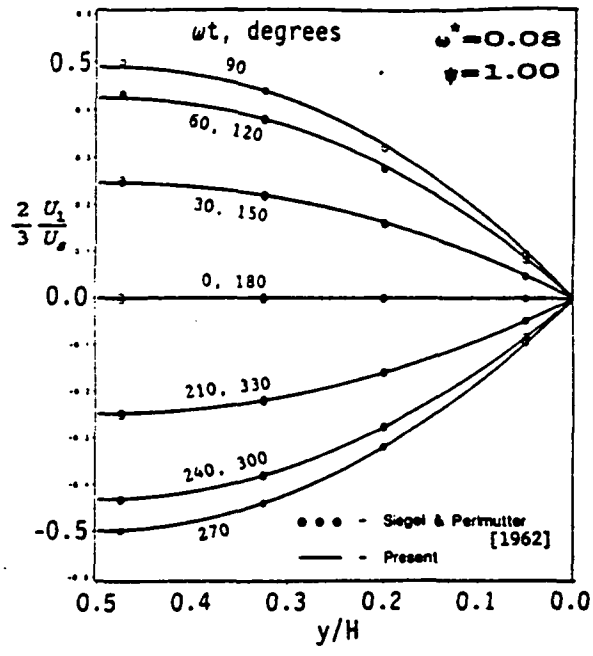

b)

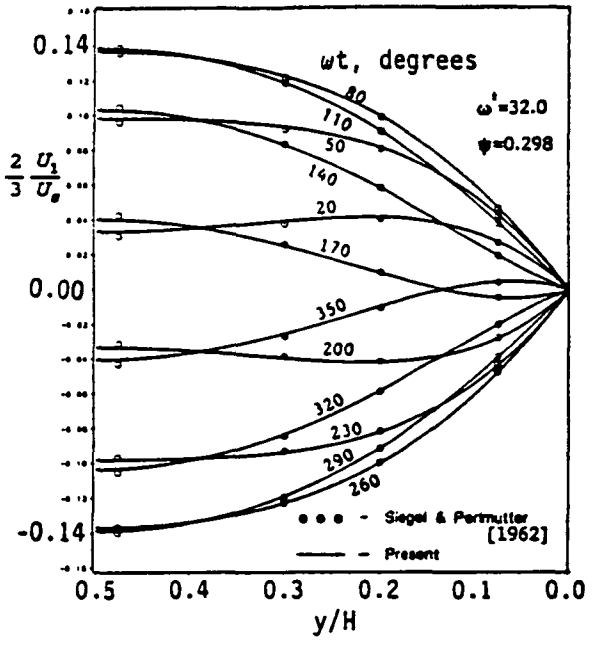

Figure 4.2.1: Cross sectional fluctuating velocity profiles compared between present work and data from Siegel & Perlmutter [1962] (fully developed, incompressible pulsating flow, Re_{nom}=2000):
a) ω^*=0.08, ψ=1.00 [PI-1].
b) ω^*=32.0, ψ=0.298 [PI-3].

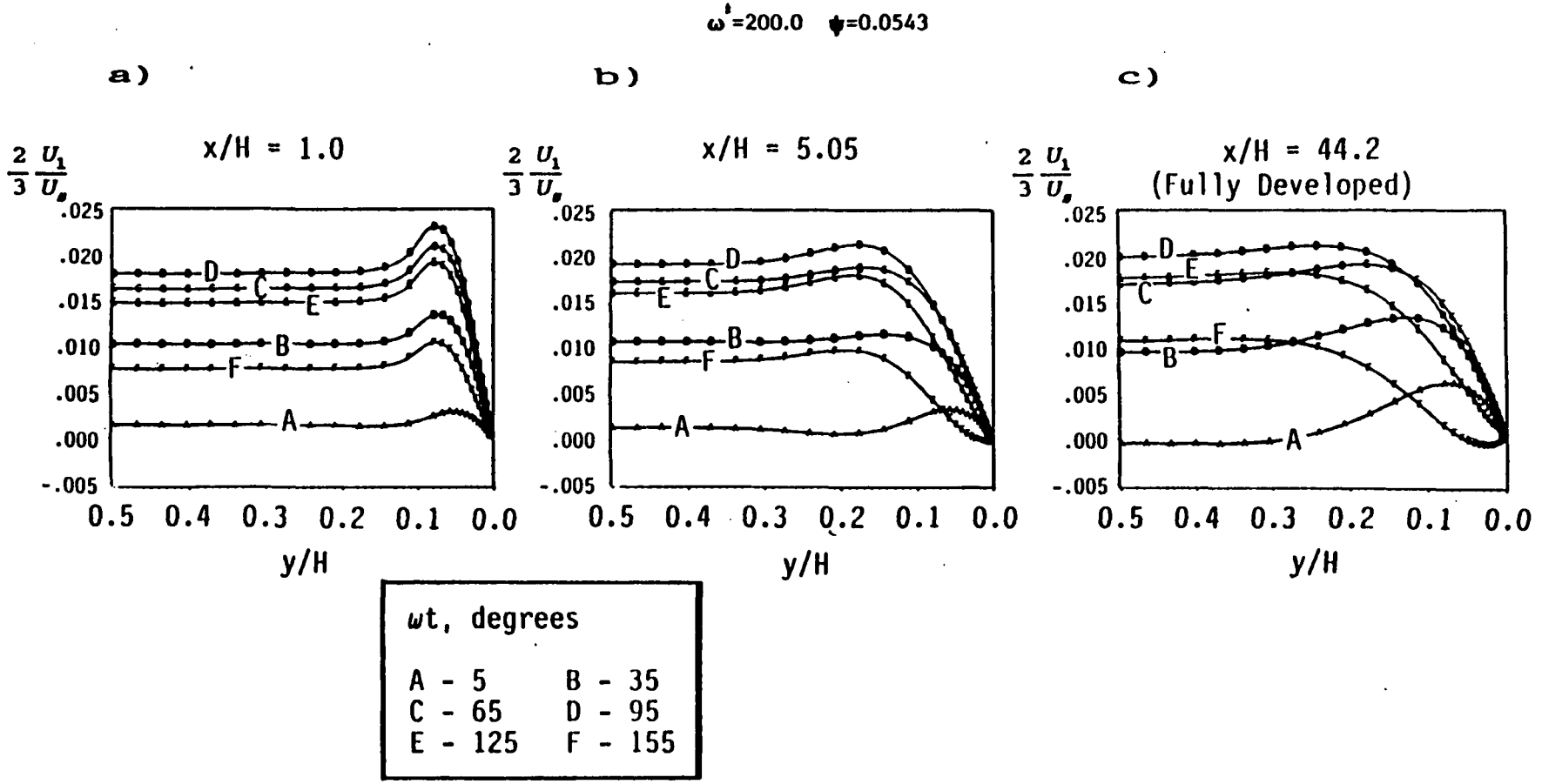

Figure 4.2.2: Fluctuating velocity versus distance from the wall at different axial locations (incompressible pulsating flow, Re_{mean}=2000, ω'=200, ψ=0.0543) [PI-4]:
a) x/H=1.00.
b) x/H=5.05.
c) x/H=44.2 (fully developed).

versus the normalized distance from the wall. The figures are comparisons between the present work and data from Siegel and Perlmutter; excellent agreement was obtained.

A study of the developing velocity profile for pulsating flow was carried out for Re_{ref}=2000 and ω^{+}=200. Figures 4.2.2a to 4.2.2c show the predicted normalized fluctuating velocity versus normalized distance from the wall at three different axial locations. An overshoot has been noticed in the velocity profile near the duct inlet which dissipates downstream. This observation is similar qualitatively to Creff's et.al. [1983,1985] findings for pulsating flow in circular tubes.

Pulsating Incompressible - Thermally Developing Flows: (Slug Flow Approximation)

Figures 4.2.3a and 4.2.3b show the predicted Nusselt number versus the normalized axial distance comparing the present work with data from Siegel and Perlmutter [1962] (Slug flow approximation). The Valensi numbers considered are 0.08 (Figure 4.2.3a) and 32.0 (Figure 4.2.3b). It should be noted that Figure 4.2.3a shows the instantaneous Nusselt number, while Figure 4.2.3b shows the fluctuating Nusselt number (instantaneous minus steady state value). The figures clearly illustrate that the agreement between the present work and the closed form solution for thermally developing with slug flow approximation is excellent. It can be seen from the figures that, at a low Valensi number, the Nusselt number decreases monotonically as x increases (at all values of ωt - see Figure

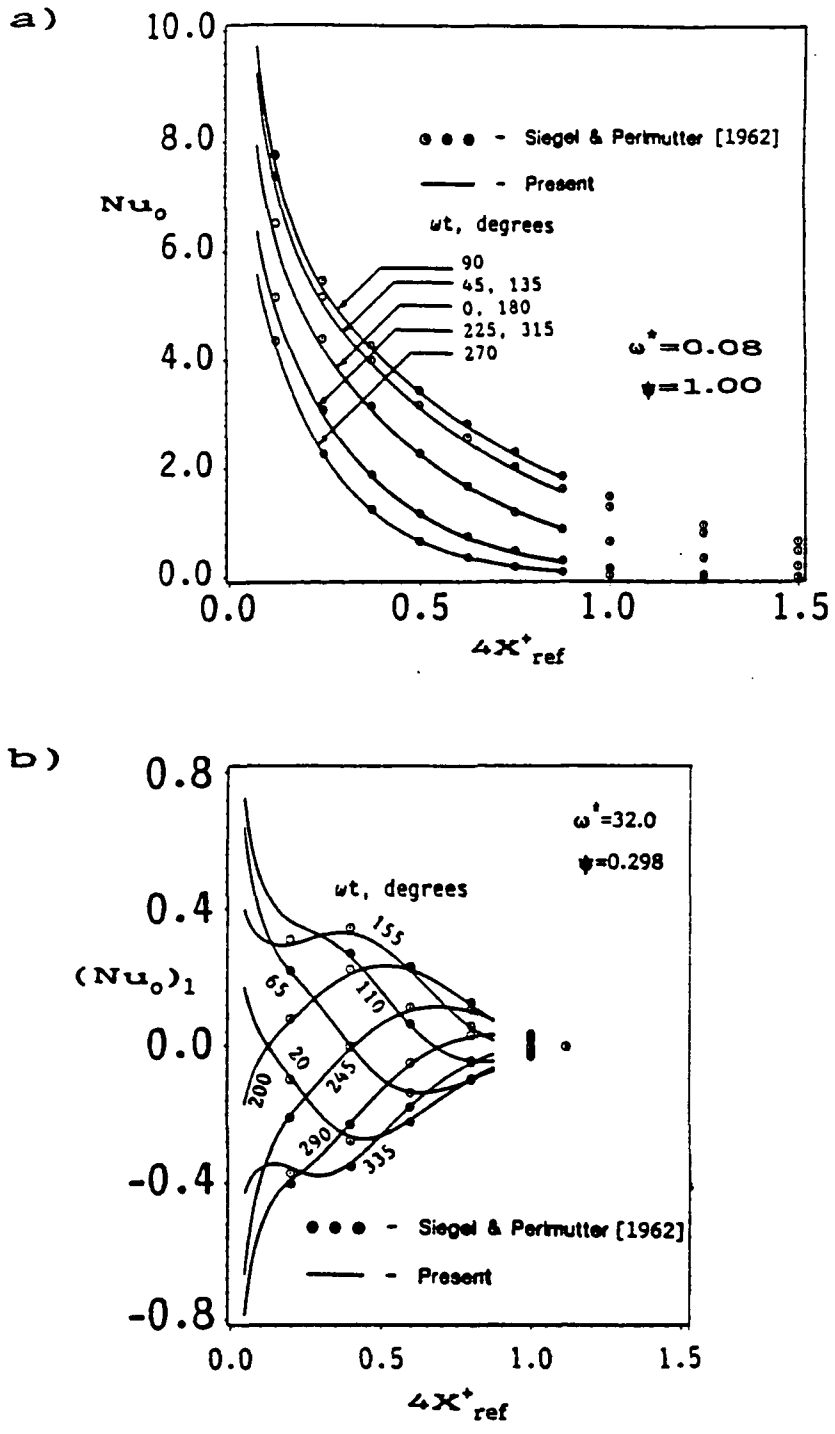

Figure 4.2.3: Nusselt number variation in the channel compared between present work and data from Siegel & Perlmutter [1962] (incompressible with pulsating slug flow approximation, Re_{mean}=2000, Pr=0.72):

a) Instantaneous Nusselt number, ω^*=0.08, ψ=1.00 [PI-1].

b) Fluctuating component of the Nusselt number, ω^*=32.0, ψ=0.298 [PI-3].

4.2.3a); accordingly, the quasi-steady approximation can be applied. As the Valensi number increases the fluctuating Nusselt number takes a complex shape in its variation with x or time. The quasi-steady approximation can only be applied close to the duct inlet.

Pulsating Simultaneously Developing Flows (Variable Fluid Properties):

In this segment, new results will be presented for thermally and hydrodynamically developing flow for incompressible, thermally expandable and compressible fluid assumptions. The effects of variable fluid properties and fluctuating frequencies (Valensi number) on the pulsating flow results are discussed. The following parameters are fixed for the rest of the investigation in this pulsating flow solution section: a) Re_{ref}=2000, b) air is the fluid, and c) ψ=1.0 (50% of the mean velocity value).

Figures 4.2.4a to 4.2.4c show the mass flux variation in the channel at different ωt. Figure 4.2.4a illustrates the results for incompressible flow at any ω^* value. Notice the inlet mass flux is always equivalent to the exit mass flux at any instant of ωt. This behavior is due to the constant density restriction applied by the incompressible fluid assumption; the same conclusion was observed for compressible flow at a low Valensi number (ω^*=0.08). But as the Valensi number increases, the instantaneous mass flux at the two ends of the duct is no longer equal for variable property flows. The viscous damping of the fluid reduces the amplitude of the unsteady mass flux fluctuation downstream (see Figures 4.2.4b and 4.2.4c).

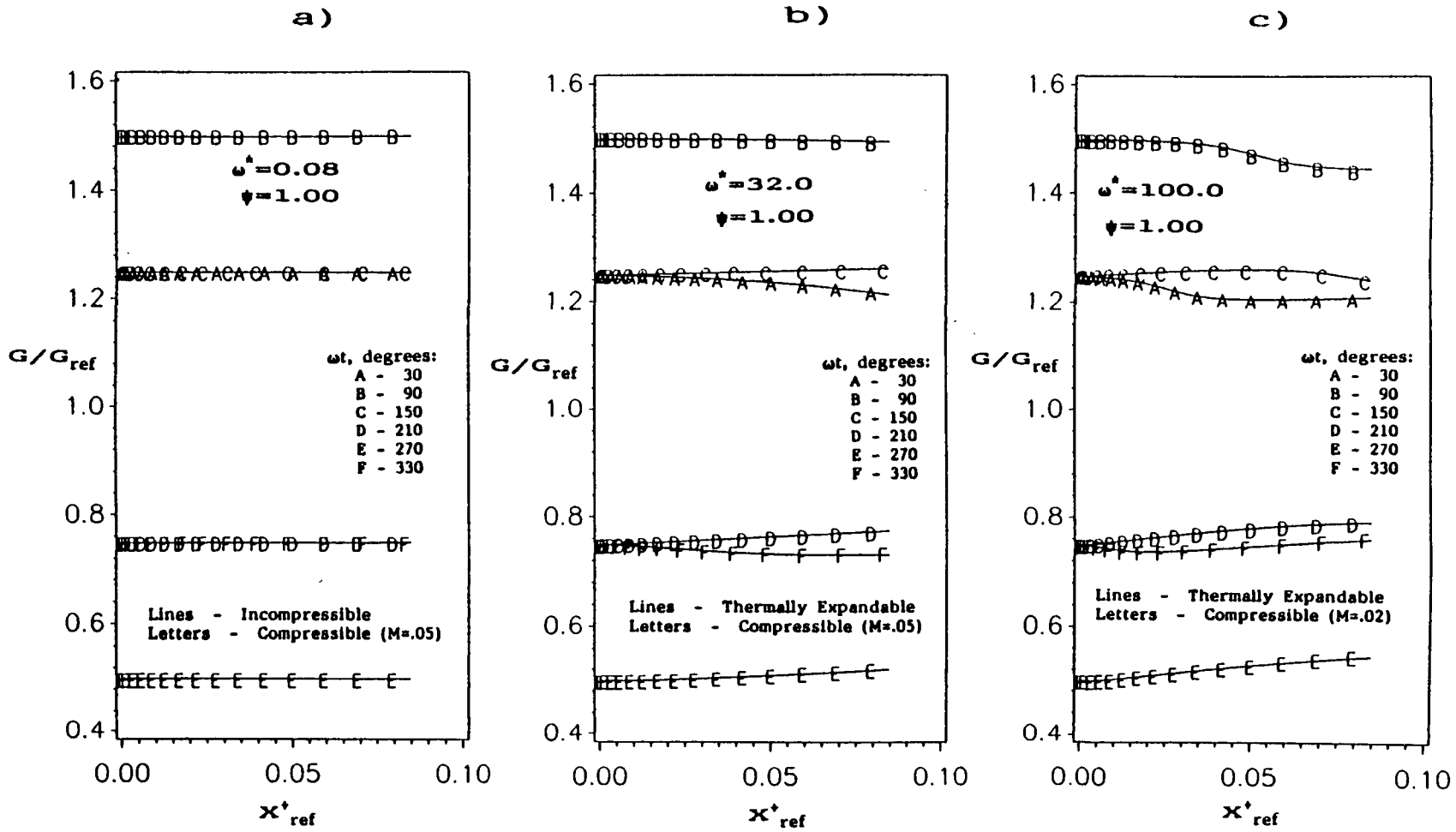

Figure 4.2.4: Mass flux variation in the channel with different fluid property assumptions (incompressible, thermally expandable and compressible), (Re_{mean}=2000, T_w/τ_0=1.2, Pr=.72, ψ=1.00):
a) ω^*=0.08 [PI-5, PC-1].
b) ω^*=32.0 [PT-3, PC-2].
c) ω^*=100.0 [PT-5, PC-3].

Accordingly, Table 4.2.3 presents the Amplitude of the exit mass flux fluctuation for the three ω^* (.08, 32.0 and 100.0) examined with the inlet fluctuation amplitude set equal to 1.0 . The following pulsating flow observations were gathered from Figures 4.2.4a to 4.2.4c and Table 4.2.3:

a) For incompressible flows, the instantaneous mass flux is identical at any axial location which means any changes or disturbance in the inlet mass flux is immediately transferred throughout the channel. This is true at any Valensi number for pulsating incompressible flow.

b) For thermally expandable and compressible flows, the fluctuating mass flux signal at the inlet is delayed downstream by the fluid density changes. Also the amplitude of mass flux fluctuation decreases with respect to the axial distance caused by the fluid viscous damping. These results suggest that if the channel was sufficiently long, the damping effect of the fluid will eventually eliminate the fluctuating component of the pulsating flow; hence, the flow will become steady-state downstream.

c) Results in Table 4.2.3 suggest the higher the Valensi number (dimensionless frequency) of the pulsating flow, the faster the fluctuating component diminishes. This phenomenon is similar to the behavior of sound wave, where lower frequency waves can travel further in distance than higher frequency waves at the same amplitude of fluctuation.

Table 4.2.3: Amplitude of the fluctuating mass flux at the channel's exit for different ω^* (thermally expandable pulsating flow, L/H=70.0, Re_{mean}=2000, Pr=.72, T_w/T_0=1.2, ψ=1.00) [PT-1, PT-3, PT-5].

ω^*	$(G_{exit}/G_{ref})_{max}$	$(G_{exit}/G_{ref})_{min}$	Amplitude of the Exit Mass Flux Fluctuation
.08	1.500	0.500	1.000
32.0	1.489	0.527	0.962
100.0	1.439	0.555	0.884

Table 4.2.4: Comparison between the time-averaged pulsating friction with the steady friction at different wall/inlet temperature ratios (Re_{mean}=2000, Pr=.72) [PI-5 to PI-7, PT-1 to PT-6].

T_w/T_0	X_{ref}^+	Steady Local F*	Time-Averaged Local F*			Diff. from the Steady F* (%)		
			ω^*=.08	ω^*=32	ω^*=100	ω^*=.08	ω^*=32	ω^*=100
1.0 (Inc.)	.005	2.619	2.589	2.590	2.599	-1.1	-1.1	-0.8
	.010	1.914	1.880	1.891	1.898	-1.3	-1.2	-0.8
	.020	1.449	1.434	1.433	1.424	-1.0	-1.1	-1.7
	.040	1.149	1.152	1.142	1.098	0.3	-0.6	-4.4
	.080	1.019	1.031	1.012	0.936	1.2	-0.7	-8.2
1.2 (T.E.)	.005	2.785	2.753	2.753	2.754	-1.1	-1.1	-1.1
	.010	2.037	2.012	2.011	1.996	-1.2	-1.3	-2.0
	.020	1.543	1.521	1.515	1.470	-1.4	-1.8	-4.7
	.040	1.225	1.208	1.191	1.110	-1.4	-2.8	-9.4
	.080	1.078	1.064	1.037	0.962	-1.3	-3.8	-10.8
1.4 (T.E.)	.005	2.931	2.894	2.893	2.888	-1.3	-1.3	-1.5
	.010	2.143	2.116	2.112	2.083	-1.3	-1.4	-2.8
	.020	1.624	1.598	1.587	1.518	-1.6	-2.3	-6.5
	.040	1.291	1.260	1.238	1.137	-2.4	-4.1	-11.9
	.080	1.123	1.095	1.085	0.992	-2.5	-5.2	-11.7

Note: $F^* = f_{app} * Re_x / 24$
Inc. – Incompressible
T.E. – Thermally Expandable

Figures 4.2.5a to 4.2.5c present the predicted local time-averaged apparent friction versus the normalized axial distance with ω^+=0.08 (Figure 4.2.5a), 32.0 (Figure 4.2.5b) and 100.0 (Figure 4.2.5c). The pulsating results are plotted with the steady results as reference. In addition, Table 4.2.4 shows the numerical comparison between the steady state and the local time-averaged apparent friction under the incompressible and thermally expandable models. For ω^+=0.08 and 32.0, the difference between the steady state friction and the local time-averaged friction is within 5% for the three T_w/τ_0 (1.0, 1.2 and 1.4) ratios. The results lead to the conclusion that these low frequency flows are still close to quasi-steady. However, at a Valensi number equal to 100.0, the difference between the steady state friction and the local time-averaged friction increases to about 12% downstream. Only the near entrance region can be modeled by the quasi-steady assumption.

Comparison of the local time-averaged friction between thermally expandable and compressible models is presented in Figures 4.2.6a to 4.2.6c. At the lower frequencies (ω^+=0.08 and 32.0), the difference is minimal (see Table 4.2.5), but at the higher frequency (ω^+=100.0) the difference between the two fluid models reached as high as 7.6% downstream,

Figures 4.2.7a to 4.2.7c show the predicted normalized mean fluid temperature versus time at different axial locations and ω^+=0.08 (Figure 4.2.7a), 32.0 (Figure 4.2.7b), 100.0 (Figure 4.2.7c). As shown in the figures, the temperature fluctuation increases as the fluid moves downstream, while the amplitude of these temperature fluctuations decreases as the Valensi

a)

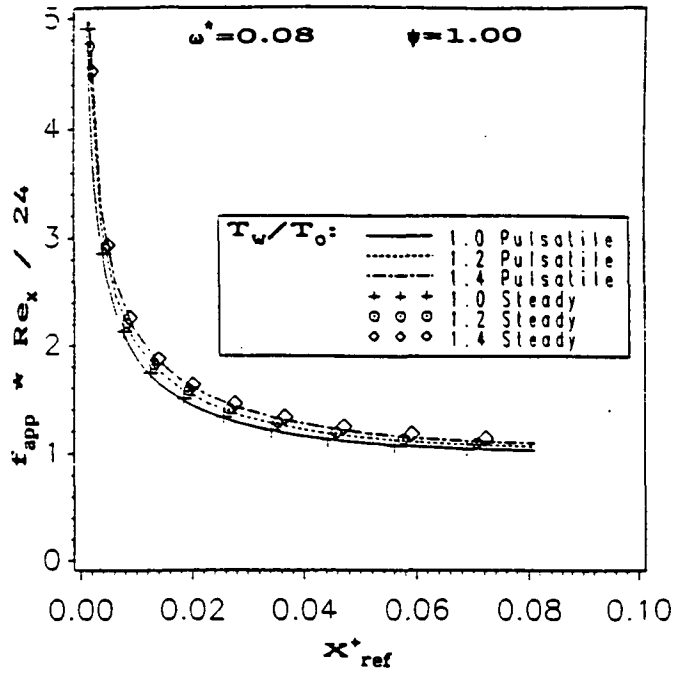

b)

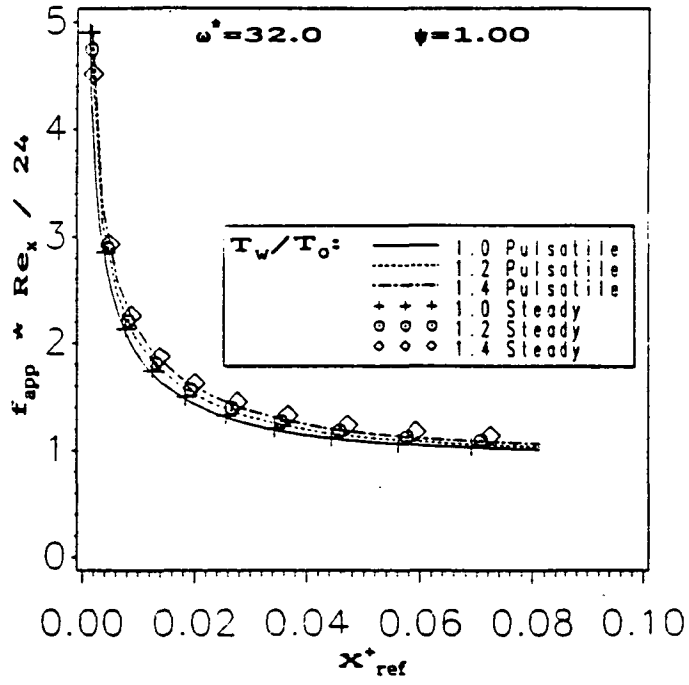

Figure 4.2.5: Time-averaged local apparent friction in the channel at different wall/inlet temperature ratios: T_w/T_0=1.0 (incompressible), 1.2 and 1.4 (thermally expandable); (Re_{mean_t}=2000, Pr=0.72, ψ=1.00):
a) ω^*=0.08 [PI-5, PT-1, PT-2].
b) ω^*=32.0 [PI-6, PT-3, PT-4].

c)

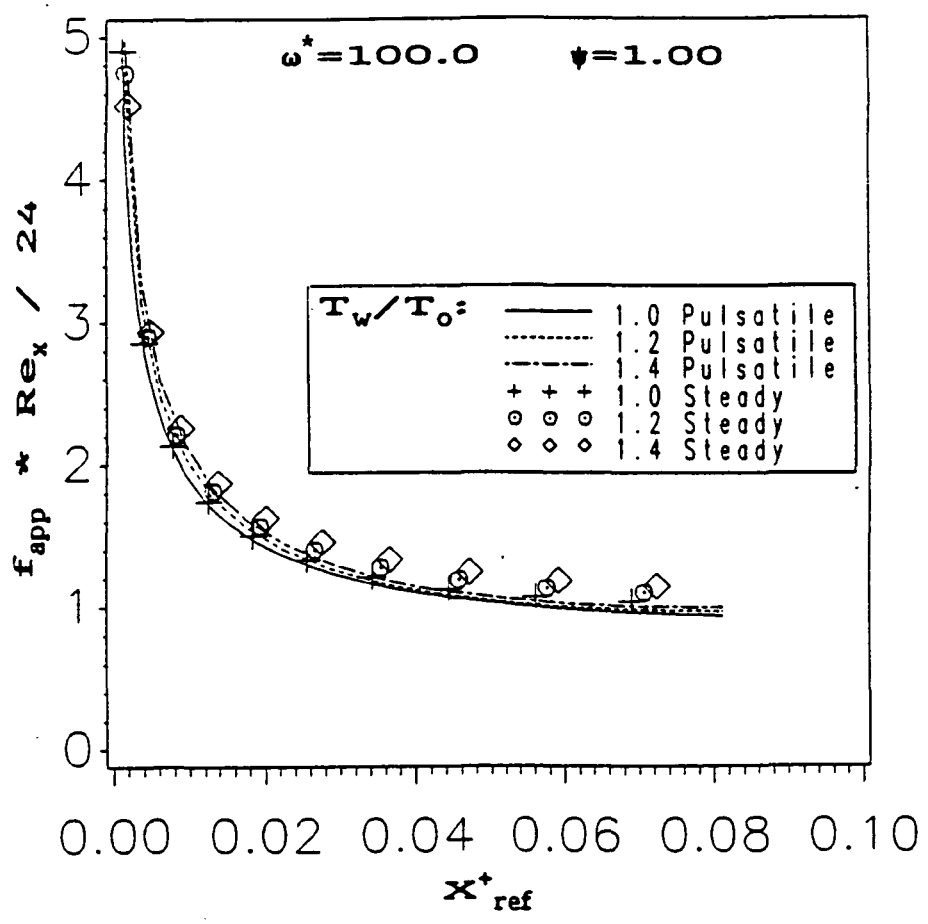

Figure 4.2.5 (cont.):
c) ω^*=100.0 [PI-7, PT-5, PT-6].

a)

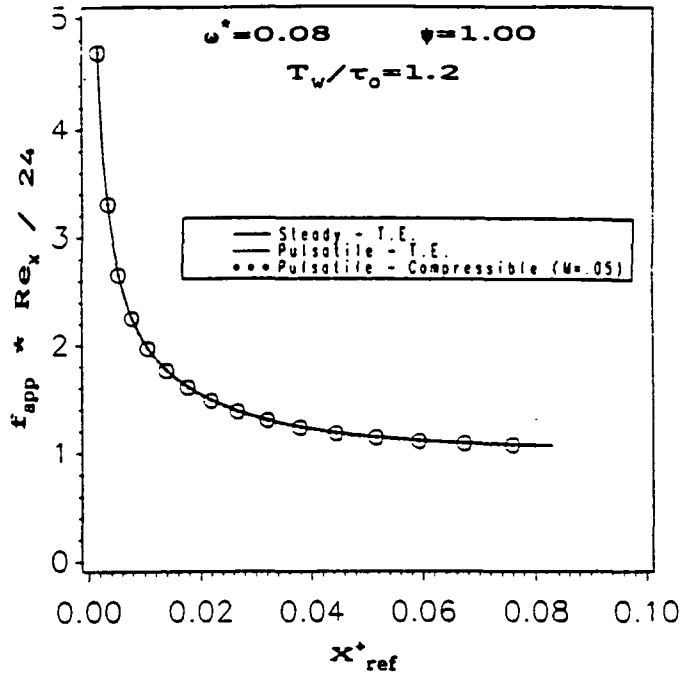

b)

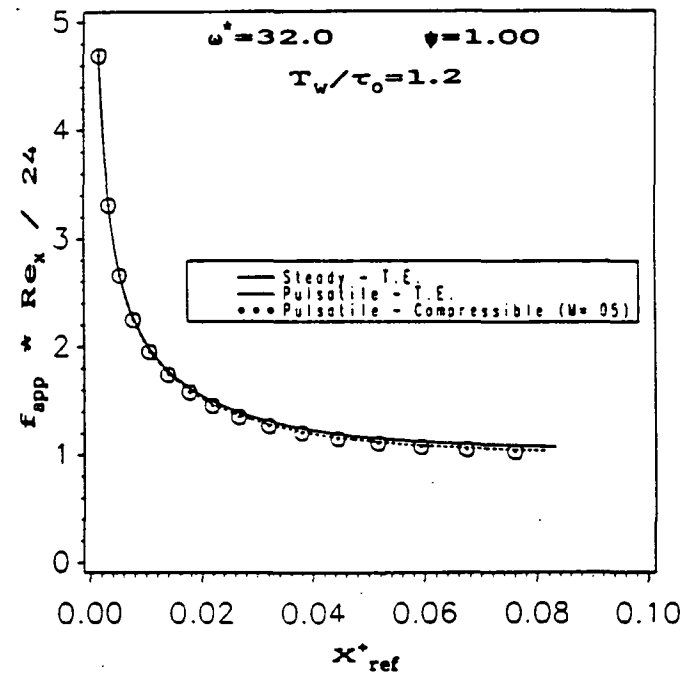

Figure 4.2.6: Comparison of the time-averaged local apparent friction in the channel between thermally expandable and compressible predictions (Re_{mean}=2000, air, T_w/τ_0=1.2, ψ=1.00):
a) ω^+=0.08 [PT-1, PC-1].
b) ω^+=32.0 [PT-3, PC-2].

c)

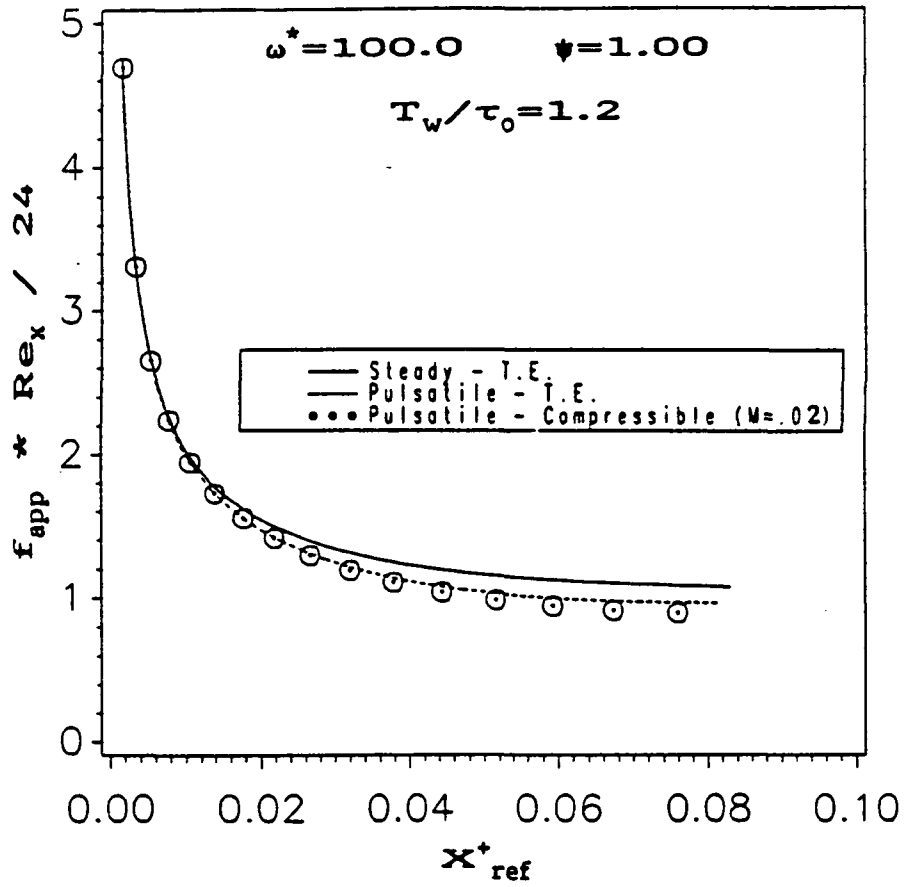

Figure 4.2.6 (cont.):
c) ω^*=100.0 [PT-5, PC-3].

Table 4.2.5: Comparison of the time-averaged pulsating friction between predictions from thermally expandable and compressible flows (Re_{mean}=2000, air) [PT-1, PT-3, PT-5, PC-1 to PC-3].

ω^*	T_w/T_e	Mach no.	X_{ref}^+	Time-Averaged Local F^*		Diff. between Comp. and T.E. (%)
				T.E.	Comp.	
.08	1.2	.05	.005	2.753	2.756	0.1
			.010	2.012	2.015	0.1
			.020	1.523	1.526	0.2
			.040	1.210	1.212	0.2
			.080	1.066	1.068	0.2
32	1.2	.05	.005	2.753	2.758	0.2
			.010	2.011	1.999	−0.6
			.020	1.515	1.496	−1.3
			.040	1.191	1.178	−1.1
			.080	1.037	1.015	−2.1
100	1.2	.02	.005	2.754	2.755	0.0
			.010	1.996	1.996	0.0
			.020	1.470	1.462	−0.5
			.040	1.110	1.077	−3.0
			.080	0.962	0.889	−7.6

Note: $F^* = f_{app} * Re_\tau / 24$
T.E. – Thermally Expandable
Comp. – Compressible

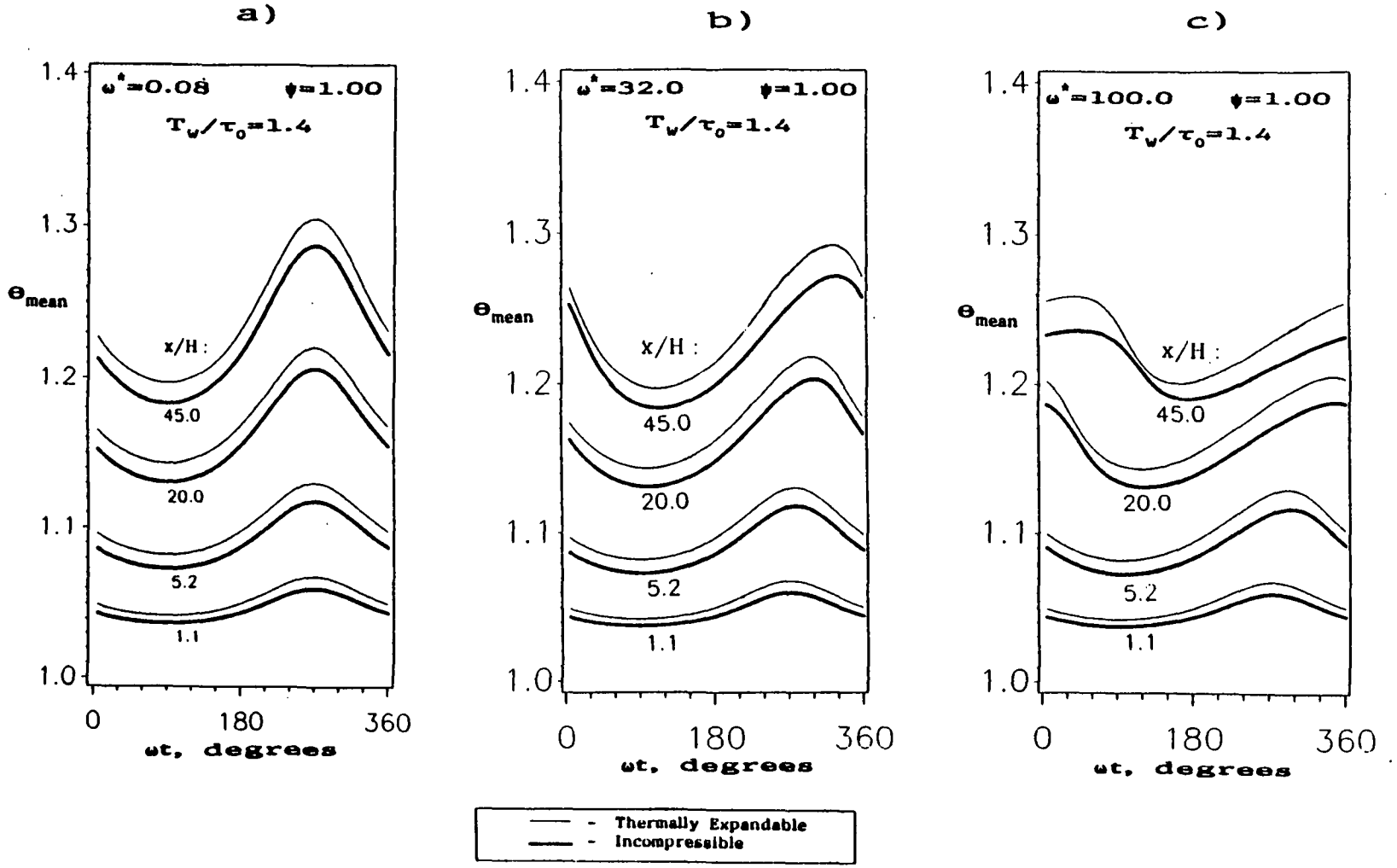

Figure 4.2.7: Mean fluid temperature versus time for simultaneously developing, pulsating flow. Predictions from incompressible and thermally expandable fluid properties are compared (T_w/T_{0_i}=1.4, Re_{mean}=2000, Pr=0.72, ψ=1.00):
a) ω^*=0.08 [PI-5, PT-2].
b) ω^*=32.0 [PI-6, PT-4].
c) ω^*=100.0 [PI-7, PT-6].

number increases. Moreover, for the same first order harmonic flow field, the temperature field contains only low order harmonics at low Valensi numbers (see Figure 4.2.7a); while at higher Valensi numbers (see Figures 4.2.7b and 4.2.7c), distortions of the temperature fluctuations suggest higher order harmonics are present. The trend of the temperature field is similar for both incompressible and thermally expandable models, except the incompressible model under-states the temperature. Table 4.2.6 lists the numerical comparison of Figures 4.2.7a to 4.2.7c.

Figure 4.2.8 shows similar plots of mean temperature fluctuation as presented in Figure 4.2.7 except the predictions are from thermally expandable and compressible fluid models. The trend of the temperature field is identical for both models with minimal difference.

The effect of the Valensi number towards the heat transfer of the pulsating flow is examined and presented in Figures 4.2.9a (ω^*=0.08), 4.2.9b (ω^*=0.08) and 4.2.9c (ω^*=0.08). The figures plot the local time-averaged Nusselt number together with the corresponding steady Nusselt number results at different wall/inlet temperature ratios. The comparison of the time-averaged results versus the steady Nusselt number results shows increased differences as the Valensi number increases, however, even at the high ω^*=100.0, the maximum difference downstream is only 1.2% (see Table 4.2.7). Thus, the steady heat transfer predictions are good estimations of the time-averaged pulsating heat transfer results even at high Valensi numbers.

Illustrated in Figures 4.2.10a to 4.2.10c are heat transfer solutions

Table 4.2.6: Periodic location and amplitude of the maxima cross-sectional mean fluid temperature [PI-5 to PI-7, PT-2, PT-4, PT-6].

ω^*	T_e/T_o	x/H	Maximum θ_{max}		Velocity Phase Angle, ωt at the Maximum θ_{max} (degrees)	
			Incomp.	T.E.	Incomp.	T.E.
.08	1.4	1.1	1.060	1.068	270	270
		5.2	1.118	1.130	270	270
		20.0	1.206	1.221	270	270
		45.0	1.287	1.305	270	270
		60.0	1.318	1.336	270	270
32	1.4	1.1	1.060	1.068	270	270
		5.2	1.118	1.130	280	275
		20.0	1.203	1.218	300	295
		45.0	1.271	1.293	330	320
		60.0	1.296	1.319	340	335
100	1.4	1.1	1.060	1.068	275	275
		5.2	1.117	1.130	295	295
		20.0	1.188	1.208	350	345
		45.0	1.236	1.259	45	40
		60.0	1.254	1.278	75	70

Notes: Incomp. - Incompressible
T.E. - Thermally Expandable

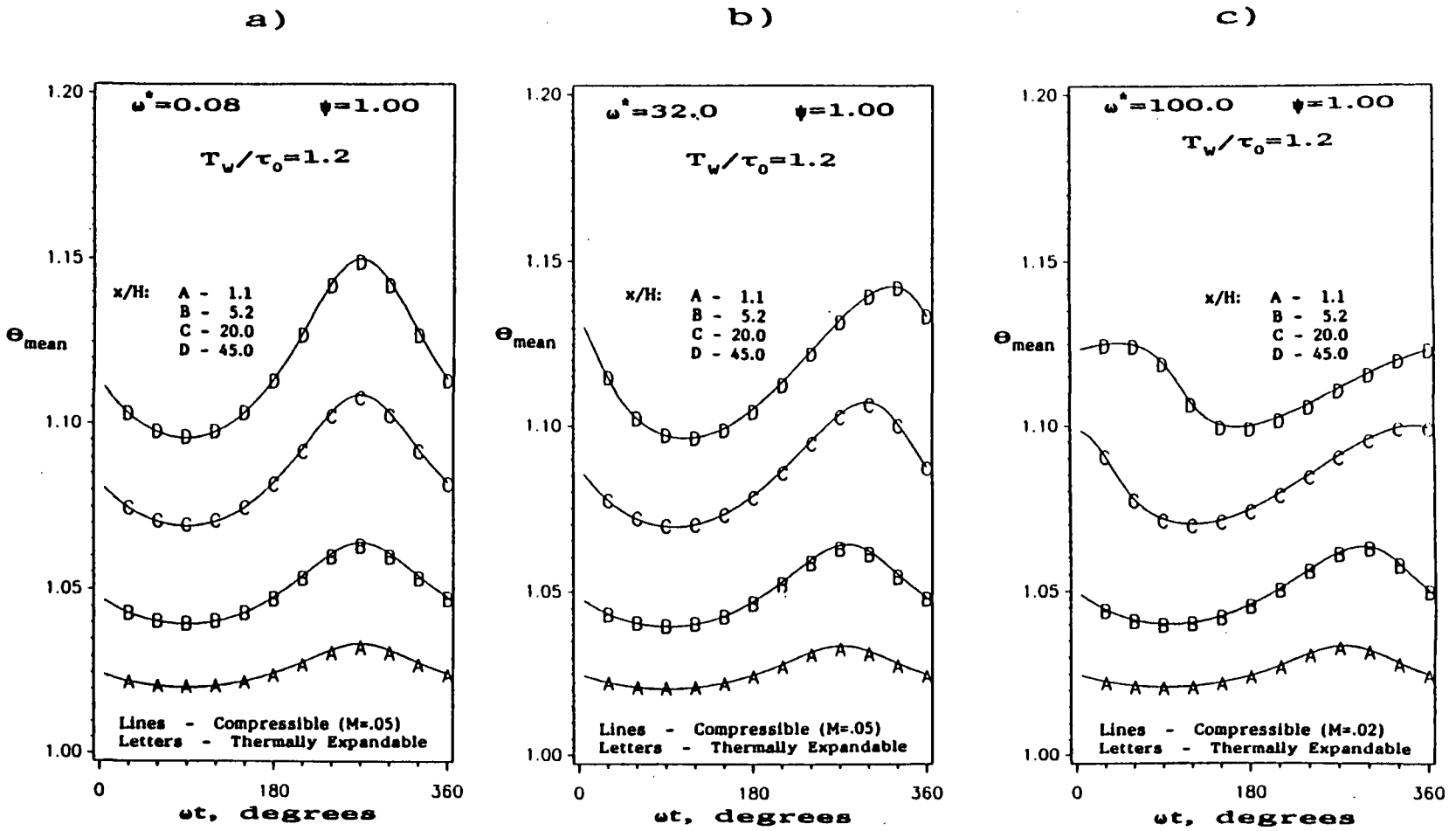

Figure 4.2.8: Mean fluid temperature versus time for simultaneously developing, pulsating flow. Predictions from thermally expandable and compressible fluid properties are compared (T_w/T_{0_i}=1.2, Re_{mean}=2000, air, ψ=1.00):

a) ω^*=0.08 [PT-1, PC-1].

b) ω^*=32.0 [PT-3, PC-2].

c) ω^*=100.0 [PT-5, PC-3].

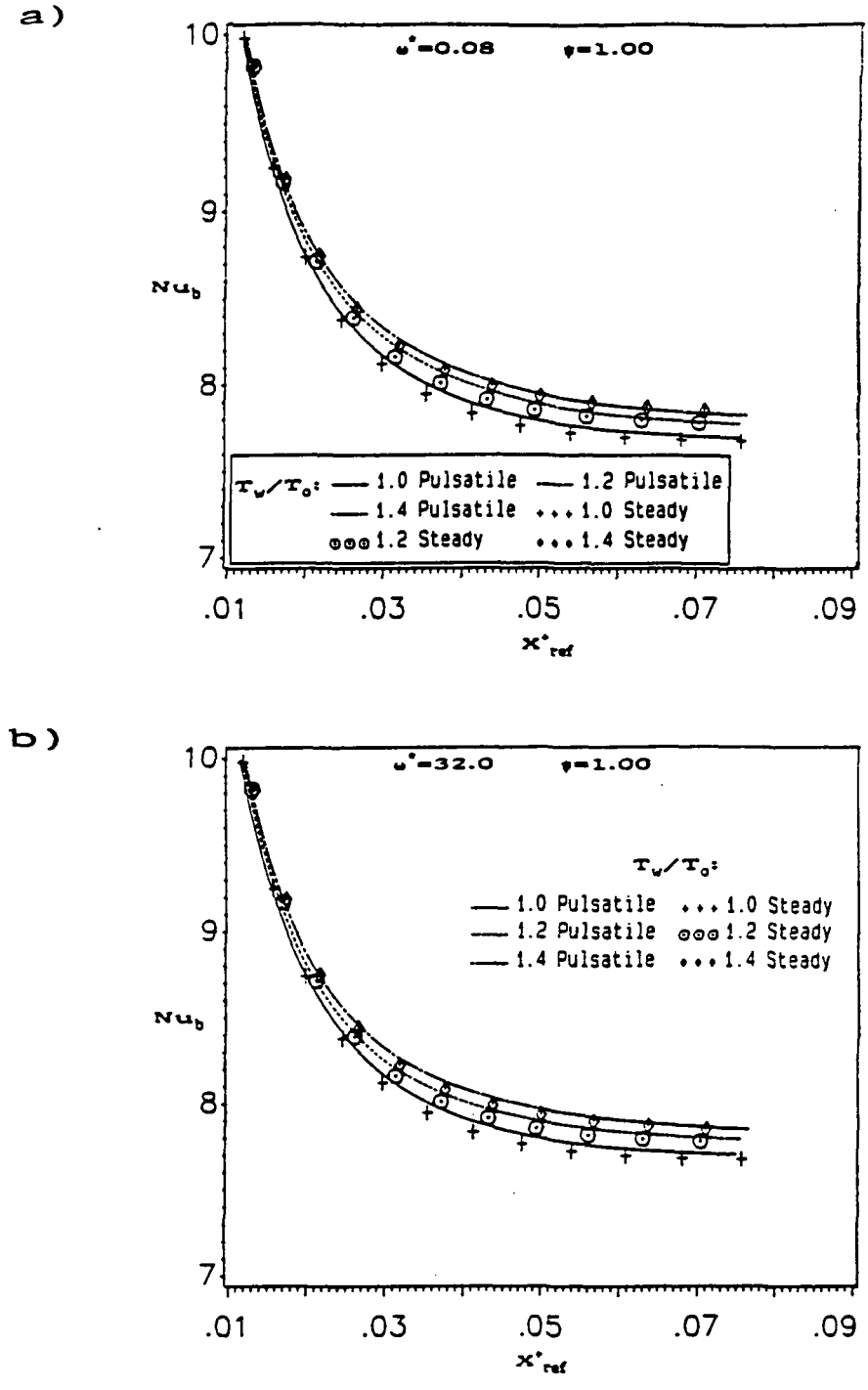

Figure 4.2.9: Time-averaged Nusselt number in the channel at different wall/inlet temperature ratios: T_w/T_0=1.0 (incompressible), 1.2 and 1.4 (thermally expandable); (Re_{mean}=2000, Pr=0.72, ψ=1.00):
a) ω^*=0.08 [PI-5, PT-1, PT-2].
b) ω^*=32.0 [PI-6, PT-3, PT-4].

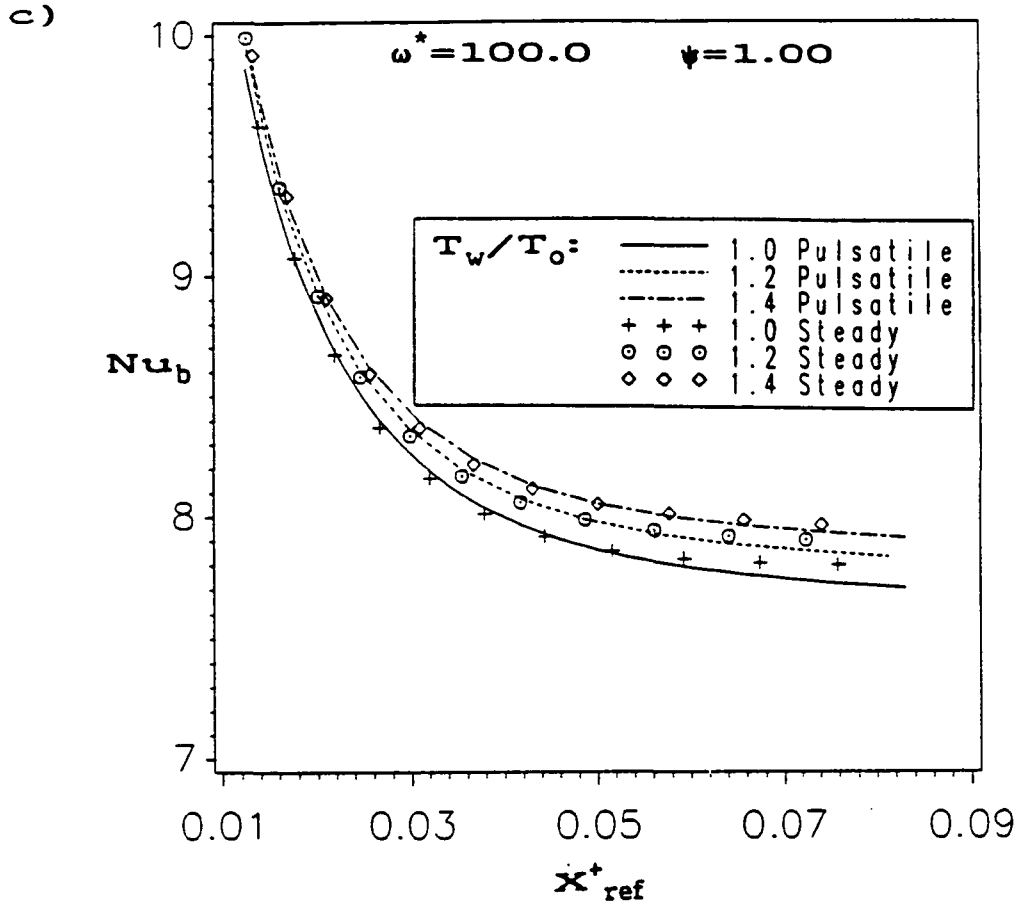

Figure 4.2.9 (cont.):
c) ω^*=100.0 [PI-7, PT-5, PT-6].

Table 4.2.7: Comparison between the time-averaged pulsating Nusselt number with the steady Nusselt number at different wall/inlet temperature ratios (Re_{mean}=2000, Pr=.72) [PI-5 to PI-7, PT-1 to PT-6].

T_w/T_o	X_{ref}^+	Steady Local Nu_x	Time-Averaged Local Nu_x			Diff. from the Steady Nu_x		
			ω^+=.08	ω^+=32	ω^+=100	ω^+=.08	ω^+=32	ω^+=100
1.0 (Inc.)	.02	8.82	8.83	8.82	8.84	.11%	0.0%	.23%
	.04	7.97	8.02	8.02	7.99	.63%	.63%	.25%
	.06	7.82	7.86	7.86	7.79	.51%	.51%	-.38%
	.08	7.80	7.81	7.82	7.72	.13%	.26%	-1.2%
1.2 (T.E.)	.02	8.92	8.91	8.91	8.92	-.11%	-.11%	0.0%
	.04	8.08	8.11	8.11	8.09	.37%	.37%	.12%
	.06	7.93	7.94	7.95	7.91	.13%	.25%	-.25%
	.08	7.89	7.89	7.90	7.84	0.0%	.13%	-.63%
1.4 (T.E.)	.02	8.98	8.97	8.97	8.98	-.11%	-.11%	0.0%
	.04	8.15	8.17	8.17	8.17	.25%	.25%	.25%
	.06	8.00	7.99	8.00	7.99	-.12%	0.0%	-.12%
	.08	7.95	7.94	7.95	7.92	-.13%	0.0%	-.38%

Note: Inc. - Incompressible
T.E. - Thermally Expandable

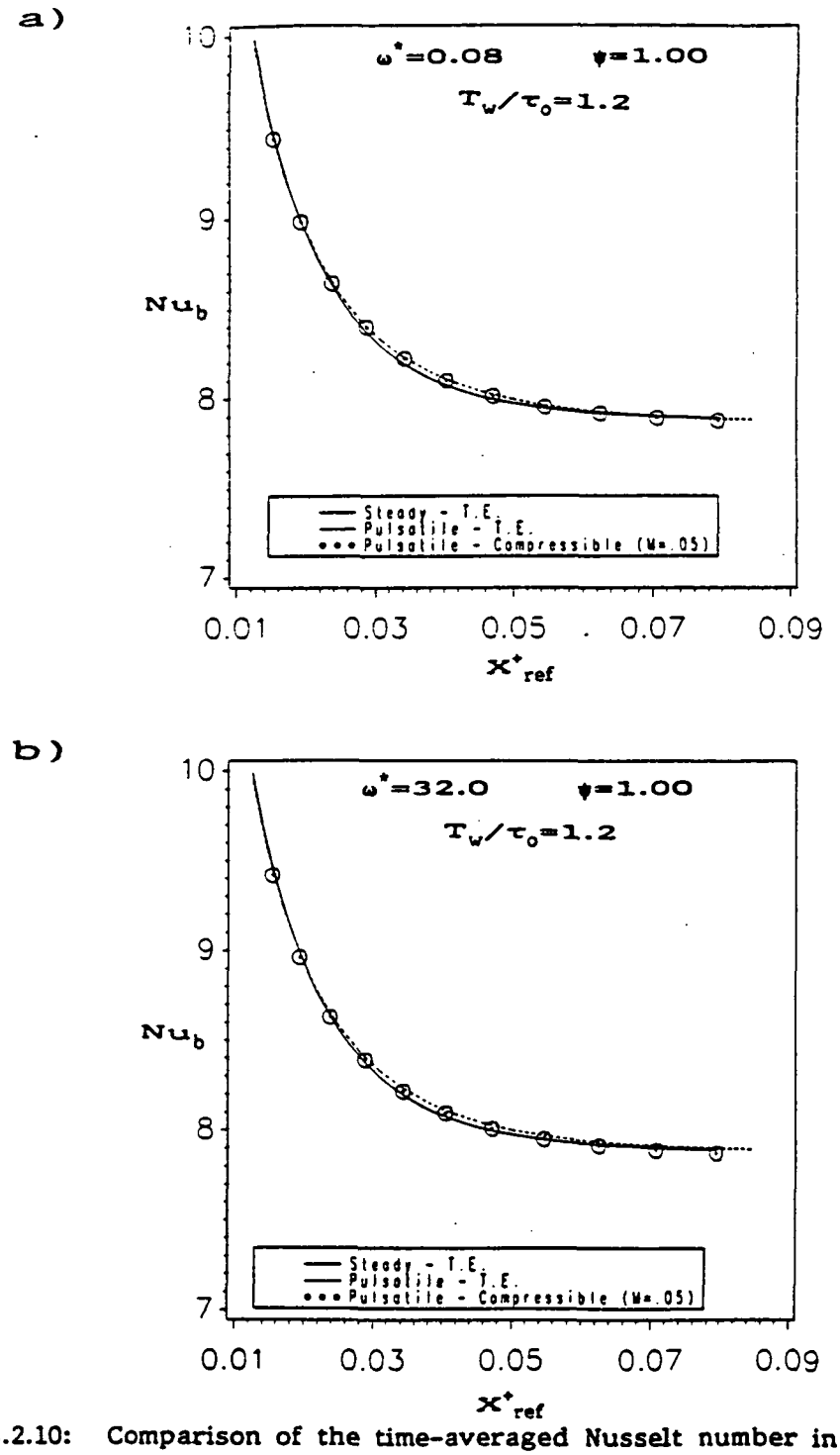

Figure 4.2.10: Comparison of the time-averaged Nusselt number in the channel between thermally expandable and compressible predictions (Re_{bean}=2000, air, T_w/τ_0=1.2, ψ=1.00):
a) ω^+=0.08 [PT-1, PC-1].
b) ω^+=32.0 [PT-3, PC-2].

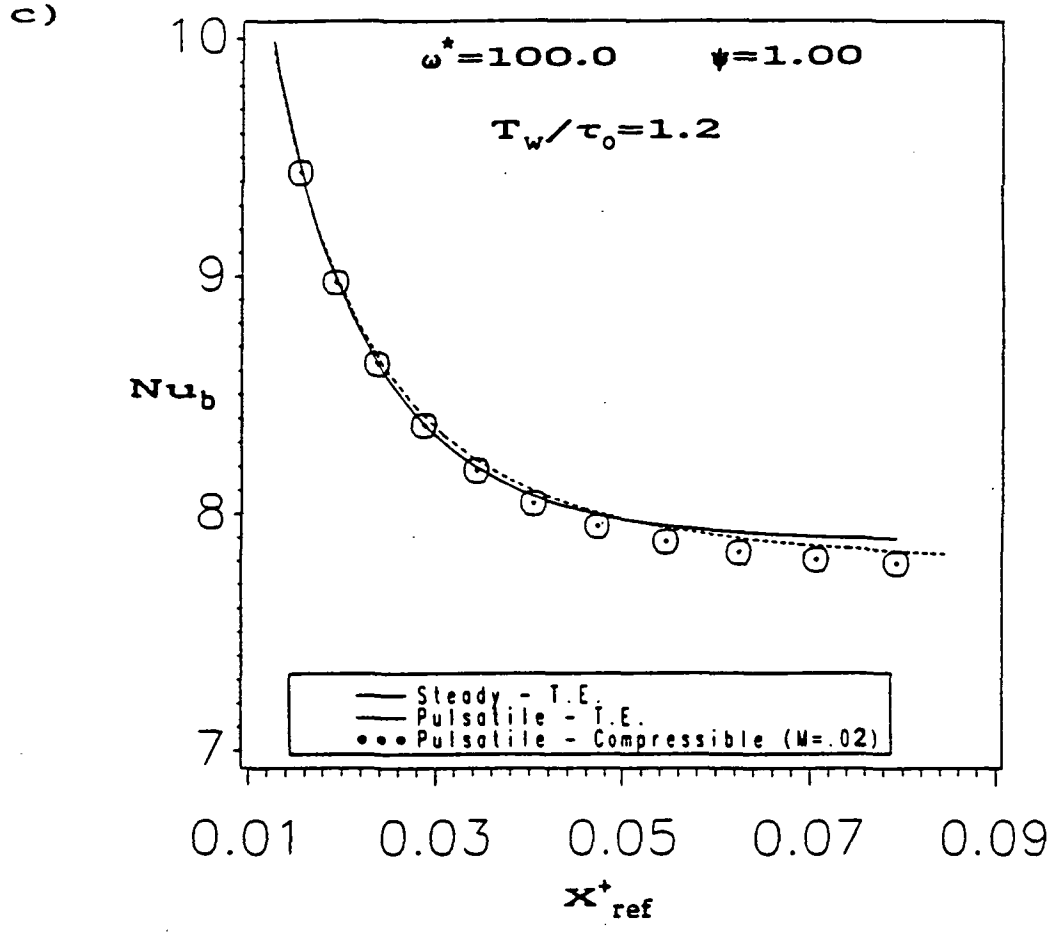

Figure 4.2.10 (cont.):
c) ω^*=100.0 [PT-5, PC-3].

Table 4.2.8: Comparison of the time-averaged pulsating Nusselt number between predictions from thermally expandable and compressible flows (Re_{mean}=2000, air) [PT-1, PT-3, PT-5, PC-1 to PC-3].

ω^*	T_w/T_o	Mach no.	X_{ref}^+	Time-Averaged Local Nu,		Diff. between Comp. and T.E. (%)
				T.E.	Comp.	
.08	1.2	.05	.010	10.59	10.59	0.00
			.020	8.912	8.907	0.06
			.040	8.107	8.099	0.10
			.080	7.889	7.878	0.14
32	1.2	.05	.010	10.59	10.55	0.04
			.020	8.911	8.886	0.28
			.040	8.109	8.091	0.22
			.080	7.901	7.871	0.38
100	1.2	.02	.010	10.60	10.58	0.19
			.020	8.922	8.893	0.33
			.040	8.094	8.042	0.65
			.080	7.839	7.786	0.68

Notes: T.E. – Thermally Expandable
Comp. – Compressible

of the pulsating flow influenced by the effect of fluid compressibility under different pulsating frequencies. As listed in Table 4.2.8, similar Nusselt number predictions were found by the thermally expandable model and the compressible model (Mach number of .02 and .05).

A couple of major observations are identified from this pulsating flow study. The fluid compressibility has a direct effect on the friction factor and there is a secondary effect on the heat transfer coefficient (see Table 4.2.5 and 4.2.8). At a range of the Valensi number, the steady flow model provides good estimations for the time-averaged pulsating Nusselt number; whereas, for the time-averaged pulsating friction factor, close estimations by the steady flow model is limited to pulsating flow at the low Valensi number.

Oscillating Flows

The examination of the oscillating flow is divided into two segments. The first segment validates the code by comparing results with data from the existing literature on the incompressible model, then it leads into the investigation of compressibility effects on the friction and heat transfer coefficients. The second segment predicts friction and heat transfer results under the NASA Space Power Research Engine (SPRE) boundary conditions by the incompressible and compressible models. The comparison

of the two models will be presented and discussed.

Oscillating Flow (ω^+=32.0 and Re_{max}=2000):

Kurzweg [1985] developed an analytical equation to calculate the velocity profile existing in the central channel for incompressible, laminar, oscillating flow conditions. A validation incompressible run was made at ω^+=32.0 and Re_{max}=2000. The agreements between the present velocity profile and predictions from Kurzweg are excellent, as shown in Figure 4.3.1. The velocity profile pattern is symmetrical around the zero velocity which signifies that the flow is fully-developed.

Figure 4.3.2 illustrates the pressure in the channel at various ωt. Besides the entry effect at both ends of the channel, the pressure fluctuation is symmetrical around the normalized pressure value of zero; the same qualitative finding was observed by Wolf [****] in his oscillating flow study for tubes.

1990

With similarity to the pulsating flow, a lead phase angle for the pressure gradient over the velocity exists. Table 4.3.1 reveals the present lead phase angle as 68 degrees for the ω^+=32.0 and Re_{max}=2000; this is compared to the 66 degrees found by Kurzweg [1985] at the same conditions. Table 4.3.1 also shows the lead phase angle results for the variable fluid property models. The graphical presentation of the pressure gradient variation for one oscillating cycle is illustrated in Figure 4.3.3, and sine wave pressure gradient curves were obtained.

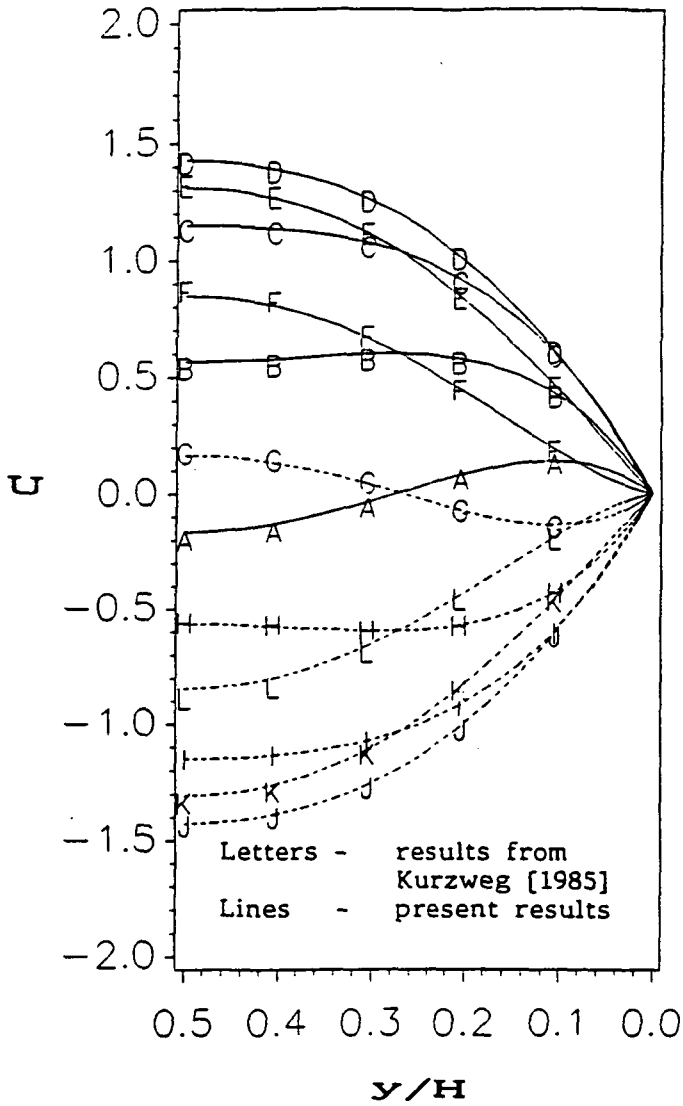

ωt, degrees:		
A A - 0.0	B B - 30.0	C C - 60.0
D D - 90.0	E E - 120.0	F F - 150.0
G G - 180.0	H H - 210.0	I I - 240.0
J J - 270.0	K K - 300.0	L L - 330.0

Figure 4.3.1: **Cross-sectional velocity profiles compared between present work with data from Kurzweg [1985] (fully-developed, incompressible oscillating flow, Re_{ω}=2000, ω^{+}=32.0) [OS-1].**

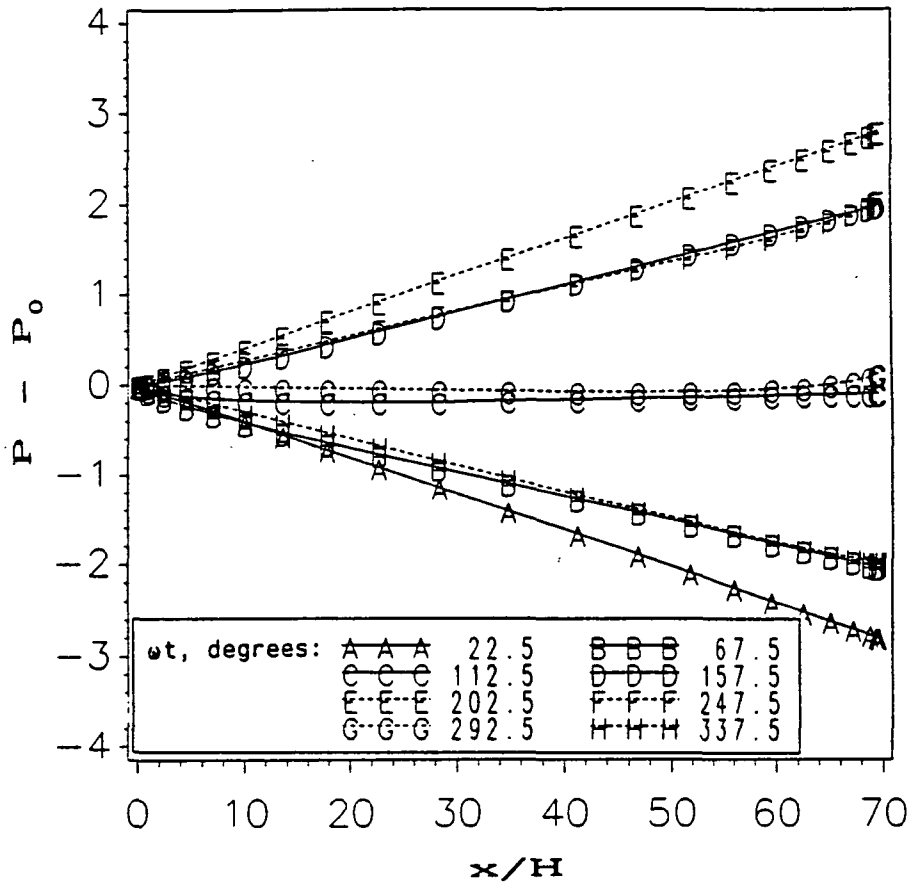

Figure 4.3.2: Center-line pressure in the channel at different ωt values (incompressible oscillating flow, Re_{max}=2000, ω^+=32.0) [OS-1].

Table 4.3.1: Comparison between present work and data from Kurzweg [1985] on the phase angle difference between cross-sectional average velocity and axial pressure gradient (fully-developed oscillating flow, Re_{max}=2000, ω^{+}=32.0) [OS-1 to OS-3].

ω^{+}	Phase Angle Difference (degrees)			
	Kurzweg [1985]	Present		
	Incomp.	Incomp.	T.E.	Comp.
32.0	66.	68.	65.	66.

Notes:

Incomp. – Incompressible
T.E. – Thermally Expandable
Comp. – Compressible (M=.02)

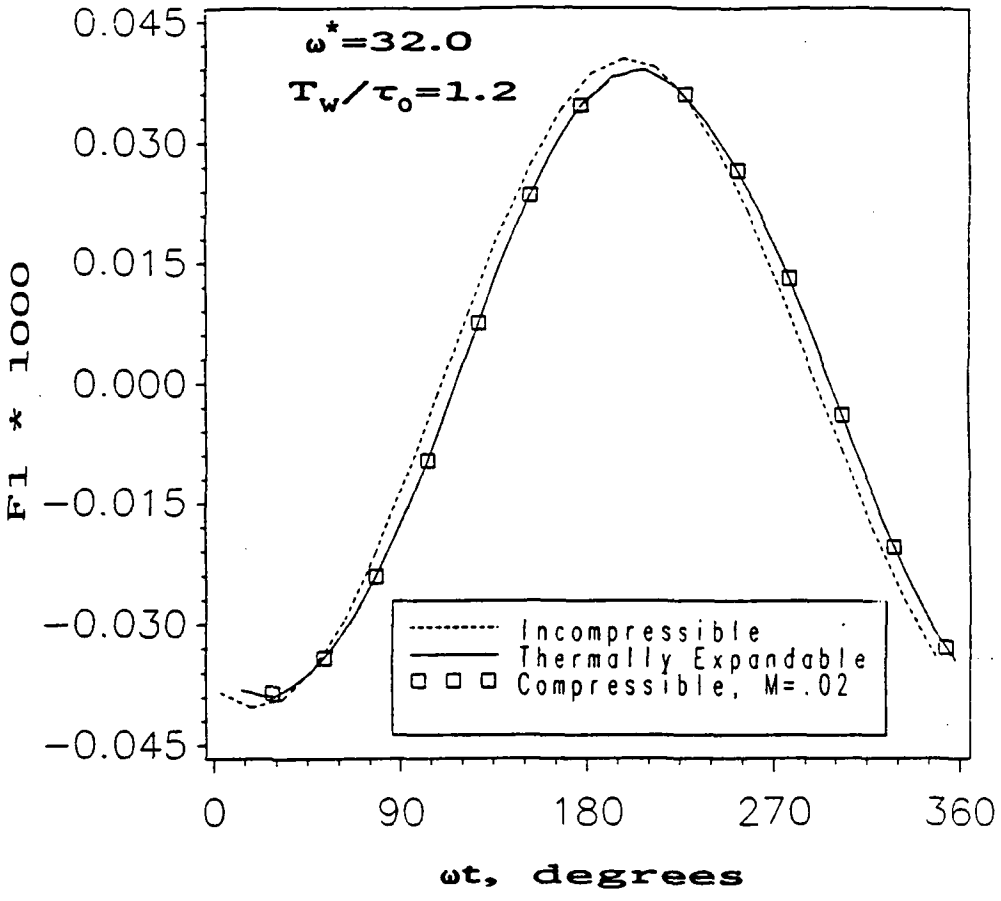

Figure 4.3.3: Oscillating cross-sectional average pressure gradient at the fully-developed region (Re_{max}=2000, ω^*=32.0) [OS-1, OS-2, OS-3].

The examination of the mass flux indicated similar results as found in the pulsating flow analysis. For the incompressible model, the instantaneous mass flux is constant throughout the channel, (see Figure 4.3.4a), while the compressible model indicated a delay of the input mass flux signal caused by the fluid density variation. Notice also that the existence of a mass wave front produced by the acceleration portions of the cycle oscillates through the channel (see Figure 4.3.4b). This wave front identifies the location of high density compression at any instantaneous ωt caused by the variable flow speed.

The next parameter examined is the time-averaged apparent friction in the channel. Unlike the pulsating flow where the time-averaged value is the average value of a complete fluctuation cycle, the time-averaged value for oscillating flow is defined as the average value of the forward half of the cycle. As for the reverse half of the cycle, the time-averaged values are mirror images across the central channel of the forward half results. Figure 4.3.5 shows the time-averaged friction comparison between the different fluid property models plotted with the steady incompressible results as reference. Notice the close agreement between the steady incompressible results with the time-averaged oscillating friction predictions. This suggests that the oscillating flow is close to being quasi-steady. Table 4.3.2a lists the numerical friction values of Figure 4.3.5, and substantial friction difference of about 50% is observed between the incompressible results and the thermally expandable results. The friction comparison between thermally expandable and compressible (M=.02)

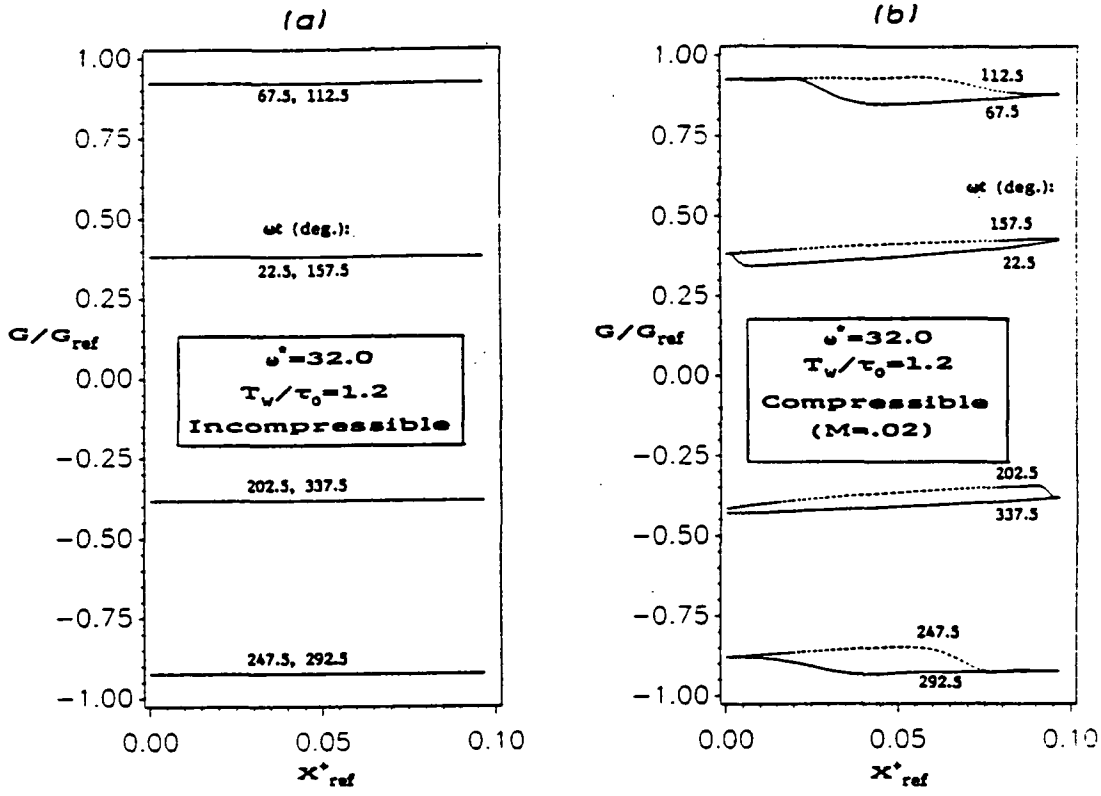

Figure 4.3.4: Mass flux variation in the channel at ω^+=32.0 and Re_{MAX}=2000:
a) incompressible [OS-1].
b) compressible, M=.02 [OS-3].

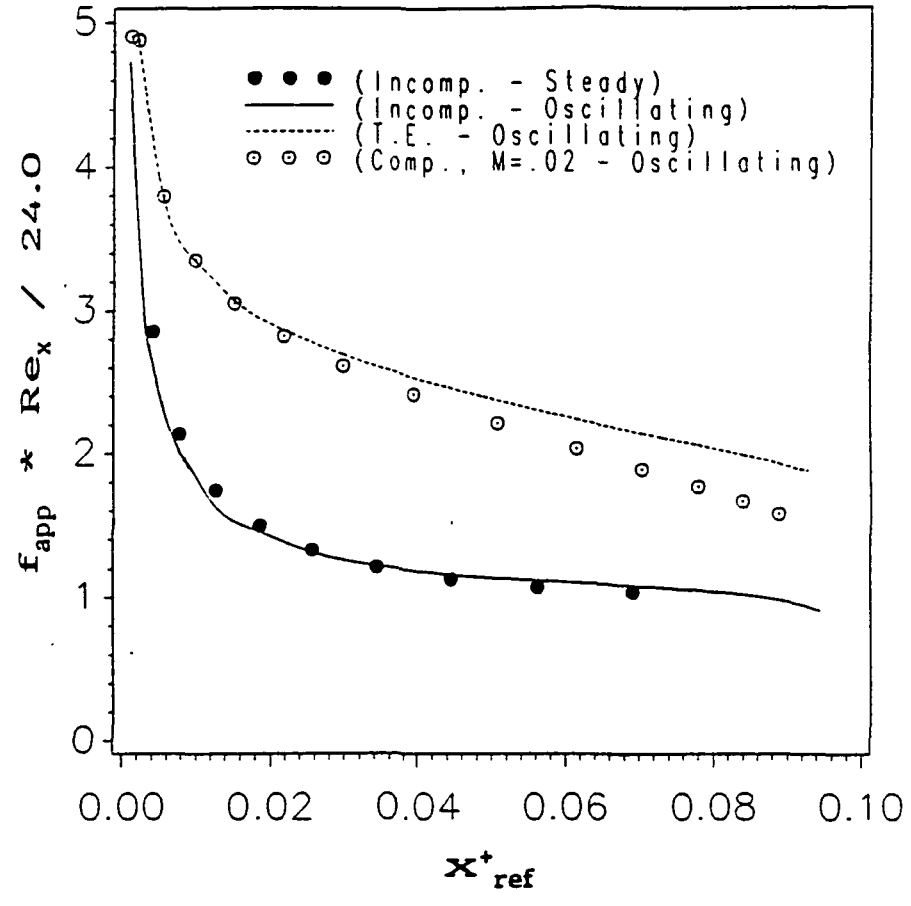

Figure 4.3.5: Comparison of the time-averaged local apparent friction in the channel between different fluid property models (Re_{max}=2000, ω^+=32.0) [OS-1, OS-2, OS-3].

models are close in value at the entrance, but diverges downstream at 15% difference. This frictional analysis expresses the importance to examine oscillating flow with the variable property models and reveals the limitation of the incompressible model.

In Figure 4.3.6, the mean fluid temperature versus time is plotted for two axial locations: one at the central channel and one close to the entrance. The figure shows two oscillating temperature cycles for every oscillating velocity cycle which corresponds to other oscillating flow literature. The minimal difference in mean temperature is observed between different fluid property models.

Figure 4.3.7 shows the time-averaged local heat flux in the channel predicted by the different fluid property models. With the wall/inlet temperature ratio set at 1.2, the heat flux predictions of the thermally expandable model are about 3% higher than the incompressible model. Identical time-averaged heat flux results were found between the thermally expandable model and the compressible model at M=.02 (see Table 4.3.2b).

The same conclusion in the pulsating flow is observed for the oscillating flow. For variable property flows, the wall/inlet temperature ratio and the Mach number has a direct effect on the friction factor while a secondary effect on the heat transfer.

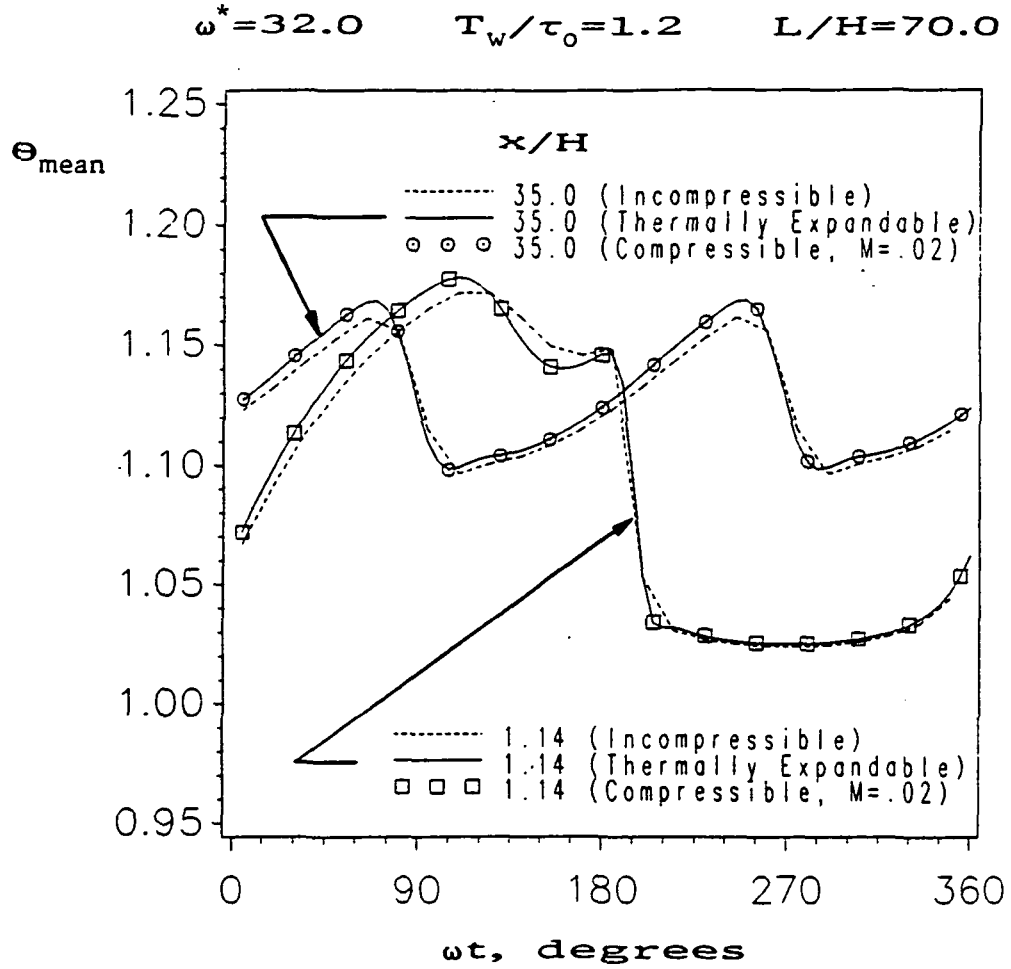

Figure 4.3.6: Mean fluid temperature versus time for simultaneously developing, oscillating flow. Predictions from different fluid property models are compared (T_w/τ_0=1.2, Re_{max}=2000, ω^*=32.0) [OS-1, OS-2, OS-3].

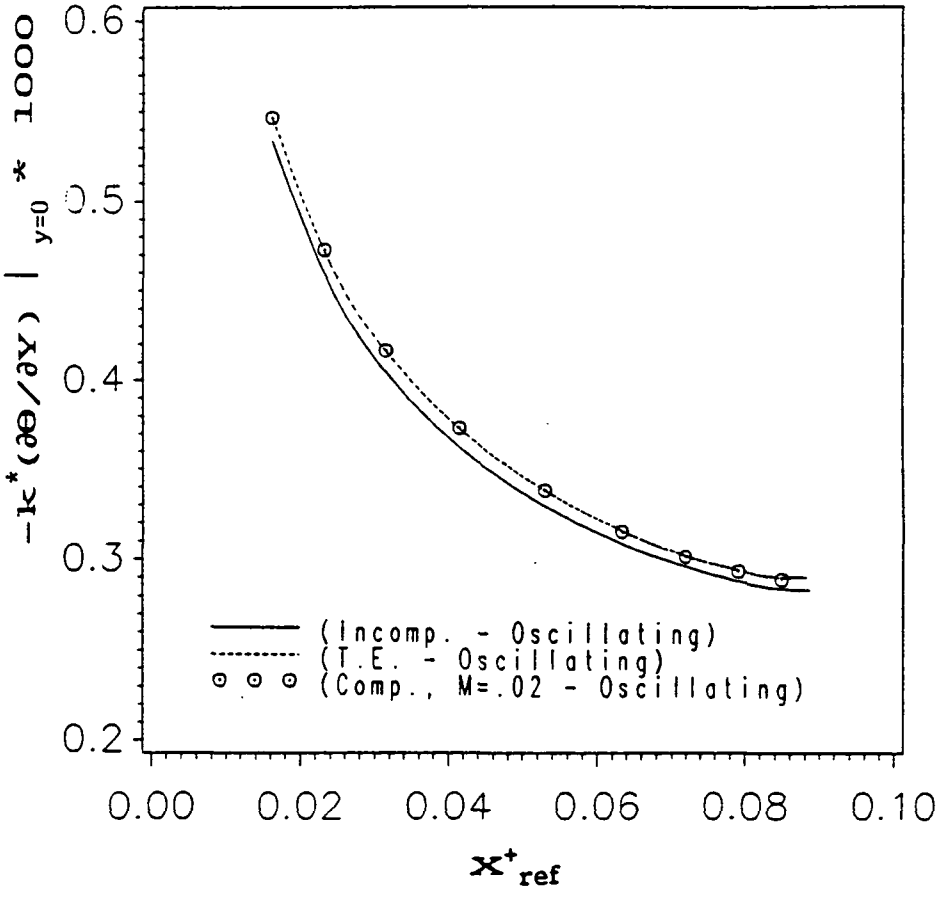

Figure 4.3.7: Comparison of the time-averaged local heat flux in the channel between different fluid property models (T_w/τ_0=1.2, Re_{max}=2000, ω^+=32.0) [OS-1, OS-2, OS-3].

Table 4.3.2: Comparison of the oscillating flow results between different fluid property models (Re_{max}=2000, ω^+=32.0, T_w/T_0=1.2, Helium) [OS-1 to OS-3]:

a) time-averaged apparent friction.

X_{ref}^+	Time-Averaged Local F*			Diff. from T.E. (%)	
	Incomp.	T.E.	Comp.	Incomp.	Comp.
.01	1.738	3.283	3.279	-47.0	-0.1
.02	1.409	2.890	2.860	-51.2	-1.0
.04	1.185	2.523	2.406	-53.0	-4.6
.08	1.037	2.026	1.725	-48.8	-14.9

b) time-averaged heat flux.

X_{ref}^+	Time-Averaged Local Q* (* 1000)			Diff. from T.E. (%)	
	Incomp.	T.E.	Comp.	Incomp.	Comp.
.01	.636	.651	.651	-2.3	0.0
.02	.487	.499	.499	-2.4	0.0
.04	.370	.381	.381	-2.9	0.0
.08	.286	.293	.292	-2.4	-0.3

Notes:

$Q^* = -k^*(\partial\Theta/\partial Y)\big|_{y=0}$

$F^* = f_{app} * Re_x / 24$

Incomp – Incompressible

T.E. – Thermally Expandable

Comp. – Compressible (M=.02)

Oscillating Flows (SPRE Boundary Conditions):

The two components under examination are the heater and the cooler of the NASA Space Power Research Engine (SPRE). In Appendix A-5, the run numbers OS-4 and OS-5 show the characteristic parameters of the cooler while the run numbers OS-6 and OS-7 represent the heater. Each component was solved under the incompressible fluid model and the compressible fluid model.

Figure 4.3.8 shows the time-averaged local apparent friction of the heater and cooler compared with the results from the incompressible and compressible (M=.01) analysis. It can be seen that only a slight difference existed between the predictions of the two fluid property models. The same conclusion was found on the comparison of the time-averaged Nusselt number presented in Figure 4.3.9.

The identical friction and heat transfer results between the incompressible and compressible models is caused by the characteristic parameters used. In the present analysis, the compressibility of the fluid is limited to the dependence of the temperature change and the flow speed. Since the wall/inlet temperature ratios are close to one and the Mach number is at a low .01, the conditions make these oscillating flows ideal incompressible property models. However, in the actual engine, the fluid compression and expansion caused by the out-of-phase movement between the displacer and the power piston will make an impact on the friction and the Nusselt number, which is not accounted for in this study. This also confirms the assumption Seume [1988] suggested that compressibility

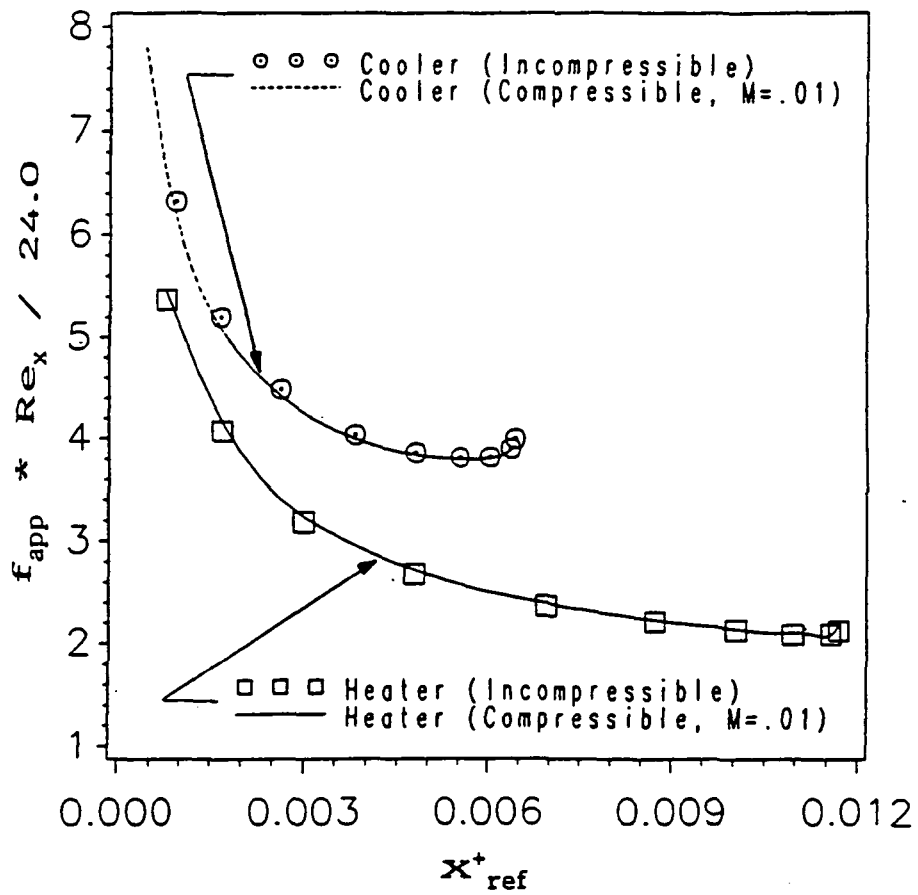

Figure 4.3.8: **Time-averaged local apparent friction in the channel at the SPRE Stirling engine heat exchanger conditions [OS-4, OS-5, OS-6, OS-7].**

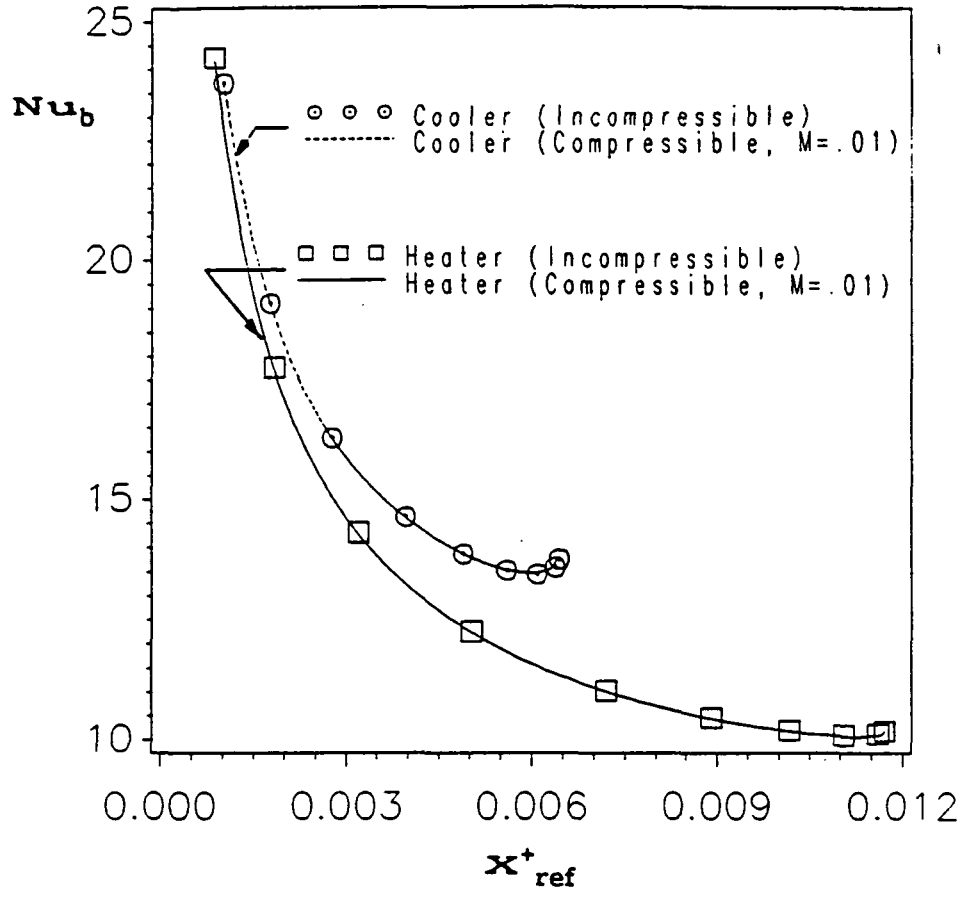

Figure 4.3.9: **Time-averaged local Nusselt number in the channel at the SPRE Stirling engine heat exchanger conditions [OS-4, OS-5, OS-6, OS-7].**

initiated by the flow speed is insignificant compared to the volumetric change in the expansion and compression spaces. But to model the actual fluid compressibility caused by the volumetric change requires moving boundaries which is out of the current code's capacity range.

CHAPTER V

CONCLUSIONS AND RECOMMENDATIONS

The Partially-Parabolized Navier-Stokes equations have been used to analyze the compressible and unsteady, periodic internal flows. The computer code has been validated for steady flow conditions, and the present numerical predictions were in excellent agreement with data obtained from the Navier-Stokes equations and the boundary-layer equations reported in the literature.

Upon examining the pulsating flow, the accuracy of the present numerical code was validated by the comparison with the closed form solutions from Siegel and Perlmutter [1962]. Excellent agreements were obtained for the incompressible fully-developed flow conditions and thermally developing with slug flow approximation.

An interesting observation was made on the mass flux during the examination of the pulsating flow with variable fluid properties. The viscous damping of the fluid was diminishing the fluctuating component of the pulsating flow. Thus, if the channel is sufficiently long, the pulsating

flow will become steady-state downstream. This is an observation in which the incompressible model cannot obtain.

Also found in the pulsating flow analysis is that the fluid compressibility has a stronger effect on the friction factor value than on the heat transfer coefficient (see Table 4.2.5 and 4.2.8). Furthermore, the difference between the steady state Nusselt number and the local time-averaged Nusselt number is less than 1.2% for the cases considered. This leads to the conclusion that pulsating flows contribute negligible heat transfer enhancements compared with the steady flows for the cases considered (see Appendix A-4).

For the oscillating flow, the present fully-developed velocity profiles are compared with the analytical results from Kurzweg [1985] at ω^{+}=32 and Re_{max}=2000. Excellent agreement was obtained. From the variable property models where T_w/τ_0=1.2, the substantial friction difference of about 50% was observed between the incompressible results and the thermally expandable results. This shows the importance to examine oscillating flow with the variable property models.

For the SPRE conditions, the present code predicted similar friction and Nusselt number results from the incompressible and compressible models. However in the present analysis, the compressibility of the fluid is limited to the dependency of the temperature change and the flow speed, while neglecting the actual compression and expansion effects produced by the out-of-phase movement of the piston and the displacer. Further modification of the present code is needed to simulate the engine

conditions. Perhaps incorporating the moving inlet and exit boundaries and use of the full Navier-Stokes equations would predict results closer to the engine conditions. As an ultimate goal, it would be desirable to extend the present solution procedure to handle turbulent flows.

Finally, two flow visualization videos were generated from the present solutions. The first video named "Pulsatile Flow Between Parallel Plates" animates the pulsating flows at three different Valensi numbers: .08, 32.0, and 200.0. The fluid air travels at a mean Reynolds number of 2000 while the amplitude of the velocity fluctuation is half of the mean velocity. In all cases, the fluid is heated by the constant wall temperature at the ratio of 1.2 to the inlet fluid temperature.

The second video named "Oscillating Flow Between Parallel Plates" contains two parts of visualization animations. The first part shows three different Valensi numbers (.08, 32.0, and 100.0) with the operating maximum Reynolds number set at 2000. Helium is the selected fluid and is heated by the constant wall/inlet temperature ratio of 1.2. The second part contains the oscillating flow animations at the Stirling engine cooler and heater conditions. The characteristic parameters are listed in Appendix A-5.

Both pulsating and oscillating flows utilize a channel with a length of 70 times the height. Numerical calculations were done at every 5 degrees, hence each cycle is animated by 72 frames of plots. The resulting parameters examined in both videos were the velocity profile, the temperature contour, the inlet velocity, the center-line pressure in the

channel, and the apparent friction and Nusselt number; each of these parameters is animated with respect to time.

The videos clearly reflect the quasi-steady behavior of the flow when the Valensi number is low (.08) but this behavior switches to non-quasi-steady as the Valensi number increases (32.0, 100.0 and 200.0). The videos also demonstrate the difference between incompressible, thermally expandable and compressible flows.

BIBLIOGRAPHY

Anderson, D.A., Tannehill, J.C., and Pletcher, R.H., 1984, *Computational Fluid Mechanics and Heat Transfer*, Hemisphere Publishing, New York.

Atkinson, B., Brockleband, M.P., Card, C.C.H., and Smith, J.M., 1969, Low Reynolds Number Developing Flows, *A.I.Ch.E. Journal*, Vol.15, No.4, pp.548-553.

Bankston, C.A. and McEligot, D.M., 1969, Prediction of Tube Wall Temperatures with Axial Variation of Heating Rate and Gas Property Variation, *Nuclear Science and Engineering*, Vol.37, pp.157-162.

Bankston, C.A. and McEligot, D.M., 1970, Turbulent and Laminar Heat Transfer to Gases with varying Properties in the Entry Region of Circular Ducts, *Int. J. Heat Mass Transfer*, Vol.13, pp.319-344.

Beam, R.M. and Warming, R.F., 1978, An Implicit Factored Scheme for Compressible Navier-Stokes Equations, *AIAA Journal*, Vol.16, No.4, pp.393-402.

Bhatti, M.S. and Savery, C.W., 1977, Heat Transfer in the Entrance Region of a Straight Channel: Laminar Flow with Uniform Wall Heat Flux, *Journal of Heat Transfer*, February, pp.142-144.

Brandt, A. and Gillis, J., 1966, Magnetohydrodynamic Flow in the Inlet Region of a Straight Channel, *Physics of Fluids*, Vol.9, pp.690-699.

Cebeci, T. and Bradshaw, P., 1984, *Physical and Computational Aspects of Convective Heat Transfer*, Springer-Verlag, New York, pp.372-384.

Chen, R.Y., 1973, Flow in the Entrance Region at Low Reynolds Numbers, *Journal of Fluids Engineering*, Vol.95, pp.153-158.

Chilukuri, R., 1979, Calculation Procedure for the Partially Parabolized Navier-Stokes Equations in Primitive Variables for Steady, Two-Dimensional Flow, M.S. Thesis, Iowa State University, Ames, Iowa.

Chiu, I.T., 1984, Prediction of Laminar Flows over a Rearward-Facing Step using the Partially-Parabolized Navier-Stokes Equations, M.S. Thesis, Iowa State University, Ames, Iowa.

Creff, R., Andre P., and Batina, J., 1985, Dynamic and Convective Results for a Developing Laminar Unsteady Flow, *Int. Journal for Numerical Methods in Fluids*, Vol.5, pp.745-760.

Creff, R., Batina, J., Andre P., and Karunanithi, V.S., 1983, Numerical Model for Dynamic and Thermal Developments of a Pulsed Laminar Ducted Flow, *Numerical Heat Transfer*, Vol.6, pp.173-188.

Friedmann, M., Gillis, J., and Liron, N., 1968, Laminar Flow in a Pipe at Low and Moderate Reynolds Numbers, *Applied Science Research*,

Vol.19, pp.426-438.

Han, S.M., 1983, A Generalized Implicit Finite Difference Method for Transient Analysis of Compressible and Incompressible Fluid Flows, *Numerical Methods for Fluid Transient Analysis, ASME*, Vol.4, pp.17-21.

Hassankhan, S., 1983, Effects of Fluid Compressibility and Surface Curvature on Stagnation Point Heat Transfer, M.S. Thesis, Cleveland State University, Cleveland, Ohio.

Heaton, H.S., Reynolds, W.C., and Kays, W.M., 1964, Heat Transfer in Annular Passages. Simultaneous Development of Velocity and Temperature Fields in Laminar Flow, *Int. Journal for Heat and Mass Transfer*, Vol.7, pp.763-781.

Herwig, H., Klemp, K., and Stinnesbeck, J., 1990, Laminar Entry Flow in a Pipe or Channel: Effect of Variable Viscosity due to Heat Transfer Across the Wall, *Numerical Heat Transfer, Part A*, Vol.18, pp.51-70.

Hwang, C.L., 1973, Dept. Industrial Engineering, Kansas State University, Manhattan. (His steady, incompressible flow results are printed in Shah and London's book, 1978)

Hwang, C.L. and Fan, L.T., 1964, Finite Difference Analysis of Forced-Convection Heat Transfer in the Entrance Region of a Flat Rectangular Duct, *Applied Scientific Research*, Vol. 13, Section A, pp.401-422.

Ibrahim, M.B. and Kwan, C.F., 1991, Predictions for Hydrodynamically and Thermally Developing Pulsatile Flows, *Proc. 4th International Symposium on Transport Phenomena in Heat and Mass Transfer*, Sydney, Australia, Vol.4, pp.1570-1581.

Ibrahim, M.B., Tew, R.C., Jr., and Dudenhoefer, J.K., 1990, Further Two-Dimensional Code Development for Stirling Engine Components, *Proc. 25th Intersociety Energy Conversion Engineering Conf.*, Reno, Vol.6, pp.329-335.

Ibrahim, M.B., 1989, Multi-Dimensional Code Development for Stirling Engine - Progress Report, Presented at NASA Lewis Research Center, Cleveland, Ohio.

Ishida, M., and Yamada, T., 1980, Wall Friction and Local Heat Transfer in Oscillating Flow (Two-dimensional Unsteady Laminar Boundary Layer on a Flat Plate), *Bulletin of the JSME*, Vol.23, No.183, pp.1467-1474.

Kamotani, Y. and Ostrach S., 1976, Effect of Thermal Instability on Thermally Developing Laminar Channel Flow, *Journal of Heat Transfer*, February, pp.62-66.

Kays, W.M. and Crawford, M.E., 1987, *Convective Heat and Mass Transfer*, 2nd ed., McGraw-Hill book Company, New York.

Kim, S.W., 1990, Numerical Investigation of Separated Transonic Turbulent

Flows with a Multiple-Time-Scale Turbulence Model, *Numerical Heat Transfer, Part A*, Vol.18, pp.149-171.

Kwon, O.K., Pletcher, R.H., and Delaney R.A., 1988, Solution Procedure for Unsteady Two-Dimensional Boundary Layers, *Journal of Fluids Engineering*, Vol.110, pp.69-75.

Langhaar, H.L., 1942, Steady Flow in the Transition Length of a Straight Tube, *Trans. ASME, J. Appl. Mech.*, Vol.64, pp.A.55-A.58.

Lou, Y.S., 1971, Heat Transfer in the Entrance Region between Two Parallel Plates with Constant Uniform Temperature, *AIAA Paper 71-36*, New York.

Lou, Y.S. and Barton, L.O., 1973, Entrance Region Heat Transfer between Parallel Plates with Uniform Wall Temperature, *AIAA Journal*, Vol.11, No.3, pp.393-394.

MacCormack, R.W., 1976, An Efficient Numerical Method for Solving the Time-Dependent Compressible Navier-Stokes Equations at High Reynolds Number, *NASA Technical Memorandum*, TMX-73,129.

MacCormack, R.W., 1982, A Numerical Method for Solving the Equations of Compressible Viscous Flow, *AIAA Journal*, Vol.20, No.9, pp.1275-1281.

Madavan, N.K., 1981, Prediction of Incompressible Laminar Separated Flows using the Partially-Parabolized Navier-Stokes Equations, M.S. Thesis, Iowa State University, Ames, Iowa.

Mercer, W.E., Pearce, W.M., and Hitchcock, J.E., 1967, Laminar Forced Convection in the Entrance Region between Parallel Flat Plates, *Journal of Heat Transfer*, Vol.89, pp.251-257.

Morihara, H. and Cheng, R.T., 1973, Numerical Solution of Viscous Flow in the Entrance Region of Parallel Plates, *Journal of Computational Physics*, Vol.11, pp.550-572.

Narang, B.S. and Krishnamoorthy, G., 1976, Laminar Flow in the Entrance Region of Parallel Plates, *Journal of Applied Mechanics*, pp.186-188.

Patankar, V.S., 1980, *Numerical Heat Transfer and Fluid Flow*, Hemisphere Publishing, New York.

Presler, A.F., 1971, Analytical and Experimental Study of Compressible Laminar-Flow Heat Transfer and Pressure Drop of a Gas in a Uniformly Heated Tube, *NASA Technical Note*, TN D-6333.

Riley, N., 1975, Unsteady Laminar Boundary Layers, *SIAM Review*, Vol.17, No.2, pp.274-297.

Roache, P.J., 1972, *Computational Fluid Dynamics*, Alburquerque : Hermosa Publishers.

Schade, K.W. and McEligot, D.M., 1971, Cartesian Graetz Problems with Air

Property Variation, *Int. J. Heat Mass Transfer*, Vol.14, pp.653-666.

Schlichting, H., 1960, *Boundary Layer Theory*, 4th ed., McGraw-Hill Book Company, New York, pp.169-171.

Shah, R.K., and London, A.L., 1978, *Advances in Heat Transfer: Laminar Flow Forced Convection in Ducts*, Academic Press, New York.

Siegel, R., 1987, Influence of Oscillation-Induced Diffusion on Heat Transfer in a Uniformly Heated Channel, *Transaction of the ASME, Journal of Heat Transfer*, Vol.109, pp.244-247.

Siegel, R., and Perlmutter, M., 1962, Heat Transfer for Pulsating Laminar Duct Flow, *Transaction of the ASME, Series C: Journal of Heat Transfer*, Vol.84, No.2, pp.111-123.

Siegel, R., and Sparrow, E.M., 1959, Simultaneous Development of Velocity and Temperature Distributions in a Flat Duct with Uniform Wall Heating, *A.I.Ch.E. Journal*, Vol.5, No.1, pp.73-75.

Spalding, D.B., 1972, A Novel Finite-Difference Formulation for Differential Expressions Involving Both First and Second Derivatives, *Int. J. Numer. Methods Eng.*, Vol.4, pp.551-559.

Tew, R.C., Jr., 1987, Overview of Heat Transfer and Fluid Flow Problem Areas Encountered in Stirling Engine Modeling, *Winter Annual Meeting of the ASME, Boston*, FED-Vol.62, HTD-Vol.93, pp.77-88.

Tribus, Myron, and Boelter, L.M.K., 1942, An Investigation of Aircraft Heaters: II - Properties of Gases, *NACA ARR*, October.

Uchida, S., 1956, The Pulsating Viscous Flow Superposed on the Steady Laminar Motion of Incompressible Fluid in a Circular Pipe, *Zeitschr. Angew. Mathem. Phys.*, Vol.7, pp.403-422.

Van Driest, E.R., 1952, Investigation of Laminar Boundary Layer in Compressible Fluids using the Crocco Method, *NACA* TN2597.

White, F. M., 1974, *Viscous Fluid Flow*, McGraw-Hill, New York.

APPENDIX - A

List of Flow Runs Examined

Appendix A-1: Steady Flow Runs (Incompressible)

Run Number	Re_θ	Fluid (Pr no.)	Grid Size (x,y)	Wall Temp, θ
SI-1	40	Air (.72)	50 X 91	2.0
SI-2	100	Air (.72)	50 X 91	2.0
SI-3	100	Air (.72)	50 X 91	1.5 (upper) 0.5 (lower)
SI-4	144	Air (.72)	60 X 40	1.0
SI-5	1000	Air (.72)	60 X 40	1.0
SI-6	2000	Air (.72)	107 X 29	.67
SI-7	2000	Air (.72)	107 X 29	1.0
SI-8	2000	Air (.72)	107 X 29	1.5

Appendix A-2: Steady Flow Runs (Thermally Expandable)

Run Number	Re_θ	Fluid (Pr no.)	Grid Size (x,y)	Wall Temp, θ
ST-1	144	Air (.72)	60 X 40	0.5
ST-2	144	Air (.72)	60 X 40	2.0
ST-3	144	Air (.72)	60 X 40	5.0
ST-4	2000	Air (.72)	107 X 29	0.5
ST-5	2000	Air (.72)	107 X 29	0.67
ST-6	2000	Air (.72)	107 X 29	1.2
ST-7	2000	Air (.72)	107 X 29	1.4
ST-8	2000	Air (.72)	107 X 29	1.5
ST-9	2000	Air (.72)	107 X 29	2.0
ST-10	2000	Air (.72)	107 X 29	5.0

Appendix A-3: Steady Flow Runs (Compressible)

Run Number	Re_∞	Fluid (Pr no.)	Grid Size (x,y)	Wall Temp, θ	Mach No.
SC-1	2000	Air (1.0)	107 X 29	0.980	0.25
SC-2	2000	Air (1.0)	107 X 29	0.993	0.25
SC-3	2000	Air (1.0)	107 X 29	1.000	0.25
SC-4	2000	Air (1.0)	107 X 29	1.007	0.25
SC-5	2000	Air (.72)	107 X 29	0.67	0.05
SC-6	2000	Air (.72)	107 X 29	0.67	0.10
SC-7	2000	Air (.72)	107 X 29	0.67	0.25
SC-8	2000	Air (.72)	107 X 29	1.50	0.05
SC-9	2000	Air (.72)	107 X 29	1.50	0.10
SC-10	2000	Air (.72)	107 X 29	1.50	0.25

Appendix A-4: Pulsating Flow Runs

Run Number	ω^*	ψ	T_w/T_∞	Fluid Properties	Mach no.
PI-1	0.08	1.00	2.0	Incomp.	--
PI-2	8.00	.778	2.0	Incomp.	--
PI-3	32.0	.298	2.0	Incomp.	--
PI-4	200.	.054	2.0	Incomp.	--
PI-5	0.08	1.00	1.4	Incomp.	--
PI-6	32.0	1.00	1.4	Incomp.	--
PI-7	100.	1.00	1.4	Incomp.	--
PT-1	0.08	1.00	1.2	T.E.	--
PT-2	0.08	1.00	1.4	T.E.	--
PT-3	32.0	1.00	1.2	T.E.	--
PT-4	32.0	1.00	1.4	T.E.	--
PT-5	100.	1.00	1.2	T.E.	--
PT-6	100.	1.00	1.4	T.E.	--
PC-1	0.08	1.00	1.2	Comp.	0.05
PC-2	32.0	1.00	1.2	Comp.	0.05
PC-3	100.	1.00	1.2	Comp.	0.02

Notes: All the above runs have the following parameters -

a) Air as the fluid with Pr=.72.
b) x,y-grid is 107 X 29, respectively.
c) Re_{∞}=2000.
d) Time step is 5 degrees.

Appendix A-5: Oscillating Flow Runs

Run Number	ω^*	Re_{max}	A_R	T_w/T_o	Fluid Properties	Mach no.
OS-1	32.0	2,000	.893	1.2	Incompressible	--
OS-2	32.0	2,000	.893	1.2	Thermally Expandable	--
OS-3	32.0	2,000	.893	1.2	Compressible	.02
OS-4	350.0	30,000	1.22	0.956	Incompressible	--
OS-5	350.0	30,000	1.22	0.956	Compressible	.01
OS-6	88.0	16,500	2.68	1.048	Incompressible	--
OS-7	88.0	16,500	2.68	1.048	Compressible	.01

Notes: All the above runs have the following parameters -

a) Helium as the fluid with Pr=.72.
b) x,y-grid is 107 X 29, respectively.
c) Channel length is L/H=70.0.
d) Time step is 5 degrees.

APPENDIX - B

Explanation of Input Parameters for the Computer Code

This variable list contains the input parameters used by the present computer code and their explanations. The sequence of these variables are in the same order as they appear in the READ statement.

HIGHT	Channel inlet height.
THIGHT	Total channel height including the wall's thickness. If the wall's thickness is not considered in the analysis, set equal to HIGHT.
HSTEP	Step height of the sudden expansion. For Straight Parallel Plates Channel(SPPC), set equal to 0.0 .
XSTEP	Streamwise location of the step for SPPC, set equal to 0.0 .
FLARE	Constant for FLARE approximation. Set equal to 0.0 .
DMLFCT	Constant used for the set up of the x-grid. Normally, set equal to 1.01 - 1.20 .
LPNS	Designates the axial station index (MCOUNT) after which the governing equations (PPNS or NS) are to be solved. For most cases, set equal to 1 .
KPNS	Designates MCOUNT after which the governing equations need not be solved.
JPNS	Designates MCOUNT after which Global Iteration in Space(GIS) is desired. In general, set to 2 .
NLMT	Safety parameter designating the maximum allowable MCOUNT, set equal to KPNS.
LPOP	For external pressure gradient flows, this represents the number of freestream u-velocity input. For internal fluid flows, set to 0 .
NJ	Total number of grid points in the y-direction inside the channel.
INV	For external pressure gradient flows, this represents the number of freestream v-velocity inputs. Set to 0 for internal flows or when no v-velocities are prescribed.

INT	This represents the number of wall temperature inputs on the upper or lower boundaries. Set to 0 for isothermal or constant heat flux boundary conditions.
ZAP1	Output selections: For abbreviated output, set equal to 1 ; for detailed output at each streamwise station, set to -1 .
GLOBE	Beginning cycle number for this run. Set equal to min.
TOLERC	No longer used. Tolerance on the streamwise pressure gradient to be used in secant procedure when estimating the initial pressure field for the first cycle.
XE	Safety parameter designating the maximum axial distance in length beyond which no calculation will be done.
PR	Prandtl number.
CPS	Specific heat.
TEST	Value used to check for edge of B.L., typically 0.9995 for fully-developed flow and 0.995 for developing flow.
US	The u-velocity used for nondimensionalization.
XMUS	The absolute viscosity at the channel's inlet used for nondimensionalization.
RHOS	The fluid density at the channel's inlet used for nondimensionalization.
VW	Normal velocity at the wall. Set equal to 0.0 for no-slip conditions at the wall.
UREF	Freestream u-velocity that will vary with axial distance, however, US remains fixed. Set equal to the freestream value at first axial station.
TWL	Wall temperature for the lower isothermal boundary.
TWU	Wall temperature for the upper isothermal boundary. For the symmetrical analysis, set equal to any value.

MIN	Beginning GIS. In general, set to 1 .
MAX	Final GIS.
IUPDAT	Set to 1 if the best known values are used in evaluating convective coefficients for the pressure gradients, F1 and F2. Otherwise set equal to 0 . In general, set equal to 0 .
NPOINT	The number of y-grid points used inside of each channel wall. If the wall thickness is not considered in the analysis, set equal to 0 .
LTEMP	Number of x-stations from the inlet for the wall temperature to reach the desired constant wall temperature. For constant wall temperature starting at the inlet, set equal to 0 .
MP1	The number of MCOUNTs to be read in to determine detailed printout stations.
MPC(J)	J=1,MP1 . The MCOUNTs of streamwise stations where detailed printout is desired.
NP1	Number of x distance from the inlet to be read in to determine detailed printout locations.
NWALL	For asymmetric test cases: Set to 2 if one-sided differencing is to be used to evaluate F1 and F2 near wall. Set to -2 if regular differencing is to be used. For other geometries (including SPPC): Set to 1 for one-sided differencing. Set to -1 for regular differencing.
JSTEP	Grid-point index in y-direction for the first point below the sudden expansion step. For the SPPC analysis, set equal to 1 .
MCSTEP	Station index (MCOUNT) for the first station downstream of the sudden expansion step. For the SPPC analysis, set to 1 .
NTEMP	Set to 1, if the energy equation is to be solved, otherwise set to 0 . For variable fluid properties, set NTEMP equal to 1 .

NWALLT	Set to 0, if both the upper and lower boundaries are isothermal. Set to 1, if the temperatures on both boundaries are not constant. Set to >1, if only the lower boundary is NOT isothermal. Set to <0, if only the upper boundary is NOT isothermal.
NEXTRP	Set to 1, if extrapolation is to be used to evaluate F1 and F2 near wall, otherwise set to 0 .
XP3(J)	J=1,NP1 . The x-distances from the inlet of the channel where detailed printout is desired.
NPRINT	Set to 0 if abbreviated output is required when solving the Poisson equation for pressure. Set to 1 for detailed printout. ZAP, if set equal to 1, overrides NPRINT and no details are printed.
LSOR1	For the steady flow analysis: If set to 1, calculation of the beginning GIS (MIN) starts with solving the Poisson equation. In this case, the marching sweep for this GIS must have been already calculated and the results stored on unit 9. Choice of LSOR1 is related to value of LSOR. Set to 0 for first GIS. For the unsteady flow analysis: Set to 0 for the first time cycle.
LSOR2	If set equal to 1, the final GIS (MAX) completes with the calculation of the Poisson equation for pressure. If set equal to 0, the final GIS finishes with the marching integration sweep calculation but the Poisson equation is not solved.
LEAD	This variable specifies the singularity condition of the u-velocity at the point just ahead of the leading edge of the plate. When set to 0, this u-velocity is zero. When set to 1, this u-velocity is set to UREF. In the present study (SPPC), LEAD is set to 0.
FAC	The over-relaxation factor used on the pressure update after solving the Poisson equation by the method of SOR by points. Values used range from 1.5 to 1.97 .

TOL	No longer used. When positive, this represents tolerance on the total mass flow rate when making block adjustments on pressure. This option used only after convergence has become montonic. If block adjustments are not required, set to any negative value. Make sure TOL is small when positive to avoid imposing oscillations.
XKWL	The thermo-conductivity of the walls (Pr_{solid}). If the analysis does not include the walls, set equal to PR.
FROMINLT	This variable is for print-out purpose only. Set to the x-value where the current results are started from. In general set this equal to 0.0 .
RC	Critical mesh Reynolds number. Set to 1.9 .
ERRMAX	Mass convergence criteria. Set to around .10 .
NIRROT	Set to 2 .
IRROT	Set to 0 if the freestream u, v-velocities are specified. Set to 1 if only freestream u values are specified and an irrotational outer-edge boundary condition is to be used on the v-velocities. The second option does not work well.
NDOWN	Specifies the downstream pressure boundary condition. If set to: 0 - no downstream boundary condition is imposed on the pressure. 1 - constant axial pressure gradient condition is imposed. -1 - constant normal pressure gradient condition is imposed.
NOBLK	When set to 0, the pressure block adjustment is used in all the GIS. If set to 1, the pressure block adjustment is used in the GIS up to the iteration specified in NBLK, after that no pressure block adjustment is used. For the variable properties analysis, set NOBLK to 1 .
NBLK	The number of GIS that the pressure block adjustment is used. NBLK is ignored when NOBLK is set to 0 .

NSUTH	This variable specifies the method used to determine the viscosity of the fluid. If set to 1, the Sutherland's Law is used. If set to 0, the Power Law is used. For the constant properties case, set NSUTH to 0 .
NCOMP	For compressible flow, set equal to 1 . For thermally expandable or incompressible flow, set equal to 0 .
XBEGIN	This variable represents the x coordinate value at which the calculation begins.
SUTH	The Sutherland's constant in degree Kelvin used to determine the value of the fluid viscosity. (Example: for air SUTH=110.4 K) SUTH is ignored when NSUTH is set to 0 .
ALPHA	The exponent α in the Power Law is used to determine the fluid viscosity. Set ALPHA to 0.0 for incompressible analysis. ALPHA is ignored when NSUTH is set to 1 .
BETA	The exponent β in the Power Law is used to determine the fluid conductivity. Set BETA equal to 0.0 for incompressible analysis. BETA is ignored when NSUTH is set equal to 1 .
GAMMA	The exponent γ in the perfect gas relationship is used to determine the fluid density. Set GAMMA equal to 1.0 for variable density (thermally expandable or fully compressible). Set GAMMA equal to 0.0 for incompressible analysis.
XMACH	The reference mach number of the flow. This variable is ignored when NCOMP is equal to 0 .
CPRATIO	The ratio of specific heats of the fluid. This variable is ignored when NCOMP is equal to 0 .
NSTEAD	This variable specifies the type of flow to be considered. Set to 1 for steady flow. Set to 0 for unsteady flow (pulsatile or oscillating).
N2DPRT	For print-out of 2-D velocity and fluid properties, set to 1.0 .

UB(J)	Read only when the flow is steady (NSTEAD=1). J=1,NJ+1. The inlet u-velocity profile at the upstream boundary.
VB(J)	Read only when the flow is steady (NSTEAD=1). J=1,NJ+1. The inlet v-velocity profile at the upstream boundary. Note that the axial location of this profile is slightly different than that for the u-velocity profile due to the staggered grid format.
NCYCLE	Read only when the flow is unsteady (NSTEAD=0). The number of pulsating (or oscillating) cycles to be made in this run.
NDEGRE	Read only when the flow is unsteady (NSTEAD=0). The degree increment used in the calculation (One cycle has 360 degrees). Set NDEGRE greater than or equal to 5 .
NSLUG	Read only when the flow is unsteady (NSTEAD=0). Set to 1 for the slug flow approximation when determining the temperature field. Set to 0 for simultaneously developing flow. The slug flow approximation works only for the incompressible flow. Set to 0 when making a variable properties analysis.
NOSCIL	Set to 1 for oscillating flow. Set to 0 for pulsating flow.
NSKIP	Number of time step to be skipped around the zero velocity for the oscillating flow. Input even number only.
VALENSI	Read only when the flow is unsteady (NSTEAD=0). Valensi number.
UMEAN	Read only when the flow is unsteady (NSTEAD=0). The time average value of the inlet u-velocity. For Oscillating flow, set UMEAN equal to 0.0 . Note that for unsteady flow the inlet velocities are assumed uniform in profile.

DELTU — Read only when the flow is unsteady (NSTEAD=0). The amplitude of the fluctuating u-velocity at the inlet of the channel. (Example: If UMEAN & DELTU are set to 1.0 & .5, respectively, the inlet u-velocity will vary from .5 to 1.5 sinusoidally through the cycle).

MSEP1 — Set to the MCOUNT value beyond which the 2-D u,v-velocity arrays are stored. For separated, incompressible, and steady flow, set equal to the MCOUNT value slightly ahead of the separation point. For steady incompressible flow in SPPC, set equal to KPNS. For other flows (variable properties, pulsating, or oscillating) set equal to 1 .

MSEP2 — Set to the MCOUNT value beyond which the 2-D u,v-velocity arrays are not stored. For separated, incompressible, and steady flow, set equal to the MCOUNT value slightly beyond the reattachment. For other flows (steady incompressible flow in SPPC, variable properties, pulsating, or oscillating) set equal to KPNS. For full Navier-Stokes calculation, the specified values of MSEP1 and MSEP2 are overridden within the program (no changes were made in the full N.S. equations to run variable properties or unsteady flows).

MCDOWN — The MCOUNT value at the downstream. Set equal to KPNS.

NSFULL — Set equal to 0 for solving the Partially Parabolized Navier-Stokes (PPNS) equations. Set to 1 if the full Navier-Stokes (NS) equations are to be solved. Note that even when full NS equations are to be solved, NSFULL must be set to 0 for the first GIS. No modifications were made to update the full NS equations for unsteady, thermally expandable, or compressible flow analysis. For the present study, set to 0 .

NHYBRD — Set equal to 1 to use the hybrid differencing scheme. If set to 0, pure upwind or central differencing is used depending on the value of the mesh Reynolds number. In general, set to 1 .

NSTEP	Set equal to 0, when analyzing the external or internal asymmetric channel flow. Set to 1 for internal symmetric channel flow.
MSEP11	Set to the MCOUNT value where beyond which the 2D u,v-velocities were stored from the previous GIS. In general, set equal to MSEP1.
MSEP22	Set to the MCOUNT value where beyond which the 2D u,v-velocities were Not stored from the previous GIS. In general, set equal to MSEP2.
XU(J)	Not required for internal flows. J=1,LPOP. The x distances for freestream u-velocity input. (Note: No attempts were made to run an external flow analysis under the unsteady, thermally expandable, or compressible conditions).
YU(J)	Not required for internal flows. J=1,LPOP. The freestream u-velocity values corresponding to XU(J) values.
XV(J)	Not required for internal flows or if INV is set to 0 . J=1,INV. Represents the x distance for freestream v-velocity input.
YV(J)	Not required for internal flows or if INV is set to 0 . J=1,INV. Represents the freestream v-velocity values corresponding to XV(J) values.
MINT	Beginning GIS number for solving the energy equation.
MAXT	Final GIS number for solving the energy equation.
NENGY	Set to 1 if only the energy equation is to be solved (this option requires that the u,v-velocities have been solved in previous run); otherwise set to 0 .
IBL	Set equal to 1, if the Boundary Layer (B.L.) or the compressible energy equation is used, otherwise set to 0 . For Thermally expandable or Compressible flow analysis, set IBL equal to 1 .

NQWL	Set to 1 for constant heat flux at the lower wall, (currently, this works only for incompressible flow), otherwise set equal to 0 .
NQWH	Set to 1 for constant heat flux at the upper wall, (currently, this works only for incompressible flow), otherwise set equal to 0 .
QWL	This is the constant heat flux value at the lower wall, (currently, this works only for incompressible flow), if NQWL is set to 0, then QWL is ignored.
QWH	This is the constant heat flux value at the upper wall, (currently, this works only for incompressible flow), if NQWH is set to 0, then QWH is ignored.
TREF	The reference stagnation inlet temperature (in Kelvin).
TT(1,J)	J=1,NJ. The inlet temperature (in Kelvin) profile at the upstream boundary.
XTWL(J)	Not required for Isothermal or constant heat flux boundary. J=1,INT. The x distances for lower boundary temperature inputs.
YTWL(J)	Not required for Isothermal or constant heat flux boundary. J=1,INT. Lower boundary temperature values corresponding to the x distances, XTWL(J), values.
XTWU(J)	Not required for Isothermal or constant heat flux boundary. J=1,INT. The x distances for upper boundary temperature inputs.
YTWU(J)	Not required for Isothermal or constant heat flux boundary. J=1,INT. Upper boundary temperature values corresponding to the x distances, XTWU(J), values.
NG3(I)	I=MIN,MAX. The number of Gauss-Siedel sweeps to be carried out when solving the Poisson equation for pressure. For the first GIS, set to a small number (around 5). For later cycles, increase this number gradually.

NT3(I)	No longer used. I=MIN,MAX. The number of times the pressure is revised at each axial station during each conventional iteration of the SOR method when solving the Poisson equation for pressure.
FAC13(I)	I=MIN,MAX. The under-relaxation factor to be used on the pressure gradients after each marching integration sweep. Start with a small fraction and increase gradually but not to excess one.
FAC23(I)	I=MIN,MAX. The relaxation parameter for velocity corrections; 1.0 was used in this study.
FAC33(I)	I=MIN,MAX. The relaxation parameter for fluid properties corrections; 1.0 was used in this study.

*** Note: One data set of NG3, NT3, FAC13, FAC23, & FAC33 values is required for each GIS.

APPENDIX - C

Listing of the Computer Program